Downloaded from orbit.dtu.dk on: Apr 19, 2025

DTU Library

MIS hot electron devices for enhancement of surface reactivity by hot electrons

Thomsen, Lasse Bjørchmar

Publication date:
2009

Document Version
Early version, also known as pre-print

Link back to DTU Orbit

Citation (APA):
Thomsen, L. B. (2009). *MIS hot electron devices for enhancement of surface reactivity by hot electrons.* Technical University of Denmark.

General rights
Copyright and moral rights for the publications made accessible in the public portal are retained by the authors and/or other copyright owners and it is a condition of accessing publications that users recognise and abide by the legal requirements associated with these rights.

- Users may download and print one copy of any publication from the public portal for the purpose of private study or research.
- You may not further distribute the material or use it for any profit-making activity or commercial gain
- You may freely distribute the URL identifying the publication in the public portal

If you believe that this document breaches copyright please contact us providing details, and we will remove access to the work immediately and investigate your claim.

Ph. D. thesis
Center for Individual Nanoparticle Functionality
Department of Physics
Technical University of Denmark

MIS hot electron devices for enhancement of surface reactivity by hot electrons

by:

Lasse B. Thomsen

March 2009

Preface

This thesis and related experimental work has been carried out at the Center for Individual Nanoparticle Functionality (CINF) and the Department of Physics at the Technical University of Denmark. The work on this project work has endured from March 2006 to March 2009. CINF, and thus the work presented in this thesis, has been funded by the Danish National Research Foundation, which I thank for the opportunity and support.

The supervisors on this thesis were Professor Ib Chorkendorff and Associate Professor Ole Hansen, whom I would like to thank for their help, patience and guidance throughout the duration of this project. I would like to thank them both for letting me draw on their extensive knowledge within surface science, catalysis and semiconductor processing. A very big thanks goes to Ole for our discussions and patient help throughout the writing work of this thesis.

The experimental work and device fabrication has been done in collaboration with Ph.d. student Gunver Nielsen, whom I would like to thank for her help, friendship and cooperative spirit. I would also like to acknowledge Robert Jensen, Martin Johansson, Thomas Olsen, and Søren B. Vendelbo for their cooperation and fruitful discussions. I also acknowledge the help I have received from the workshop in 309, without their skillful work many of the results presented on the following pages would not have been possible to obtain.

Furthermore I would like to thank Rasmus M. Nielsen for his friendship, making the days in the lab seem shorter and more fun. My friend Jesper S. Jensen I would like to thank for his friendship, support and patient listening. A special thanks goes to my girlfriend Pia Nyberg for her incredible patience and loving care during, especially, the past months of hard work.

On a final note I would like to give my appreciation for the fantastic working and social environment in the CINF and CAMd conglomerate group, by thanking all past and present members for creating this environment.

Lasse Bjørchmar Thomsen, Kgs. Lyngby, March 2009

Abstract

A Metal-Insulator-Semiconductor (MIS) based device is developed for investigation of hot electron enhanced chemistry. A model of the device is presented explaining the key concepts of the functionality and the characteristics. The MIS hot electron emitter is fabricated using cleanroom technology and the process sequence is described. An Ultra High Vacuum (UHV) setup is modified to facilitate experiments with electron emission from the MIS hot electron emitters and hot electron chemistry. Simulations show the importance of keeping tunnel barrier roughness to an absolute minimum. The tunnel oxide is characterized using IV and CV measurements to extract tunnel barrier thicknesses, which was distributed around the expected value of 50 Å. CV measurements yield thicknesses between 44.7 Å and 58 Å. The IV and CV measurements is shown to correlate and an offset between the two types of measurements indicate some degree of roughness of the tunnel oxide. Electron emission is realized from the devices to a collector plate. The emission below 5 V varies between consecutive measurements, but is stable above 5 V. The work function is lowered using Cs to 2 eV and emitted electrons are observed from a bias voltage of 2 eV. The maximum emission efficiency of 8% is obtained at 3 V on the Cs covered MIS hot electron emitter. The mean free path of Au for 5 eV electron extracted from emission experiments is 52 Å, which is in excellent agreement with other measurements. The Ti wetting layer is found to be an important energy loss center for the electrons tunneling through the oxide lowering the emission efficiency of a factor of 10 for a 1 nm Ti layer thickness. Electron emission is observed under ambient pressure conditions and in up to 2 bars of Ar. 2 bar Ar decrease the emission current by an order of magnitude compared to emission in vacuum. The emission current is observed to decrease exponentially with pressure. The energy dispersion of the emitted electrons is measured using a customized HemiSpherical Analyzer (HSA) setup. The emitted electrons are emitted in a narrow peak (FWHM 0.3-0.5 eV) moving up in energy proportional to the bias voltage. A tail of scattered electrons extend from the main peak towards the work function edge of the emission spectra. The MIS hot electron

emitter devices are heated using a direct current of 0.3 A through a 20 nm Pt gate metal layer and the temperature is monitored using the calibrated resistance of the metal layer. The MIS hot electron emitters are cleaned in-situ in a background pressure of 3×10^{-7} mbar O_2. Thermal desorption experiments with labeled CO are carried out with a reproducibility of 7%. The detection limit of labeled CO for the mass spectrometer setup is estimated to 3×10^9 s^{-1} from the desorption experiments. The theoretical hot electron induced desorption rate is estimated to $2{\times}10^4$ s^{-1}.

Resumé

En Metal-Isolator-Halvleder (MIS, eng.) baseret komponent udvikles til undersøgelse af kemi forbedret vha. varme elektroner. En modelbeskrivelse af komponenten præsenteres, som beskriver de vigtigste koncepter af funktionaliteten og karakteristika for komponenten. MIS komponenten fremstilles ved brug af rentrumsteknologi og processeringsfremgangsmåden beskrives. En Ultra Højt Vakuum (UHV) opstilling er modificeret til udførsel af eksperimenter med elektron emission fra varm elektron emittere og varm elektron kemi. Simuleringer viser vigtigheden af at holde oxidruhed og tykkelsesvariationer til et absolut minimum. Tunneloxiden karakteriseres ved brug af strøm-spændings (IV) og kapacitans-spændings (CV) karakteristikker for at kunne uddrage tunnelbarrierens tykkelse. Den veksler omkring de forventede 50 Å fra 44.7 Å til 58 Å. IV og CV-karakteristikkerne er korrelerede, men en forskel i oxidtykkelse opnås, hvilket indikerer en vis grad af rughed. Elektron emission bliver realiseret fra komponenterne til en opsamligsplade. Emissionen under 5 V varierer fra måling til måling, men er stabil over 5 V. Arbejdsfunktionen bliver sænket vha. Cs til 2 eV og emitterede elektroner observeres fra en forspænding på 2 V. Den maksimale observerede emissions effektivitet på 8% opnås ved en forspænding på 3 V på den Cs dækkede emitter. Den middel frie vejlængde i Au for 5 eV elektroner uddrages fra emissionsmålingerne til 52 Å, hvilket er i fremragende overensstemmelse med andre eksperimenter. Titan vædningslaget er et vigtigt spredningscenter for elektroner, som tunnelerer igennem oxiden. Et 1 nm Titan vædningslag reducerer elektron emissions effektiviteten med en faktor 10. Elektron emission bliver observeret under atmosfærisk lufttryk og i op til to bar Ar tryk. To bar Ar reducerer emissionsstrømmen med en størrelsesorden i forhold til under vakuum. Emissionsstrømmen falder eksponentielt med trykket. De emitterede elektroner's energi spektrum måles vha. en modificeret elektrostatisk halvkugle analysator opstilling. Elektronerne emitteres i en smal energi top (FWHM 0.3-0.5 eV), som flytter sig mod højere energier proportionalt med forspændingen over komponenten. En hale af spredte elektroner strækker sig fra toppen ned mod arbejdsfunktionskanten af elektronemissionsspektret.

Varm Elektron Emittererne opvarmes ved at sende en jævnstrøm på 0.3 A gennem en 20 nm Pt metalfilm på forsiden af komponenten og temperaturen overvåges ved at måle modstanden i metalfilmen, som kalibreres til en temperatur. Varm elektron emitterne renses in-situ i et baggrundstryk af O_2 på 3×10^{-6} mbar. Termiske desorptionsekperimenter med isotopmærket CO udføres med en reproducerbarhed på 7%. Detektionsgrænsen for mærket CO for massespektrometeropstillingen estimeres til 3×10^9 s^{-1} fra desorptionsekperimenterne. Den teoretiske varm elektron inducerede desorptionsrate estimeres til $2{\times}10^4$ s^{-1}.

Contents

1 Introduction **1**

2 Hot Electron Surface Chemistry **3**

2.1 The DIET and DIMET Regimes 5
2.2 A Theoretical Approach to DIET 6

3 Physics of the MIS Structure **9**

3.1 The MIS Structure 10
3.1.1 Semiconductor Charge Density 12
3.1.2 Electron and Hole Concentrations 13
3.1.3 Concentration of Ionized Donors and Acceptors 13
3.1.4 Determining the Equilibrium Fermi Level 14
3.2 The MIS Capacitor 14
3.2.1 Capacitance Voltage Characteristics 17
3.3 Transport in the Insulator 18
3.3.1 The Tunnel Current 21
3.3.2 The WKB approximation 21
3.3.3 Transmission Probability for Trapezoidal and Triangular Barriers 22
3.3.4 Correction for the Image Charge Potential 23
3.3.5 The Supply Function 25
3.3.6 Energy Distribution of Tunneling Electrons 27
3.3.7 IV Characteristics 28
3.4 Self-Consistent Solution to Poisson's Equation 30
3.4.1 CV characteristics from Self-Consistent Solutions . . . 34
3.4.2 IV characteristics from Self-Consistent Solutions 35

4 Fabrication **37**

4.1 Implementation of the MIS Hot Electron Emitter 37
4.1.1 Process Overview 41
4.2 Process Sequence 41

5 Ultra High Vacuum Setup **45**

6 Tunnel Barrier Thickness and Variations **49**
6.1 Roughness 50
6.2 Experimental 55
6.2.1 CV Measurements 55
6.2.2 CV data and Modeling 58
6.2.3 IV Data 59
6.2.4 Fowler Plots 60
6.3 Thickness Variation 62
6.4 Length Scales of the Thickness Variation 64

7 Electron Emission **67**
7.1 Total Emission Current 68
7.2 Electron Emission from Cesiated Au 70
7.3 Extraction of the Mean Free Path 72
7.4 Influence of the Ti Wetting Layer 75
7.5 Overview of Emission Efficiencies 77
7.6 Electron Emission in Air 78

8 Electron Energy Dispersion **81**
8.1 Experimental Setup 81
8.2 Energy Band Diagram 85
8.3 Electron Emission Energy Spectra 85

9 Towards Hot Electron Chemistry **91**
9.1 Choice of Test System 91
9.2 Heating and Temperature Monitoring 92
9.3 Cleaning Platinum 95
9.4 Thermal CO Desorption 101
9.5 Detection Limit 103
9.6 Hot Electron Induced Desorption Rates 104

10 Conclusion **107**

A Symbols **111**

B Abbreviations **115**

C Numerical Implementation **117**

D Process as implemented in the Danchip Cleanroom **119**

E Calibration of Metal Layer Thickness **121**

F List of Publications **131**

Chapter 1

Introduction

The main motivation for this thesis was the possibility of enhancing the chemical reactivity of surfaces by the use of hot electrons. Hot electrons are electrons excited from a fraction of- to several electron volts above the Fermi level of the surrounding environment. By exciting electrons several electron volts above the Fermi level with energies above the range of typical molecular binding energies and diffusion energies it was speculated [1, 2, 3] that these hot electrons could inelastically scatter and deposit a fraction of their energy in the vibrational degrees of freedom of an adsorbate on the surface and induce a chemical reaction.

In the past decades substantial scientific research have been conducted within heterogeneous catalysis. With the advent of Ultra High Vacuum (UHV) it became possible to study atomically clean surfaces for several hours at a time, which is an important prerequisite for modern surface science. The research have taught us about eg. binding sites, coverage isotherms and reaction barriers. It is the interaction between electronic states, which decides the physical properties such as desorption energies and reaction barriers.

Another great important realization within the realm of heterogenous catalysis and chemistry in general is the Sabatier principle [4]. The main point in this principle is that the optimal materials choice for catalyzing a given chemical reaction, in terms of reactivity, will always be a compromise. In the case of heterogenous catalysis the material chosen should be the optimum compromise between activating the reactants while not binding the products too strongly. In the case of a metal that cannot activate the reactants no reaction will occur, on the other will an excessively reactive metal bind the products too strong leading to self-poisoning of the catalyst in the way that no free reaction sites will be available for further products to be produced.

Within the paradigm of traditional heterogeneous catalysis there is no

way to get around Sabatier's principle. Hot electrons could be a way to select the bonds to activate by injecting hot electrons into specific unoccupied resonances in adsorbates on the surface. This is perhaps a very ambitious vision, lying years in the future. On the short time scale investigation of hot electron chemistry can give new information on how exited electrons interact with adsorbates. Such insight can be employed for better understanding of photo-catalysis and other systems where excited electrons are present.

In this thesis the focus is on fabrication and characterization of a Metal-Insulator-Semiconductor (MIS) structure based hot electron emitter and the work towards applying it for hot electron enhanced chemistry. There are several challenges which must be met before the stage is set to investigate hot electron chemistry efficiently and reliably. During the work of this thesis many of these challenges have been faced and met, but some challenges still remain. Some of the topics this thesis deals with are design and fabrication of MIS structures suited as hot electron emitters, characterizing the yield and energy distribution of hot electrons from these devices, selecting metal and molecules for early studies of hot electron chemistry, obtaining an atomically clean surface to be used as the template for hot electron chemistry, etc. The focus has been on pushing forward towards the final goal of enabling hot electron chemistry on a MIS based hot electron emitter. During this work we have gained awareness of many new challenges and possibilities which have made this thesis a very broad piece of work spanning many areas within applied physics. Many spin-off projects have been proposed, such as using the MIS structures for electron emitters and detectors of excited carriers produced by ion bombardment [5, 6] and chemical reactions [7, 8].

The outline of this thesis is as follows: A short overview of hot electron chemistry is given in chapter 2 introducing the basic concepts of hot electron adsorbate interaction and sources for hot electrons. Furthermore some theoretical results from our collaborating theoretical subgroup are summarized. In chapter 3 the basic physics of the MIS structure is introduced along with a self-consistent model explaining key features of the MIS structure as an electron emitter. In chapter 4 the design of the MIS hot electron emitter and the fabrication process is presented. Chapter 5 focus on the experimental UHV setup that has been used to obtain many of the results presented in this thesis. Chapter 6 deals with the electrical characterization of the tunnel barrier of the MIS hot electron emitter. In chapter 7 and 8 results covering the electron emission from the MIS hot electron emitter are presented. The efforts towards experiments with surface chemistry enabled by hot electrons are treated in chapter 9, and finally a conclusion summarizing the most important results and achievements from the work presented in this thesis is given in chapter 10.

Chapter 2

Hot Electron Surface Chemistry

In the later years there have been a growing interest in non-thermal interaction between charge carriers and reactants. Traditionally the focus in theoretical and experimental heterogeneous catalysis has been on understanding the interaction of adsorbates with surfaces by assuming the electronic configuration to be in the ground state at every step of the reaction pathway. The underlying assumption is that the electrons equilibrate on a timescale orders of magnitudes faster than the movement of the nuclei. This is the Born-Oppenheimer approximation [9]. Another way to express this is that reactions occur in the adiabatic limit without energy exchange with the surrounding environment. For a bulk of chemical reactions this approximation is a good one yielding precise theoretical estimates on parameters such as binding energies and energy barriers for surface diffusion.

For some classes of interactions at surfaces, however, the adiabatic picture breaks down. This is the case where energy is dissipated as hot electrons [10, 11], exo-electrons [12] or photons [13] from elementary exothermal reactions such as adsorption or reaction. Examples of studies of these effects both theoretically and experimentally are plentiful in the literature. The original motivation for this project was not to detect hot charge carriers, but to create hot electrons which could activate chemical surface reactions by injecting energy directly into the reaction coordinate, ie. a specific molecular bond. In the literature there are several examples on activating chemical reactions using excited carriers, such as in photocatalysis [14], Electron Stimulated Desorption (ESD) [15], desorption induced by Femto-second lasers [16, 17, 18] and Scanning Tunnel Microscope (STM) probes [19, 20].

With the advent of femto-second lasers new results for photo desorption emerged [16, 17] which pioneered a substantial increase in focus on non-

adiabatic interaction between hot electrons and adsorbates. The proposed reaction mechanism for this class of experiments is that photons are exciting hot electrons in the substrate that interact with unoccupied resonant energy levels on the adsorbate. The occupation of a resonance level by a substrate electron changes the equilibrium Potential Energy Surface (PES) from the neutral situation to a temporal negative ion situation of the composite adsorbate molecule and hot electron system. The PES of the excited state exerts a force on the excited molecule. In the case enough energy is transferred from the hot electron to the intra molecular degrees of freedom to overcome the activation barrier the molecule will desorb, dissociate or react. The amount of energy transferred from the hot electron to the adsorbate is governed by the lifetime of the resonance or the resonance width[21, 18].

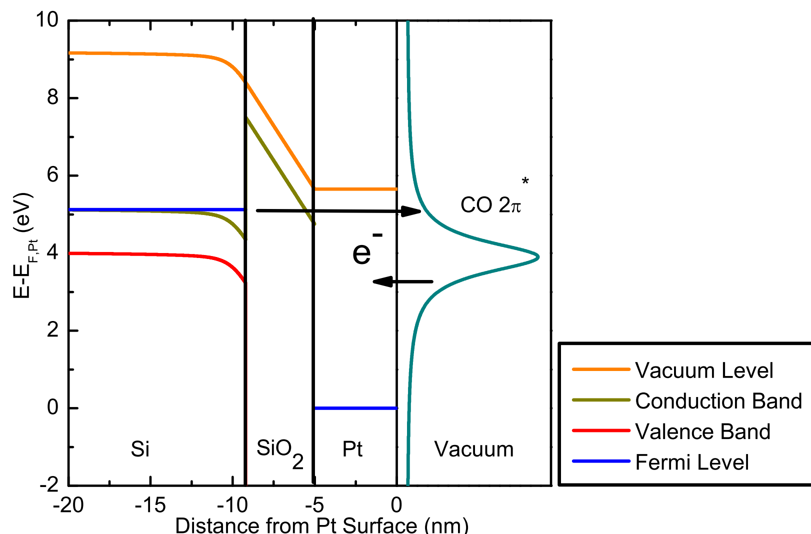

Figure 2.1: A schematic energy diagram for a MIS hot electron device made up of Si, SiO_2 and Pt. The Pt layer is the reaction template. Electrons tunnel ballistically through the insulator into the metal layer due to the positive bias voltage of 5 V. The ballistic electrons then scatter inelastically on the resonance of the unoccupied 2π antibonding orbital catalyzing desorption.

An alternative approach to hot electron chemistry was suggested by J. W. Gadzuk. He proposed to utilize a Metal-Insulator-Metal (MIM) tunnel device as a source for hot electrons [22, 1, 2, 3]. A great feature of the MIM device is that the tunneling electrons injected from one metal electrode to the other has a very narrow energy distribution around a mean energy given

by the bias voltage across the insulator. The tunneling electrons stem from the Fermi level in one of the electrodes. Towards high energies the electron distribution is determined by the Fermi tail, while towards the low energy side the energy distribution is limited by the exponential decrease in tunnel probability with energy. Work on applying MIM devices and hot electrons for redox electrochemistry [23, 24] and for decomposition of relatively large molecules on surfaces [25, 26] have already been presented in the literature.

We adopted this interesting idea of creating a hot electron chemistry device with a built-in narrow band source of hot electrons, but as a Metal-Insulator-Semiconductor (MIS) device. In Fig. 2.1 a schematic view of the energy diagram of the MIS-adsorbate system. A very interesting feature of a MIS hot electron device is the possibility of directing energy directly and selectively into unoccupied molecular orbitals by tuning the bias voltage across the insulator of the device [2].

2.1 The DIET and DIMET Regimes

In the literature most effort have been spent on investigating desorption by hot electrons as opposed to reaction. There are two main regimes of desorption induced by hot electrons, they are: Desorption Induced by (Multiple) Electronic Transitions (DIET) [27] and (DIMET) [28]. In DIET the energy needed to induce a desorption event is delivered to the adsorbate by a single electron transition event. The desorption rate has a threshold when the hot electron energy deposited in the resonance surmounts the desorption energy and is directly proportional to the influx of hot electrons. For the DIMET situation there is no threshold energy, since the desorption event can in principle be excited by an infinite amount of low energy electronic transitions. The excitation by multiple electronic transitions lead to a power law dependence of the desorption rate on the influx of hot electrons [29].

Very few techniques are able to probe the DIMET regime due to the extreme fluxes of hot electrons needed. The influx of hot electrons will compete with molecular de-excitation which occur on a time-scale of pico-seconds [29]. The most widespread technique to induce DIMET is femtosecond lasers illuminating metal surfaces for which the power law desorption rate as a function of photon flux and thereby hot electron flux have been observed [16].

In relation to the MIS hot electron devices presented in this thesis there is no question that the DIET regime is what will be probed. The highest current density achieved by our devices lie in the range of 1 A cm^{-2} which would yield a hot electron event per adsorbed molecule per ∼0.1 ms [1]. Nowhere

[1] Assuming a coverage of molecular adsorbates of 1 monolayer and an adsorption site

near the flux required to achieve multiple excitations of an adsorbate within a pico-second.

2.2 A Theoretical Approach to DIET

Parallel to the experimental work carried out in our group during this thesis another subgroup[2] has been working on quantifying reaction yields for hot electron interaction with adsorbate species. Here a short overview of their results related to this thesis will be given.

Their theoretical work is based on results obtained using Density Functional Theory (DFT) with some important modifications. The basis of DFT is to obtain the ground-state charge density self-consistently. In 1964 Hohenberg and Kohn proved that the total energy of the nuclear system is a unique functional of the charge density [30]. By comparing the total energy of selected geometric configurations, physical quantities such as binding energies and forces can be obtained. By mapping out the forces on a molecule as a function of internal degrees of freedom, such as eg. Center-of-mass motion and internal vibrational modes, the molecular PES can be obtained. However Hohenberg and Kohn's proof is only valid for the ground state, why DFT is limited to description of systems in thermal equilibrium. A description of Hot Electron Chemistry and DIET must inherently include excited states. The PES of the excited adsorbates is treated by forcefully occupying desired molecular orbitals above the Fermi level in the self consistency loop of the calculations. The electron occupying the excited state is taken from the Fermi level and the excited states to occupy is obtained from the last iteration. This modified version of DFT is called linear expansion ΔSCF-DFT [21].

Using the PES of the ground state and the excited states, the desorption probability of a given resonance can be calculated [31]. In Fig. 2.2 the desorption rate of CO from Pt(111) has been calculated for the 2π antibonding orbital. The desorption probability has been calculated for four values of the resonance width (Γ) and a desorption energy of 1.37 eV[32]. The typical resonance width is on the order of 1 eV which give a maximum desorption probability per inelastic electron scattering event close to 10^{-5} for a hot electron de-tuned 0.6 eV above the resonance energy of 3.9 eV. The reason for the maximum in desorption probability being de-tuned can be understood as the compromise where both the incoming and outgoing electron is closest to the resonance energy [31]. This result suggest that in order to desorb CO

density of 10^{15} cm^{-2}

[2]The subgroup consists of Ph.d. students Thomas Olsen and Jeppe Gavnholt and Associate Professor Jacob Schiøtz.

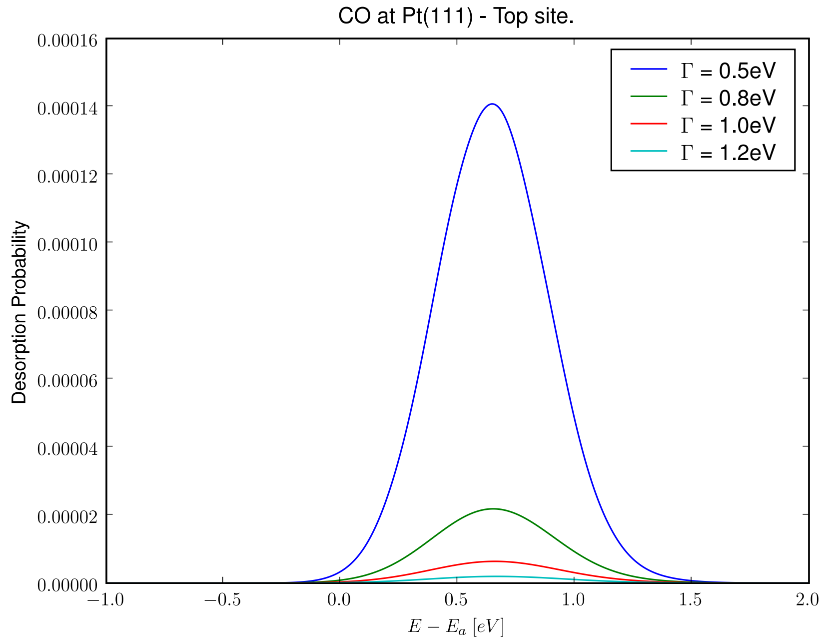

Figure 2.2: The calculated desorption probability as a function of the kinetic energy of the hot electron relative to the center of the resonance. The 2π resonance, considered here, lies 3.9 eV above the Fermi level of Pt. The maximum desorption probability of 10^{-5} is achieved for electrons de-tuned 0.6 eV above the energy of the resonance. Source: Thomas Olsen.

from Pt using hot electrons from a MIS device, the device should be biased with 4.5 V. This result is very important result and it furthermore indicates that only electrons with an energy ± 0.6 eV around 4.5 eV will contribute to the desorption rate of CO.

Chapter 3

Physics of the MIS Structure

The objective of this project, as mentioned, is to investigate the possibility of applying Metal-Insulator-Semiconductor (MIS) structures as a source for excited electrons for hot electron chemistry.

In order to pursue the objective and tailor the parameters of the fabricated MIS structure based devices a base of knowledge about the physics of the MIS structure must be compiled. This section contains the relevant information for understanding how electrons are excited by the MIS structure to become hot electrons. Poisson's equation is solved for the semiconductor part of the MIS structure to predict the capacitance voltage (CV) characteristics of the structure. The CV characteristics is used to extract the insulator thickness experimentally. Furthermore a walk-through of the nature of tunnel transport through the insulator barrier is given in order to be able to predict the current density as a function of bias voltage, the current voltage (IV) characteristics. The reaction rate of a reaction driven by hot electrons will be proportional to the current density of hot electrons, why the IV characteristics is the most important parameter of a MIS structure with respect to hot electron chemistry.

The MIS structure is a layered structure of three different materials; a semiconductor, an insulator and a metal layer. These three materials are fundamentally different from a solid-state physics point of view. Especially the interfaces between the different materials lead to interesting physics, these are the so-called heterojunctions. The MIS structure consists of two heterojunctions; The interface between the semiconductor and the insulator and between the insulator and the metal layer.

The MIS structure has throughout this project been implemented by highly n-doped Si as the semiconductor, SiO_2 as the insulator, and a metal layer, often Pt. In the following analysis this materials selection will be used for simplicity and relevance.

3.1 The MIS Structure

The three materials that comprise the MIS structure can be described using band diagrams as seen in Fig. 3.1. The metal layer is characterized by a Fermi- and a vacuum level, the insulator and the semiconductor furthermore have a valence- and conduction band. The distance in energy from the Fermi level to the vacuum level is the work function, of the material. For the semiconductor and the insulator the electron affinity is the distance from the conduction band edge to the vacuum level. The vacuum level is the common reference when the materials are not connected.

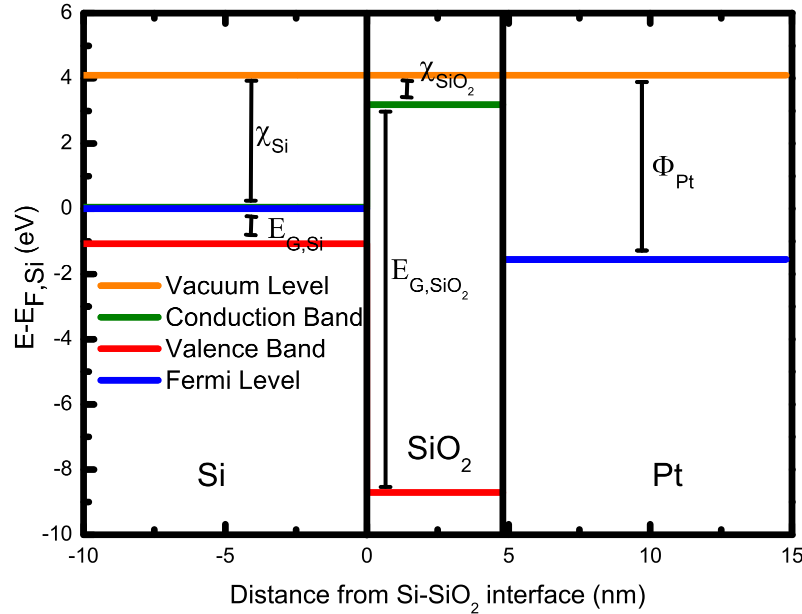

Figure 3.1: The MIS structure is made up of three materials; Si as the semiconductor, SiO_2 as the insulator, and Pt as the metal layer. χ denotes the electron affinity, E_G the band gap, E_F the Fermi level, E_V the valence band, E_C the conduction band, E_{Vac} the vacuum level, and Φ the work function.

The MIS structure can be connected with flat bands, see Fig. 3.2 A, which is the simplest situation. Due to the difference in workfunction between the semiconductor and the metal layer there is a difference in Fermi level between the two materials which yields a voltage equal to this difference across the insulator, which is the flat band voltage. In the flat band situation the voltage

equals, but with opposite sign, the built in potential from the work function difference and there is no net electrical field in the structure.

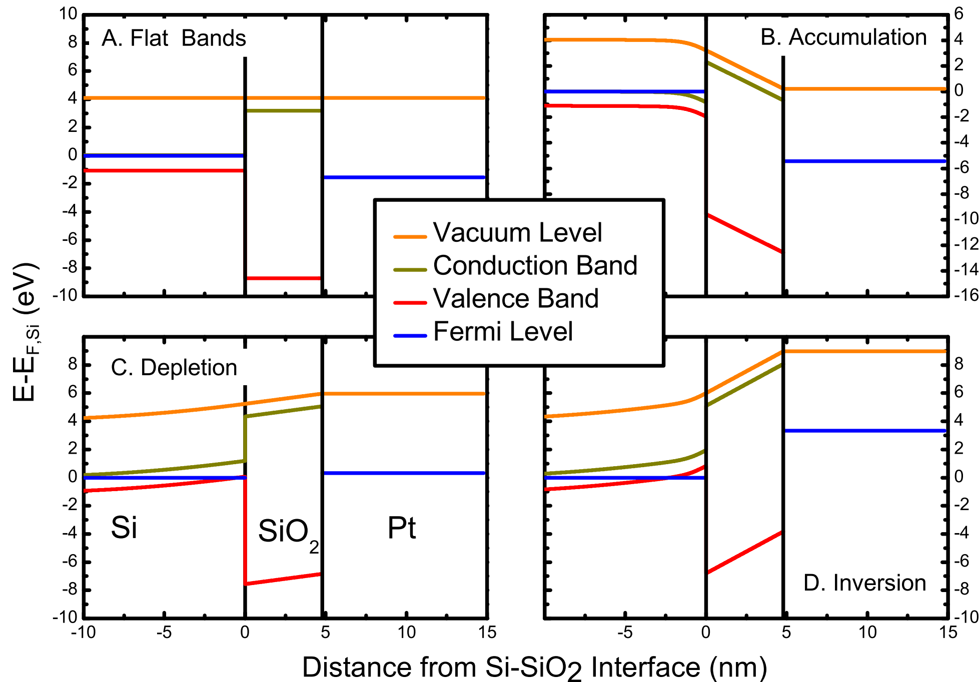

Figure 3.2: A) The MIS structure at Flat Band Condition. The applied bias voltage equal the difference in work function between the semiconductor and the metal. B) Accumulation; a positive surface potential creates an accumulation layer of electrons at the insulator interface. C) Depletion; A small negative surface potential depletes the semiconductor insulator interface for electrons and the only charge available at the interface is the ionized donors. D) Inversion; An inversion layer of holes is created at the semiconductor insulator interface due to a large negative surface potential.

In the case where a positive bias voltage is applied to the metal film compared to the semiconductor, denoted forward bias, the free charge carriers in the semiconductor are attracted to the insulator interface where they form an accumulation layer, see Fig. 3.2 B. Due to the limited amount of states a positive potential in the semiconductor is needed to gather enough electrons to the interface to create the remaining potential drop across the insulator. This positive potential makes the bands bend downwards at the insulator

interface. The potential at the interface of the semiconductor and the insulator is known as the surface potential. Due to the surface potential the entire bias voltage is not dropped across the insulator alone, but is divided between the semiconductor, and the insulator, and is relative to the flat band voltage. Eq. 3.1 show how the bias voltage is distributed in the MIS structure:

$$V_{\mathrm{Bias}} = V_{\mathrm{I}} + \psi_S + V_{\mathrm{FB}} \tag{3.1}$$

where V_{Bias} is the externally applied bias voltage, V_{I} is the voltage dropped across the insulator, ψ_S is the surface potential, and V_{FB} is the flat band voltage.

When a negative bias is applied to the metal film of the MIS structure electrons are repelled from the semiconductor insulator interface by the negative potential on the metal film. A negative surface potential is set up due to the limited positive charge supplied by the ionized donors in the semiconductor, see Fig. 3.2 C. This situation is called depletion since the majority carriers (electrons in an n-type semiconductor) are depleted from the semiconductor insulator interface.

A third situation is possible referred to as inversion. In inversion the electrons are repelled from the semiconductor insulator interface by a large negative bias voltage applied to the metal layer. A so-called inversion layer of holes is formed due to the large negative surface potential, see Fig. 3.2 D.

3.1.1 Semiconductor Charge Density

The amount of charge available in the semiconductor determines the electronic properties. The Fermi level is determined by assuming charge neutrality in the bulk of the semiconductor. The charge in the semiconductor come from several sources; electrons, holes, and ionized donors and acceptors. The total charge density can be written as the sum of the individual contributions:

$$\frac{\rho(x)}{q} = p_0 - N_A^- - n_0 + N_D^+ \tag{3.2}$$

where $\rho(x)$ is the charge density as a function of distance, q is the elementary charge, p_0 and n_0 are the hole and electron concentrations respectively and N_A^- and N_D^+ are the concentrations of ionized acceptors and donors respectively.

3.1.2 Electron and Hole Concentrations

To acquire the electron and hole concentrations the density of states must be multiplied by the fermi distribution and integrated over the relevant energy range:

$$n_0 = \int_{E_C}^{+\infty} g_C(E) f_{fd}(E - E_F) dE \text{ and } p_0 = \int_{-\infty}^{E_V} g_V(E)(1 - f_{fd}(E - E_F)) dE \tag{3.3}$$

where E_F is the Fermi level, E_C and E_V are the conduction and valence band edge respectively, while g_V and g_C are the density of states in the valence and conduction band respectively and are given by[33]:

$$g_C(E) = \frac{8\pi\sqrt{2}}{h^3} m_c^{*3/2} \sqrt{E - E_C} \text{ and } g_V(E) = \frac{8\pi\sqrt{2}}{h^3} m_v^{*3/2} \sqrt{E_V - E} \tag{3.4}$$

where h is Planck's constant and m_c^* and m_v^* are the effective density of states masses of electrons and holes respectively.

Using the Fermi integral of order 1/2 Eq. 3.3 can be rewritten as:

$$n_0 = N_C \mathcal{F}_{\frac{1}{2}}(E_F - E_C) \text{ and } p_0 = N_V \mathcal{F}_{\frac{1}{2}}(E_V - E_F) \tag{3.5}$$

where N_C and N_V are the effective density of states of the conduction and valence band respectively, given as:

$$N_C = 2\left(\frac{2\pi m_c^* k_B T}{h^2}\right)^{3/2} \text{ and } N_V = 2\left(\frac{2\pi m_v^* k_B T}{h^2}\right)^{3/2} \tag{3.6}$$

where T is the temperature and k_B is Boltzmann's constant. $\mathcal{F}_{\frac{1}{2}}(\eta)$ is the Fermi Integral of order 1/2 defined as:

$$\mathcal{F}_{\frac{1}{2}}(\eta) = \frac{2}{\sqrt{\pi}} \int_0^{+\infty} \frac{\sqrt{x}}{1 + e^{x-\eta}} dx \tag{3.7}$$

3.1.3 Concentration of Ionized Donors and Acceptors

The concentrations of ionized donors and acceptors are given by the impurity concentration multiplied by the ionization probability of the given impurity.

$$N_D^+ = N_D \cdot f_D(E_D - E_F) \text{ and } N_A^+ = N_A \cdot f_A(E_A - E_F) \tag{3.8}$$

where N_D and N_A are the donor and acceptor impurity concentrations respectively, and E_D and E_A are the respective ionization energies. f_D and f_A are the donor and acceptor ionization distributions given by[33]:

$$f_D(E_D) = 1 - \frac{1}{1 + \frac{1}{2}e^{\frac{E_D - E_F}{k_B T}}} \text{ and } f_A(E_A) = \frac{1}{1 + 4e^{\frac{E_A - E_F}{k_B T}}} \tag{3.9}$$

3.1.4 Determining the Equilibrium Fermi Level

Now that the concentration of charges in the semiconductor can be calculated using Eq. 3.2 and the equations for the concentrations of the different types of charge carriers, the Fermi level of the semiconductor can be determined. Charge neutrality must exist in the bulk of the semiconductor and the Fermi level is determined as the value that will satisfy this condition:

$$0 = p_0(E_F) - N_A^-(E_F) - n_0(E_F) + N_D^+(E_F) \tag{3.10}$$

Eq. 3.10 can be solved numerically or graphically as the interception between the concentration of holes and ionized donors and the concentration of electrons and ionized acceptors as can be seen in Fig. 3.3.

3.2 The MIS Capacitor

In order to model the electronic properties of the MIS structure as a whole a good description of the semiconductor is mandatory. The surface potential and -charge are important to obtain, since these are necessary to calculate the voltage drop across the insulator and the total capacitance of the MIS structure as a function of external bias voltage.

Poisson's equation is used to obtain the relationship between the charge and potential in the semiconductor:

$$\frac{d\psi^2}{dx^2} = -\frac{\rho(x)}{\epsilon_r} \tag{3.11}$$

where ψ is the potential, ϵ_r is the permittivity of the semiconductor, and $\rho(x)$ is the charge density.

In the bulk of the semiconductor $x = +\infty$ charge neutrality must exist, otherwise free carriers would flow due to electrical fields to reestablish this charge neutrality, the potential in the semiconductor bulk is defined as 0:

$$\rho(+\infty) = 0 \rightarrow \psi(+\infty) = 0 \rightarrow E(+\infty) = 0 \tag{3.12}$$

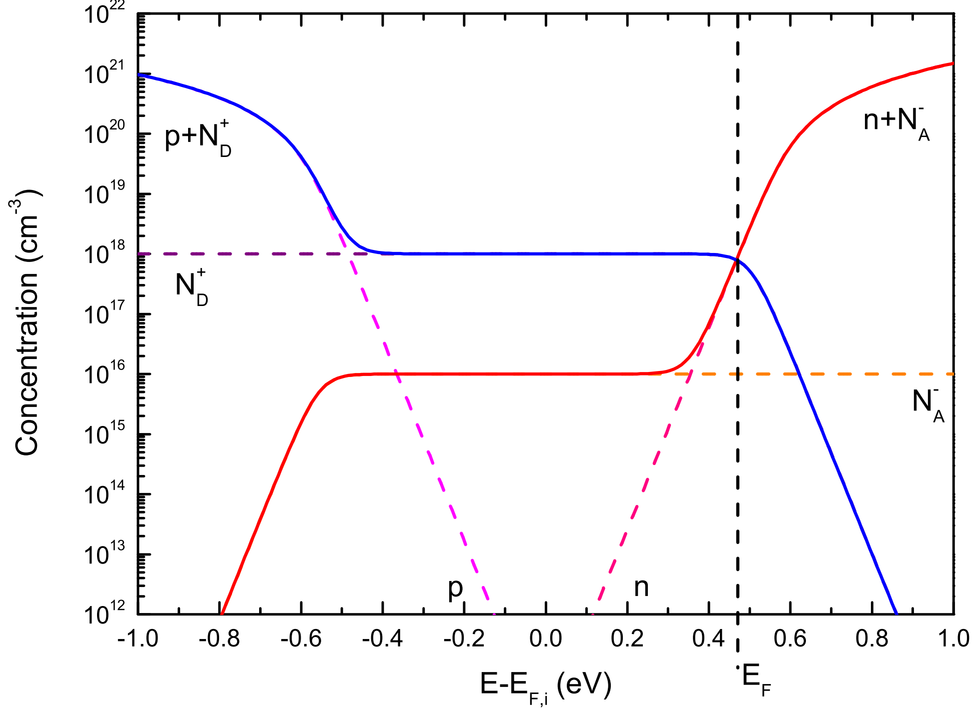

Figure 3.3: The concentration of electrons, ionized acceptors, holes, and ionized donors are shown as a function of the Fermi level. The Fermi level in the bulk of the semiconductor must yield charge neutrality and is therefore given by the interception of the two solid curves corresponding to holes and ionized donors (blue) and electrons and ionized acceptors (red) respectively. The x-axis is relative to the intrinsic Fermi level of undoped silicon. In this example the donor concentration is 10^{18}cm^{-3} of antimony (Sb) with an ionization energy of 40 meV. The acceptor concentration is 10^{16}cm^{-3} of boron (B) with an ionization energy of 45 meV.

Eq. 3.11 is multiplied on both sides by $\frac{d\psi}{dx}$ and integrated from the bulk to the semiconductor surface at the insulator interface. This yields:

$$\int_{+\infty}^{x} \left(\frac{d\psi}{dx}\right) \frac{d}{dx}\frac{d\psi}{dx} dx = -\int_{+\infty}^{x} \frac{\rho(x)}{\epsilon_r}\frac{d\psi}{dx} dx \qquad (3.13)$$

In order to obtain the electric field as a function of the potential a change of variables is carried out. For the left side of Eq. 3.13 $x \rightarrow \frac{d\psi}{dx}$ and for the right side $x \rightarrow \psi$:

$$\int_0^{\frac{d\psi}{dx}} \Big(\frac{d\psi}{dx}\Big) d\Big(\frac{d\psi}{dx}\Big) = -\int_0^{\psi} \frac{\rho(\psi)}{\epsilon_r} d\psi \tag{3.14}$$

Carrying out the integration on the right side and using the relation between electric potential and field $\frac{d\psi}{dx} = -\varepsilon$ results in:

$$\left[\frac{1}{2}\Big(\frac{d\psi}{dx}\Big)^2\right]_0^{-\varepsilon} = \frac{1}{2}\varepsilon^2 = -\int_0^{\psi} \frac{\rho(\psi)}{\epsilon_r} d\psi \tag{3.15}$$

Now the electric field can be obtained:

$$\varepsilon = \pm\sqrt{-2\int_0^{\psi} \frac{\rho(\psi)}{\epsilon_r} d\psi} \tag{3.16}$$

The charge concentration can be obtained from Eq. 3.2. In order to get the charge concentration Eq. 3.2 is combined with Eq. 3.8 and Eq. 3.5 where E_C is replaced by $(E_{C0} - q\psi)$ and E_V with $(E_{V0} - q\psi)$:

$$\begin{aligned} \rho(\psi) &= N_V \mathcal{F}_{\frac{1}{2}}(E_{V0} - E_F - q\psi) - N_A \cdot f_A(E_A - E_F - q\psi) \\ &- N_C \mathcal{F}_{\frac{1}{2}}(E_F + q\psi - E_{C0}) + N_D \cdot f_D(E_D - E_F - q\psi) \end{aligned}$$

By inserting the surface potential into the solution for the electrical field in Eq. 3.16 and multiplying with the permittivity for the semiconductor the charge at the semiconductor insulator interface is obtained from Gauss' law:

$$Q_S = -\epsilon_S \varepsilon_S \tag{3.17}$$

The charge at the semiconductor insulator interface must be balanced by an equal amount of charge of opposite sign at the metal insulator interface on the other side of the insulator to uphold charge neutrality.

The voltage drop across the insulator can be found as the ratio between the charge and the insulator capacitance:

$$V_{In} = \frac{-Q_S}{C_I} = \frac{-Q_S X_I}{\epsilon_I} \tag{3.18}$$

where C_I is the capacitance, X_I is the thickness, and ϵ_I is the permittivity of the insulator. Now Eq. 3.18 can be inserted into Eq. 3.1 and the relation between external bias voltage and surface potential becomes:

$$V_{\text{Bias}} = \frac{-Q_S(\psi_S) X_I}{\epsilon_I} + \psi_S + V_{\text{FB}} \tag{3.19}$$

To give an indication of the surface potential it is plotted against the bias voltage in Fig. 3.4 for different donor concentrations, and a flat band voltage of 0 V and an oxide thickness of 50 Å. It is important to remember the difference between the bias voltage and the insulator voltage when comparing experiments to models, since the models are often based on the insulator voltage.

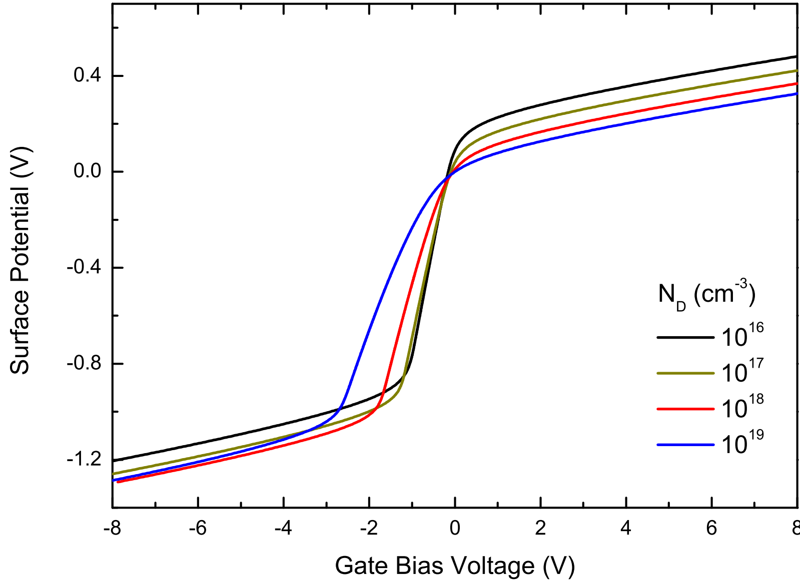

Figure 3.4: The surface potential of the semiconductor as a function of gate bias voltage for four different donor concentrations. As the donor concentration increase the surface potential is lowered under forward bias voltage, since less potential is needed to excite a given amount of electrons.

3.2.1 Capacitance Voltage Characteristics

Capacitance Voltage (CV) Characteristics have, along with the Current Voltage (IV) characteristics, been the most important electrical characterization tool working with the MIS structures in this project. CV measurements give access to a wide variety of valuable information such as; insulator thickness, dopant concentration, flat band voltage, and trap density[34].

The capacitance of the MIS structure is a series capacitance of the semiconductor capacitance and the insulator capacitance.

$$C_{\mathrm{MIS}} = \frac{1}{\frac{1}{C_I} + \frac{1}{C_S}} \tag{3.20}$$

where C_I is the capacitance of the insulator and C_S is the capacitance of the semiconductor. The insulator capacitance is the geometric capacitance of the insulator, assuming no trapped charge in the insulator:

$$C_I = \epsilon_I \frac{A}{X_I} \tag{3.21}$$

where A is the gate area. The capacitance of the semiconductor can be expressed as:

$$C_S = -\frac{\partial Q_S}{\partial \psi_S} \tag{3.22}$$

Using the results from the past sections theoretical CV characteristics can be obtained by calculating the surface charge of the semiconductor using Eq. 3.17 as a function of surface potential. From the surface charge the semiconductor capacitance is calculated and the MIS capacitance is obtained using Eq. 3.21. The bias voltage is then found by using Eq. 3.19 and finally the MIS capacitance can be plotted against the bias voltage, which is defined as the CV characteristics.

Based on the type of semiconductor and the dopant concentration and type the CV relationship for the MIS capacitance will change. In Fig. 3.5 some examples of varying the semiconductor donor and the resulting CV curves are shown.

3.3 Transport in the Insulator

The current voltage (IV) characteristics are performed to get information on the electrical integrity of the ultra-thin SiO_2 layer in the Hot Electron Emitter. First of all an IV measurement will decide whether the current transport is due to tunneling or other types of transport such as thermionic emission or ohmic conduction. For this reason the IV measurement is often the first type of measurement to be performed on a new device or a new batch of devices to test the functionality and quality. The IV characteristics yield information on the insulator thickness along with information about the quality of the insulator.

In order to create hot electrons in the metal layer of the MIS structure electrons must transport through the insulator ballistically. In the quantum process of tunneling, see Fig. 3.6 A., electrons approaching the energy barrier

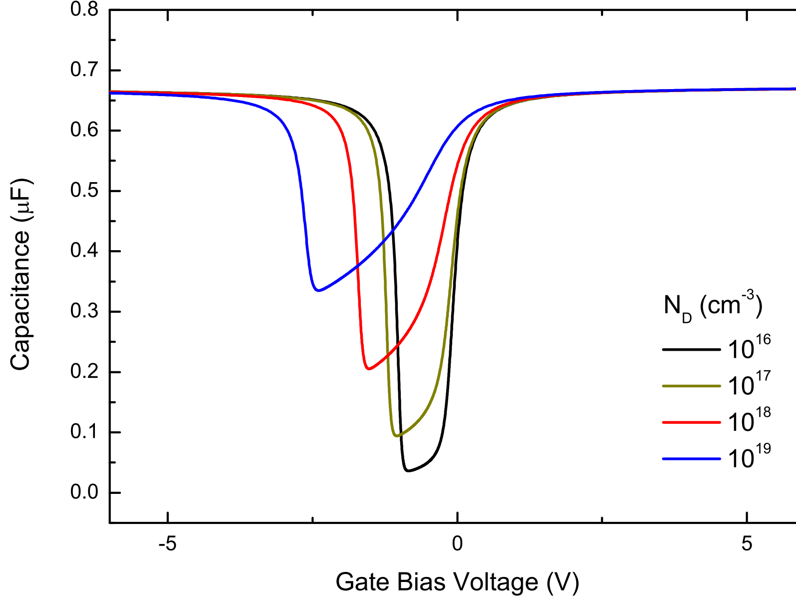

Figure 3.5: Capacitance Voltage (CV) characteristics as modeled for several values of the donor concentration N_D. For high donor concentrations the dip in the capacitance becomes shallower and broader due to the higher semiconductor capacitances as compared to lower concentrations of donors.

of the insulator have a finite probability of going through the barrier, even when the energy of the electrons is lower than the energy barrier. In this process the electrons are not scattered in the insulator but emerge on the other side of the barrier at the same energy level as they originated from. Due to the lower Fermi level in the new environment the electrons have a high kinetic energy and are termed hot electrons. The process of electrons tunneling directly across the energy barrier is called direct tunneling. By applying a large enough potential across the insulator the electrons can tunnel into the tilted conduction band of the insulator which decrease the effective tunneling distance, this is called Fowler-Nordheim tunneling [35], see Fig. 3.6 B. In the situation where a large enough bias voltage is applied to lower the vacuum level of the metal layer below the Fermi level of the semiconductor electrons are emitted to vacuum, see Fig. 3.6 C. In the following a simple model for the tunneling current will be derived.

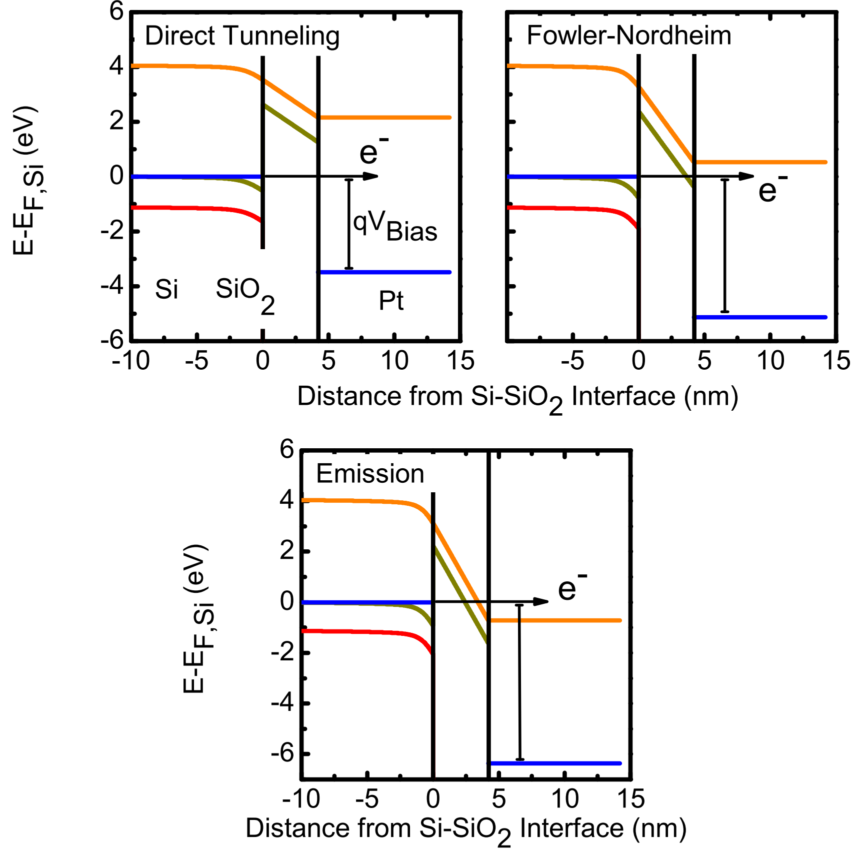

Figure 3.6: (Color convention as in Fig. 3.2) **A. Direct Tunneling.** A positive bias voltage is applied to the gate metal layer and the bands of the insulator tilts due to the potential across it. Electrons are tunneling directly from the semiconductor to the metal layer. In the metal layer they are hot electrons since the Fermi level is lowered due to the bias voltage across the insulator. **B. Fowler-Nordheim Tunneling.** The positive bias voltage on the metal gate is large enough to tilt the conduction band edge below the Fermi level of the semiconductor and electrons tunnel into the conduction band of the insulator. **C. Electron Emission.** The bias voltage is so large the vacuum level of the metal layer is pulled below the Fermi level of the semiconductor. Electrons tunneling into the conduction band of the insulator can escape to vacuum if they are scattered in the conduction band of the insulator and the metal layer.

3.3.1 The Tunnel Current

The tunnel current through the insulator can be separated into two basic parts; a transmission function and a supply function. The transmission probability is a strong function of energy and is the probability for an electron with a given transversal energy (x direction) to tunnel through the energy barrier of the insulator. The supply function yield the frequency of electrons impinging on the insulator energy barrier as a function of transversal energy. The tunnel current is obtained by integrating the supply function $N(E_x)$ multiplied by the transmission probability $T(E_x)$ over all relevant energies [36]:

$$J = \frac{4\pi m_S^* q}{h^3} \int_0^{+\infty} N(E_x)T(E_x)dE_x \tag{3.23}$$

where m_S^* is the effective mass in the semiconductor. The prefactor in front of the integral come from integration of the density of states in the y- and z-directions (longitudianl).

The supply and transmission functions can be modeled in many ways separately and then combined to form the expression for the current density. Here the transmission probability is approximated using the Wentzel-Kramers-Brillouin (WKB) approximation [37, 38, 39].

3.3.2 The WKB approximation

The transmission probability can be extracted from the time-independent Schrödinger equation[40, 41, 42]:

$$-\frac{\hbar^2}{2m^*}\frac{d^2\Psi}{dx^2} + qV(x)\Psi = E\Psi \tag{3.24}$$

where m^* is the effective mass, Ψ is the electron wavefunction, $V(x)$ is the potential, and E is the energy of the electron. Eq. 3.24 can readily be rewritten as:

$$\frac{d^2\Psi}{dx^2} = \frac{2m^*(qV(x) - E)}{\hbar^2}\Psi \tag{3.25}$$

The Schrödinger equation can be solved if we assume a slowly varying potential through the insulator. The wave function at x can be related to the wave function at $x + dx$ as:

$$\Psi(x + dx) = \Psi(x)\exp(-\int_x^{x+dx} k\ dx) \text{ with } k = \frac{\sqrt{2m^*(qV(x) - E)}}{\hbar} \tag{3.26}$$

Which is known as the WKB approximation [37, 38, 39] and holds for smoothly varying potentials of arbitrary shape. The transmission coefficient becomes:

$$T = \frac{\Psi(x+dx)\Psi^*(x+dx)}{\Psi(x)\Psi^*(x)} = \exp(-2\int_x^{x+dx} kdx) \tag{3.27}$$

3.3.3 Transmission Probability for Trapezoidal and Triangular Barriers

In order to apply the WKB approximation to the MIS structure the potential barrier must be approximated. The potential barrier electrons face in the MIS structure, Fig. 3.7, is set up by the forbidden energy range of the insulator band gap. The barrier height is the distance from the conduction band edge to the energy level of the approaching electron. The width of the barrier is the distance to the position where the potential is equal to or below the initial state. When a potential is applied across the insulator, the conduction band of the insulator is being tilted, which lowers the effective barrier for tunneling electrons, see Fig. 3.7.

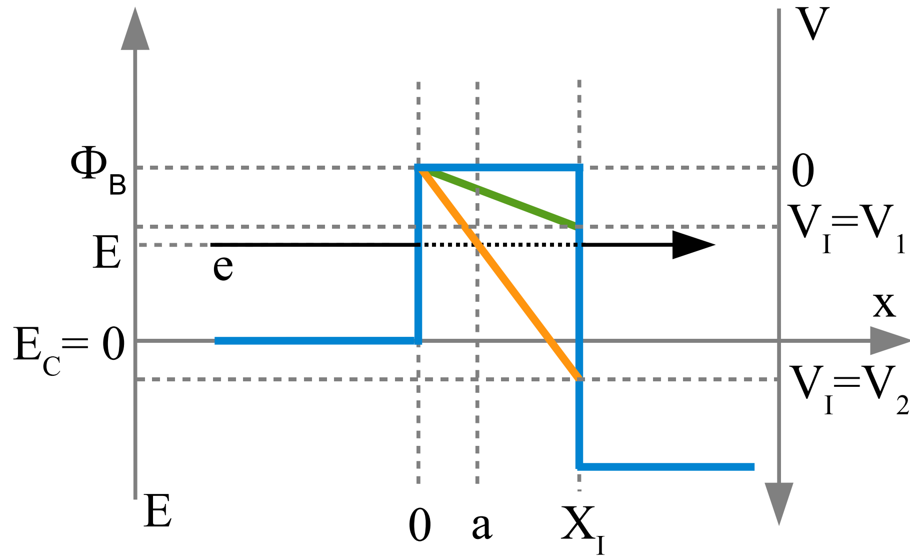

Figure 3.7: Diagram showing the potential barrier an electron of energy E see when approaching the insulator barrier from the semiconductor. The potential without applied voltage (blue) is due to the band gap in the insulator. For small insulator voltages (green) the barrier becomes a trapezoid and for larger voltages (orange) it becomes triangular.

For the trapezoidal barrier shown in Fig. 3.7 the potential can be written as:

$$qV(x) - E = \Phi_B - q\frac{V_I}{X_I}x - E \tag{3.28}$$

where V_I and X_I are the voltage across and the thickness of the insulator respectively. When inserted into the transmission probability, Eq. 3.27, it becomes:

$$T(E) = \exp\Big(-2\int_0^a \frac{\sqrt{2m_I^*(\Phi_B - q\frac{V_I}{X_I}x - E)}}{\hbar}dx\Big) \tag{3.29}$$

where m_I^* is the effective mass of the electron in the insulator, Φ_B is the height of the tunnel barrier, a is the distance where the potential barrier becomes equal to or below the starting energy level. For a trapezoidal barrier the distance is the insulator thickness ($a = X_I$) and the integral in Eq. 3.29 can be solved to yield a closed expression for the transmission probability:

$$T(E) = \exp\Big(-\frac{B(\Phi_B - E)^{3/2}X_I}{V_I}\Big)\exp\Big(\frac{B(\Phi_B - E)^{3/2}X_I}{V_I}\big(1 - \frac{qV_I}{\Phi_B - E}\big)^{3/2}\Big) \tag{3.30}$$

where $B = \frac{4}{3}\frac{\sqrt{2qm_I^*}}{q\hbar}$. In the case of a triangular barrier the distance a is given by:

$$q\Phi_B - q\frac{V_I}{X_I}a - E = 0 \implies a = -\frac{(E - \Phi_B)X_I}{qV_I} \tag{3.31}$$

Inserting into Eq. 3.29 yield the transmission probability for the triangular shaped barrier:

$$T(E) = \exp\Big(-\frac{B(\Phi_B - E)^{3/2}X_I}{V_I}\Big) \tag{3.32}$$

From Eq. 3.32 and Eq. 3.30 it is seen that the transmission probability is strongly dependent on both energy of the electron and the applied voltage.

3.3.4 Correction for the Image Charge Potential

A simple but quite important modification to the potential barrier shape is to take the image charge potential into account. The image charge potential is due to the image charge the tunneling electron see in the electrodes while

tunneling through the insulator. Taking all the image charges into account the image potential becomes[43]:

$$V_{im}(x) = \frac{q^2}{16\pi\epsilon_I}\sum_{n=0}^{\infty}(k_1k_2)^n\Big(\frac{k_1}{nX_I + x} + \frac{k_2}{X_I(n+1) - x} + \frac{2k_1k_2}{X_I(n+1)}\Big) \quad (3.33)$$

with

$$k_1 = \frac{\epsilon_I - \epsilon_M}{\epsilon_I + \epsilon_M} \approx -1, \text{ and } k_2 = \frac{\epsilon_I - \epsilon_S}{\epsilon_I + \epsilon_S} \quad (3.34)$$

where ϵ_I, ϵ_S, and ϵ_M are the permittivities of the insulator, semiconductor, and metal layer respectively.

The full potential barrier become a superposition of the image potential and the potential barrier of the insulator. In Fig. 3.8 the potential barrier for a 40 Å thick SiO_2 barrier under 4 V voltage is modeled and the lowering effect of the image charges can be inspected.

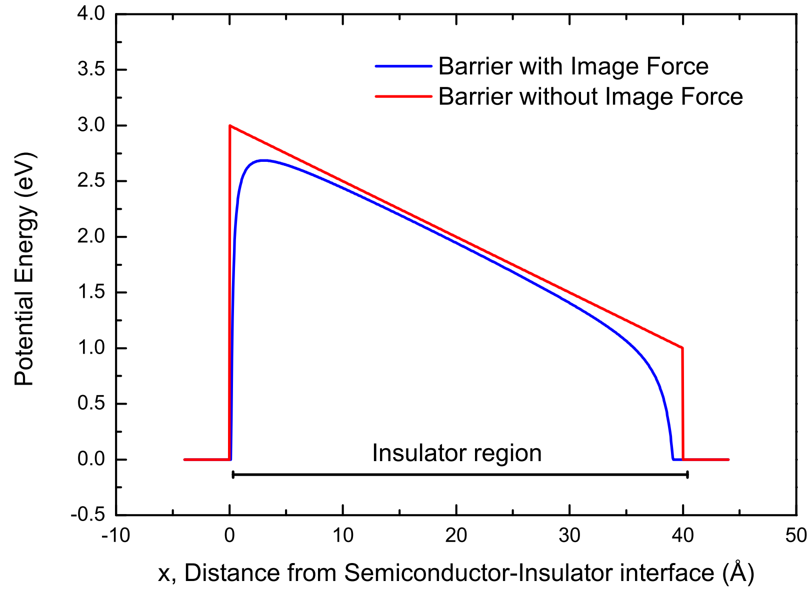

Figure 3.8: The potential barrier of 40 Å thick SiO_2 with and without the image potential taken into account. It is seen that the potential from the image charges significantly lowers the potential barrier.

3.3.5 The Supply Function

As stated earlier in this section the supply function yield the amount of electrons impinging on the tunnel barrier per unit time at a given energy. The supply function is given by the Fermi-Dirac distribution:

$$N(E_x) = \int_0^\infty f(E) dE_p \tag{3.35}$$

where E_p is the longitudinal and E_x is the transversal part of the energy. The integral can be solved by writing the total energy E as the sum $E_x + E_p$:

$$\begin{aligned} N(E_x) &= \int_0^\infty \frac{1}{1+\exp(\frac{E-E_F}{k_B T})} dE_p && (3.36) \\ &= \int_0^\infty \frac{1}{1+\exp(\frac{E_p+E_x-E_F}{k_B T})} dE_p && (3.37) \\ &= k_B T \ln\left(1+\exp(-\frac{E_x-E_F}{k_B T})\right) && (3.38) \end{aligned}$$

In Fig. 3.9 the supply function multiplied by the prefactor of the integral in Eq. 3.23 is shown for several positions of the Fermi level in the semiconductor.

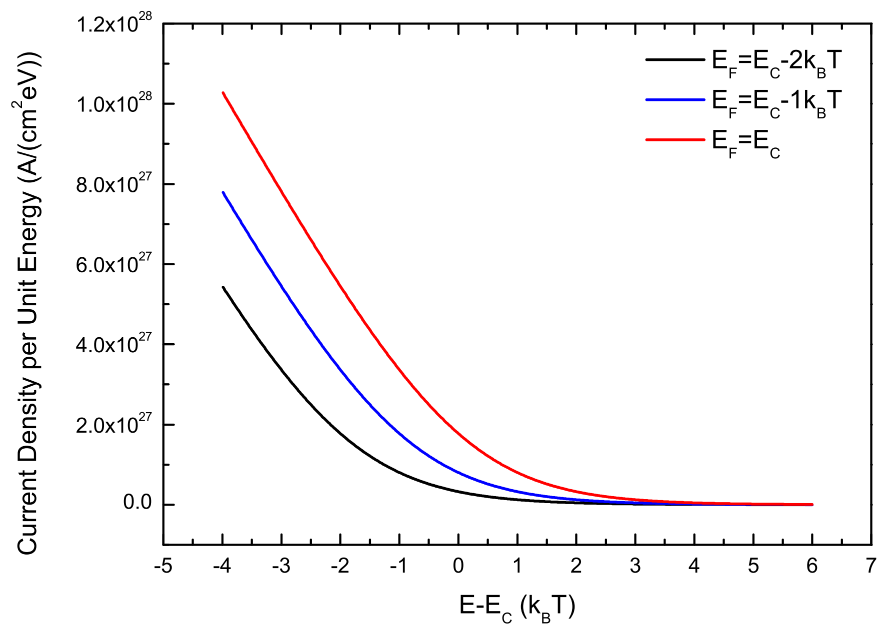

Figure 3.9: The supply function calculated for different values of the Fermi level. Due to the bandgap of the semiconductor the supply function is zero below the conduction band edge.

3.3.6 Energy Distribution of Tunneling Electrons

After having modeled the transmission and supply function separately we can now combine both to form the tunnel current energy distribution and the current voltage characteristics. The expected energy distribution of tunneling electron are simply the transmission function multiplied by the supply function and an example is shown in Fig. 3.10. The energy distribution is shown relative to the Fermi level of the metal layer. The energy distribution is almost invariable with bias voltage since the transmission coefficient is much lower than 1 for the electron energies accessible by the Fermi-Dirac distribution.

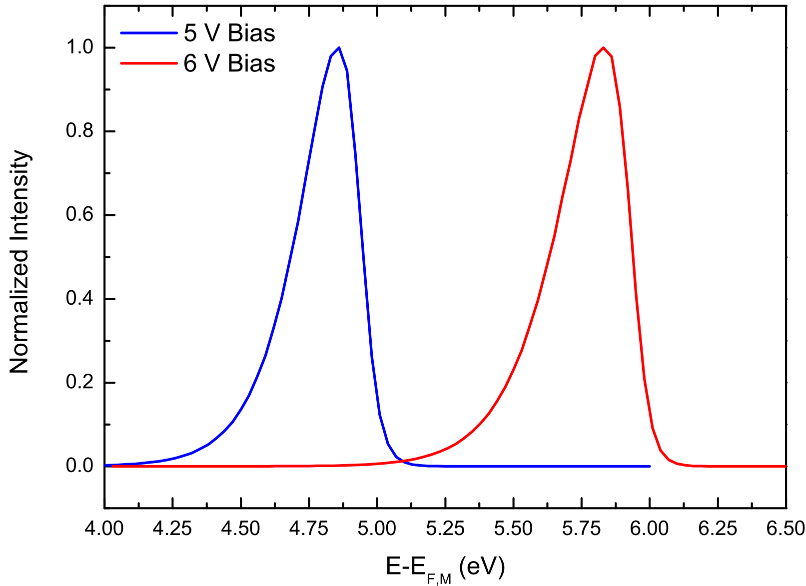

Figure 3.10: The energy distribution of electrons tunneling into an Au layer through a 50 Å thick SiO_2 layer on top of n-Si relative to the Fermi level in Au. The MIS structure is under 5 V and 6 V forward bias voltage. The distribution of electrons in energy is very narrow with a Fermi-like tail extending to higher energies from the supply function and with a tail to lower energies due to the surface potential.

3.3.7 IV Characteristics

By integrating the energy distribution for a given voltage the current density can be obtained. Repeating this for several voltages gives the IV characteristics as seen in Fig. 3.11 for various thicknesses of the insulator. In order to compare the IV characteristics to measured data the surface potential and the flat band voltage are calculated as a function of gate bias voltage using the model developed in sec. 3.2. Furthermore the surface potential is taken into account when evaluating the potential barrier of the insulator. The surface potential must be subtracted from the barrier height, since the distance from the Fermi level of the semiconductor to the conduction band of the insulator is reduced by an amount equal to the surface potential. The IV characteristics in Fig. 3.11 has been calculated using Au as the metal with a workfunction of (Φ_{Au}=4.8 eV), a donor concentration in Si of $N_D = 10^{19}$ cm^{-3}, and an effective mass of the tunneling electrons $m_I^* = 0.3$ m$_0$.

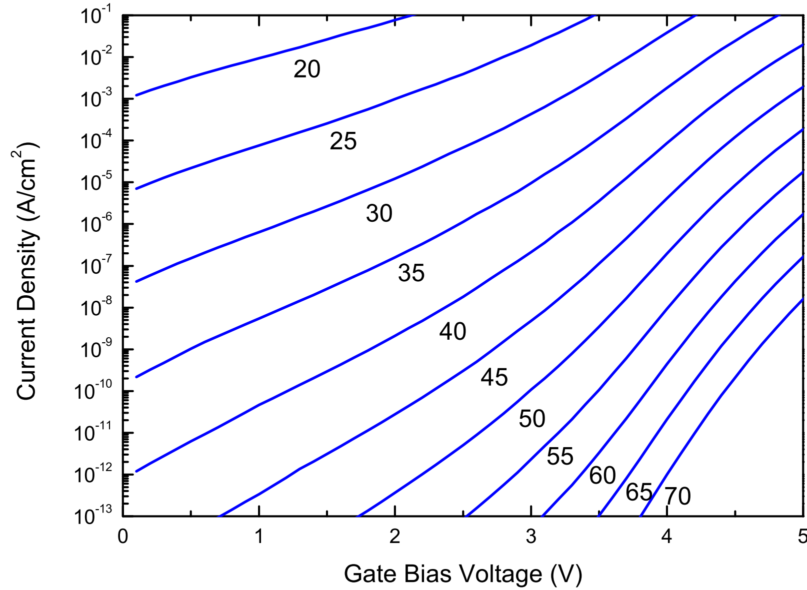

Figure 3.11: IV characteristics calculated using the model for various thicknesses of SiO_2. Thickness of the insulator in Å is marked to the right of each curve.

Now the full model for the IV characteristics is in place the influence of the different parts of the model on the IV characteristics can be tested. In Fig. 3.12 the modeled IV characteristics of a MIS structure with a 40 Å

thick SiO_2 layer is shown. In the case where the image potential have been left out of the model the tunneling current density is lowered by a factor of approximately 5, due to the larger barrier. Leaving out the correction for the surface potential parallel shift the curve to lower voltages due to the lack of flat band voltage and surface potential. Finally increasing the effective mass of the tunneling electron from 0.3 to 0.5 of the free electron mass dramatically lowers the current density due to the lower transmission probability for electrons with higher effective masses. The effective mass of the tunneling electron have been widely discussed in the literature[44, 45] and values between 0.19 and 0.6 times the free electron mass have been used. In this model a value of 0.3 have been used.

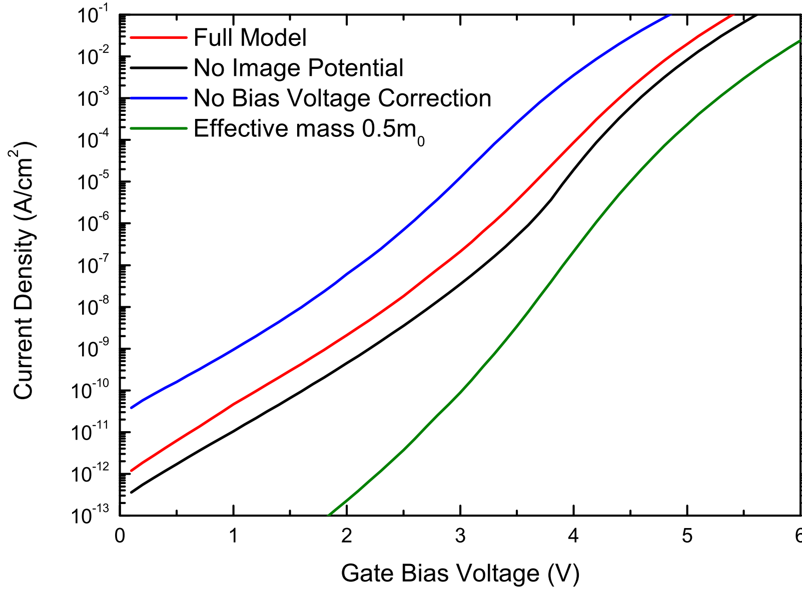

Figure 3.12: A comparison of IV characteristics calculated using the model. The full model (red) refer to the IV model taking the image potential into account, correcting for the surface potential, and with an effective electron mass in the insulator of 0.3 of the free electron mass. The black curve is calculated using the same setup, but with the image charge potential left out. The blue line is the IV without correction for the surface potential. The green line is the full model with an insulator effective electron mass of 0.5 of the free electron mass.

3.4 Self-Consistent Solution to Poisson's Equation

Another way to deal with the electrostatic problem of the MIS structure is to solve Poisson's equation, Eq. 3.11, self-consistently using a numerical solver. For more details on the implementation of the numerical problem see Appendix C. Poisson's equation can be discretized using a three point difference scheme as[46]:

$$R_i\psi_{i-1} - (1+R_i)\psi_i + \frac{\rho_i(\psi_i)}{\epsilon_i} h_i^2 R_i \frac{(1+R_i)}{2} + \psi_{i+1} = 0 \tag{3.39}$$

where ψ_i is the potential in the ith element, h_i is the width of the ith grid element and $R_i = h_{i+1}/h_i$. Eq. 3.39 is solved iteratively using a guessed potential distribution to calculate a charge density distribution, which is then used to obtain a new potential distribution. This process is then iterated until a self-consistent solution is obtained.

The charge distribution can be obtained using Eq. 3.2. Near the insulator-semiconductor interface the band bending of the conduction and valence bands are creating quantum wells with bound electronic states. This effect was neglected in the previous section about the MIS capacitor and the band bending region was implicitly treated as a continuation of the conduction band. In this numerical model the band bending region is treated as a quantum well and the stationary Schrödinger equation[40, 41, 42] is solved to yield the eigenenergies and eigenstates of the well.

The Schrödinger equation is discretized using the same three point difference scheme as used for Poisson's equation[46]:

$$-\frac{\hbar^2}{2m_t^*} \frac{\left[R_i v_{k,i-1} - (1+R_i) v_{k,i} + v_{k,i+1}\right]}{(h_i^2 R_i (1+R_i)/2)} + V_i v_{k,i} = E_k v_{k,i} \tag{3.40}$$

where V_i is the energy potential of the ith grid element. v_k is the eigenvector of the kth energy level with the corresponding energy E_k. m_t^* is the transversal electron mass for electrons moving specularly to the <100> direction in Si with a value of 0.1905 m_0[47].

The discretized Schrödinger equation is solved using a numerical eigenvalue problem solver to obtain eigenvalues and corresponding eigenvectors. The charge distribution from electrons in the bound states in the band bending region is obtained by calculating the probability distribution from each bound energy level (negative eigenvalue) as the corresponding eigenvector squared:

$$P_i(E_k) = |v_{k,i}|^2 \tag{3.41}$$

The contribution to the electron density distribution from the band bending quantum well is given as:

$$n_i = \frac{2m_c^*}{\pi\hbar^2} \sum_k k_B T \ln\left[1 + \exp((E - E_F)/k_B T)\right] |v_{k,i}|^2 \tag{3.42}$$

where m_c^* is the density of states effective mass for the conduction band of Si with a value of 1.08 m_0[47].

The hole contribution for negative surface potentials is calculated analogous to the electron concentration using appropriate effective masses for the holes. The concentrations of ionized donors and free electrons in the conduction band are calculated from equations 3.8 and 3.5, respectively.

An example of a self-consistent solution to the combination of the Poisson's and Schrödinger equations can be seen in Fig. 3.13. The example shows a MIS structure, with a 5 nm SiO_2 layer, in accumulation with an applied bias voltage of 4 eV. It is evident that the band bending gives rise to a quantized energy level at the semiconductor-insulator interface. In Fig. 3.14 another example of a self-consistent solution to Poisson's equation can be inspected. This solution is for a negative bias voltage of -3.5 V. Here the solutions to the Schrödinger equation are energy levels filled by holes. Due to the large surface potential, a quantum well is created in the valence band extending above the Fermi level and is filled by holes. The semiconductor is in inversion in this case.

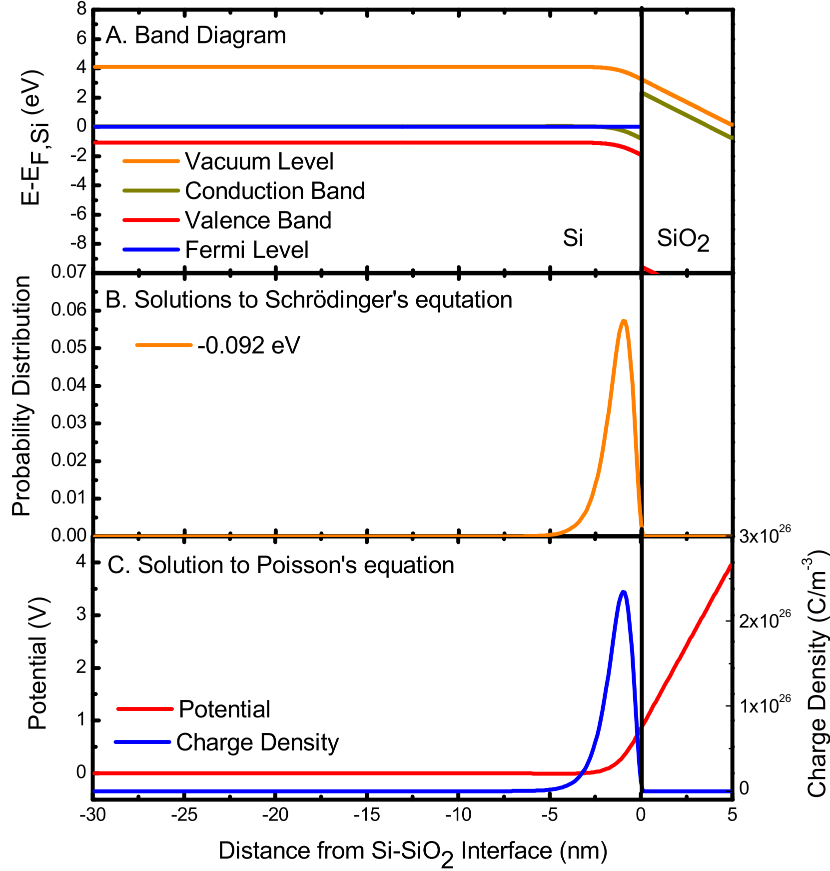

Figure 3.13: A self-consistent solution to Poisson's equation using the Schrödinger equation to obtain the energy levels and wavefunctions of the quantum well for a bias voltage of 4 V. **A. Band Diagram** Band diagram of the Si-SiO_2 part of the MIS structure. **B. Schrödinger solution** Probability distribution of the bound state of the quantum well of the conduction band of Si near the SiO_2 interface. The level energy quoted in the legend is relative to the conduction band edge of Si in the bulk. This state resembles the lowest state obtained from the analysis of a triangular quantum well[33]. **C. Solution to Poisson's equation** The solution to Poisson's equation. The charge carrier concentration is dominated by the electrons in the lowest bound state of the quantum well. This solution is obtained with a donor concentration of 10^{19} cm^{-3} and a bias voltage of 4 V.

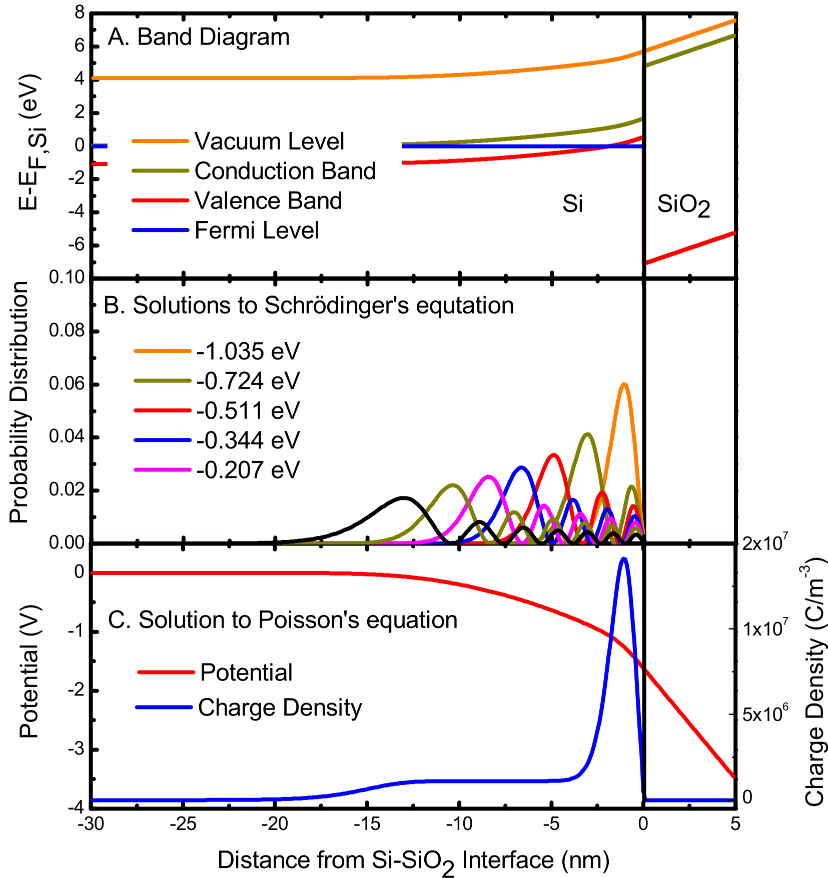

Figure 3.14: **A. Band Diagram** Band diagram of the Si-SiO_2 part of the MIS structure. A quantum well for holes is set up by the valence band bending upwards above the Fermi level of the semiconductor. **B. Schrödinger solution** The quantum well have seven bound energy levels. The level energies for the five lowest states, quoted in the legend is relative to the valence band edge of the bulk of Si. **C. Solution to Poisson's equation** The solution to Poisson's equation for a bias voltage of -3.5 V. The charge carrier concentration at the interface, is dominated by holes in the lowest bound state. Further from the interface the charge carriers are ionized donor atoms. The electrons are repelled from the depletion region which in this case is 15 nm wide. Due to the cost of potential to pull the valence band above the Fermi level and thereby create room for holes, the potential is extending far into the semiconductor, creating a large surface potential of -1.5 V.

3.4.1 CV characteristics from Self-Consistent Solutions

By obtaining the self-consistent solutions above for a range of bias voltages the results can be used to obtain the CV characteristics using the framework presented in Sec. 3.2.1. An example of a CV-curve from a series of self-consistent solutions to Poisson's equation can be seen in Fig. 3.15 along with a curve calculated using the continuous band theory from Sec. 3.2.1 and the experimental low-frequency CV characteristics obtained on a MIS hot electron emitter.

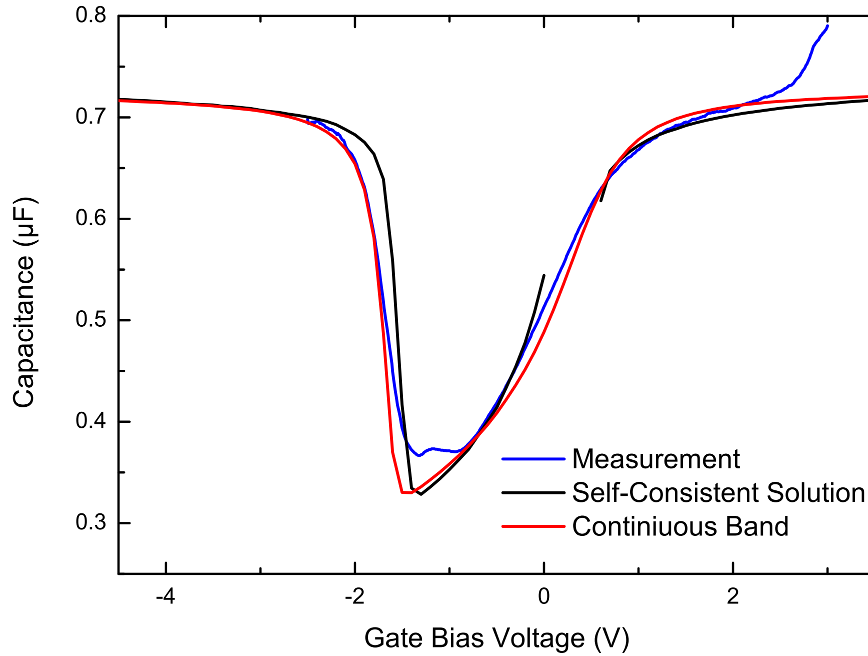

Figure 3.15: Comparison of a low frequency CV measurement on a MIS structure with a self-consistent solution and the continuous band model. The Continuous band model yield a thickness of 46 Å while the self-consistent solution yield 45 Å. A flat band voltage of 0.4 V and a donor concentration of 5×10^{18} cm^{-3} is used for both models. There is not much difference between the two models, which consolidates the validity of the continuous band model for these devices and oxide thicknesses.

The CV-characteristics from the self-consistent solutions are not defined close to 0 V surface potential since there is a difference in the differential quotient between the amount of free electrons being repelled from the in-

terface with respect to the surface potential and the amount of electrons generated in the bound states. From Fig. 3.15 it is seen that there is not much difference between the continuous band model and the self-consistent solution including the Schrödinger equation. Furthermore the self-consistent model is very computationally demanding and is not feasible to apply for data fitting. Therefore the continuous band model is applied in the rest of this thesis for fitting CV characteristics and extraction of parameters. However, the self-consistent solutions do yield a better qualitative understanding of the physics behind the CV characteristics of the MIS structure.

3.4.2 IV characteristics from Self-Consistent Solutions

As with the CV characteristics the IV characteristics can be calculated based on the self-consistent solutions. The supply function for the bound states are calculated as [48]:

$$N(E_k) = \frac{2m_c^*}{\pi\hbar^2} k_B T \ln\left[1 + \exp((E_k - E_F)/k_B T)\right]/\tau_k \qquad (3.43)$$

where

$$\tau_k = 2\int_0^{x_C} \sqrt{\frac{2E_k}{m_t^*}} dx \qquad (3.44)$$

where x_C is the classical turning point of the band bending quantum well. The supply function is then multiplied by the WKB transmission function from Eq. 3.27 and the contribution from each bound state is summed to yield the tunnel current. This approach however grossly overestimates the tunnel current by several orders of magnitude. This is probably due to the bound states of the quantum well being emptied by tunneling of electrons faster than electrons from the conduction band are scattered into these states. In this way the states in the band bending quantum well is out of equilibrium. It is beyond the scope of this thesis to calculate the scattering rate of electrons into the bound states which is needed to calculate the true contribution to the tunnel current from the bound states.

Chapter 4

Fabrication

The results presented in this thesis have been obtained on devices fabricated exclusively in the Danchip clean room facility situated on the campus of the Technical University of Denmark.

This chapter will present the process of fabrication the MIS hot electron emitters. A short overview of the process is given and then followed by a more technically elaborate step-by-step review of the process sequence.

4.1 Implementation of the MIS Hot Electron Emitter

The MIS hot electron emitter is a MIS structure implemented with a Si substrate, a SiO_2 and a thin metal layer as the gate. To ensure stability against mechanical probing the device is framed with a thick oxide region. A view of the hot electron emitter and the different layers can be seen in Fig. 4.1 and 4.2. Below the different layers and their purpose are explained in detail.

The hot electron emitters are designed with a 1 cm^2 active area of ultra-thin SiO_2. The devices measure 16×14 mm including the thick oxide frame. The hot electron emitters are fabricated on 4 inch (100 mm) wafers, with 20 individual chips on each wafer. Each chip is separated with a 0.3 mm gap which is used when separating the wafer into individual chips. Fig. 4.3 show an example of a wafer with 20 hot electron emitters. It is also possible to fabricate wafers which, apart from the 20 full size devices, have a large amount of test devices with areas of thin tunnel oxide a fraction of the full size devices.

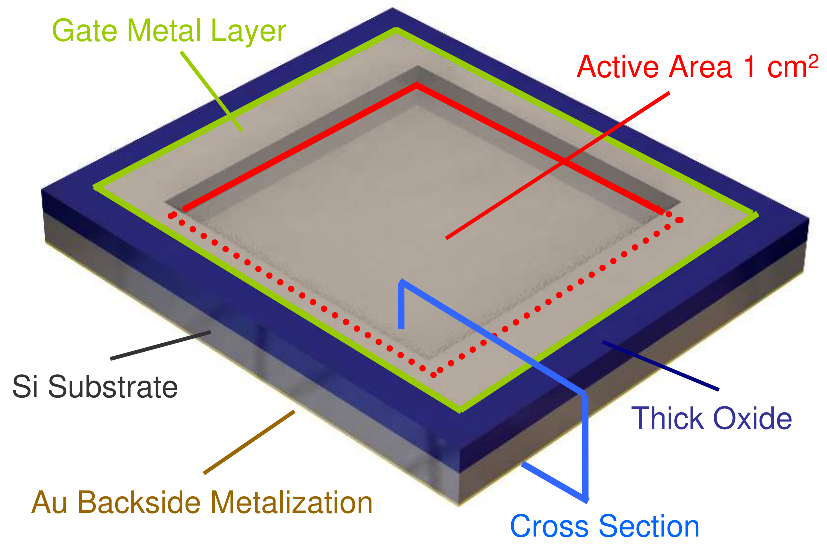

Figure 4.1: View of the MIS hot electron emitter. The active area, marked with red, is the area with thin tunnel oxide, where electrons tunnel through and are injected as hot electrons in the metal layer. The metal layer extends beyond the active area to make mechanical contacting on the thick oxide possible. The cross section marked with blue is shown in Fig. 4.2.

Substrate

The substrates used for the Hot Electron emitters produced in this project are 4" Si wafers highly n-doped using antimony (Sb). The sheet resistance stated for these wafers by the manufacturer (Okmetic, Finland) is $\leq 0.025\,\Omega$ cm. The crystal orientation of the wafers are <100> to expose a rectangular lattice as the surface, which is useful when cleaving the wafers into single devices. The Si substrate is chosen due to the availability of very well-defined and relatively cheap wafers of Si. The wafers used in this project is highly n-doped in order to ensure easily obtainable ohmic contact to the interfacing instrumentation and negligible voltage drop across the substrate itself, which makes it easy to obtain the voltage burden across the tunnel barrier formed on the substrate.

Tunnel Barrier

The tunnel barrier of the Hot Electron Emitter is an ultra-thin layer of thermally grown SiO_2 with an area of 1 cm^2. The oxide is formed in an ultra-clean furnace immediately after an RCA[49] cleaning procedure. The area of 1 cm^2 is ultra-large compared to similar devices produced in the semiconductor industry which typically have active areas several thousands times smaller than

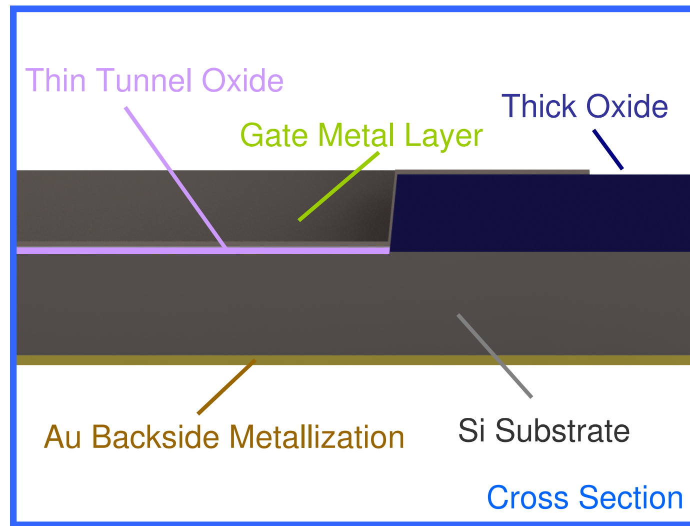

Figure 4.2: Cross section view of a MIS hot electron emitter as marked in Fig. 4.1. From below is seen: The backside metallization of 10 nm Ti and 100 nm Au to provide low resistance ohmic contact to the Si substrate. On the top of the Si substrate to the right is the thick oxide used as a mechanical barrier to allow probing and handling of the device. On top of the Si substrate to the left is the thin tunnel oxide through which electrons can tunnel between the Si substrate and the metal layer. The topmost layer is the thin metal layer which works as a gate to bias the tunnel oxide with respect to the substrate, and as the template for hot electron chemistry.

1 cm^2. The area is chosen to meet the ultimate objective of the project of detecting hot electron enhanced chemistry on the device. The probability of detecting hot electron chemistry is directly proportional to the active area of the devices. 1 cm^2 is a compromise between optimizing detection probability of hot electron chemistry events and being able to form devices with a high probability of success. The thickness of the oxide must be in the low nanometer range in order to get a reasonable tunnel current density. The oxide thickness can be customized to a given application and should represent the optimum between the energy of the hot electrons (given by the applied voltage) needed and maximizing the current density. In general the oxide thickness should be tailored to be able to support the field created by the applied voltage, but otherwise as thin as possible to maximize tunnel probability and thereby current density of hot electrons in the device.

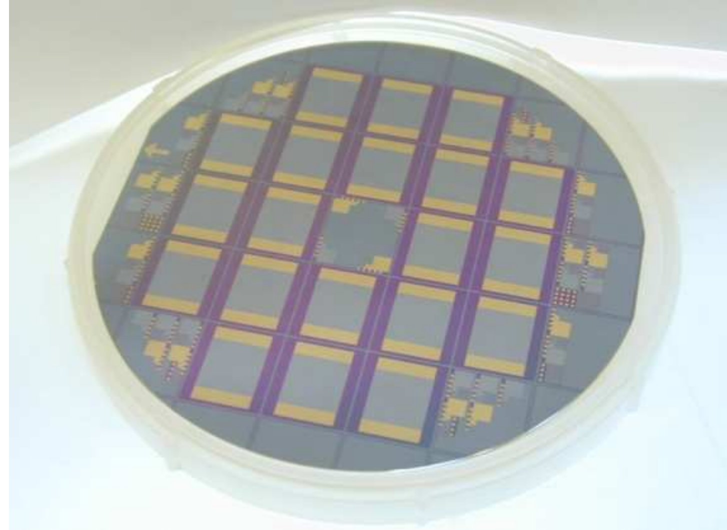

Figure 4.3: Photograph showing a wafer with 20 full size hot electron emitters and many smaller test devices. The test devices are situated along the perimeter of the wafer and in the center. On this wafer a thick gold layer has been deposited on a part of the thick oxide frame. This layer has been omitted in the following process sequence, since it was not used very often.

Metal Gate Layer

The purposes of the metal gate layer are multiple; first of all it serves to apply the bias voltage across the tunnel barrier, secondly it serves, along with the backside, as the electrical contact to interfacing instruments, and finally it is the template for hot electron surface chemistry. From the purposes as electrical contacts and applying a bias voltage a thick well-conducting metal layer would be beneficial, but from the application of the devices as hot electron emitters the metal layer should be kept as thin as possible in order to avoid scattering and thermalization of the hot electrons in the metal layer. The metal layer of the devices fabricated in this project have all been deposited using PVD. First off we used a photo resist mask and subsequent lift-off to define the metal layer, but this resulted in dirty metal films. An Al shadow mask was designed to eliminate the need for wet chemistry after the metal layer had been deposited and this resulted in significantly cleaner metal films.

Thick Oxide Frame

The purpose of the thick SiO_2 layer is to allow for mechanical contacts to electrically interface with the metal gate layer. Electrical contact can be

made to thick metal films, on the order of 100 nm or so, directly on the ultra thin oxide region, but with thin gate layers of 20 nm and below the ultra-thin oxide is ruined if probed mechanically. The thick oxide frame is created in two steps; first a 0.75 μm thick wet oxide is formed in a furnace, this oxide is then etched away to reveal the Si substrate in the active emitter areas using a bHF solution.

4.1.1 Process Overview

The process sequence for the Hot Electron Emitters was originally designed by Ole Hansen, but have undergone a number of smaller revisions to the state presented here.

A thick wet oxide is formed on the substrates. The thick wet oxide is etched back to the substrate in the active areas. The substrates are cleaned using a standard RCA clean. Immediately after the cleaning process a dry oxide is formed in an ultra-clean furnace. An ohmic back contact is deposited by PVD. As the final step the metal gate layer is deposited through a shadow mask by PVD. If required the wafers are cleaved into single devices. Fig. 4.4 show the different steps in the process sequence.

4.2 Process Sequence

Below is given a step-by-step process sequence for the Hot Electron Emitters. Focus have been placed on explaining the process in general terms applicable in any cleanroom facility with comments included to highlight procedures where special care should be taken. For a list of equipment and specific details of the implementation used in the Danchip clean room facility please refer to Appendix D.

1 Wafer Selection 4 inch <100> silicon (Si) wafers highly n-doped with antimony (Sb). One side polished, which is the side being processed below if nothing else is stated explicitly. Sheet resistance $\leq$0.025 Ω cm.

2 Formation of Thick Oxide Wet thermal oxidation of wafers in furnace at 1000°C for 180 min. in 1 bar H_2O. SiO_2 target thickness 750 nm. Film thickness characterized using an ellipsometer.
The oxide film thickness achieved is not critical, but must be determined to approximate the etch time in step 4. The thickness variation is approximately 5% from the first to the last of 25 wafers in the furnace process.

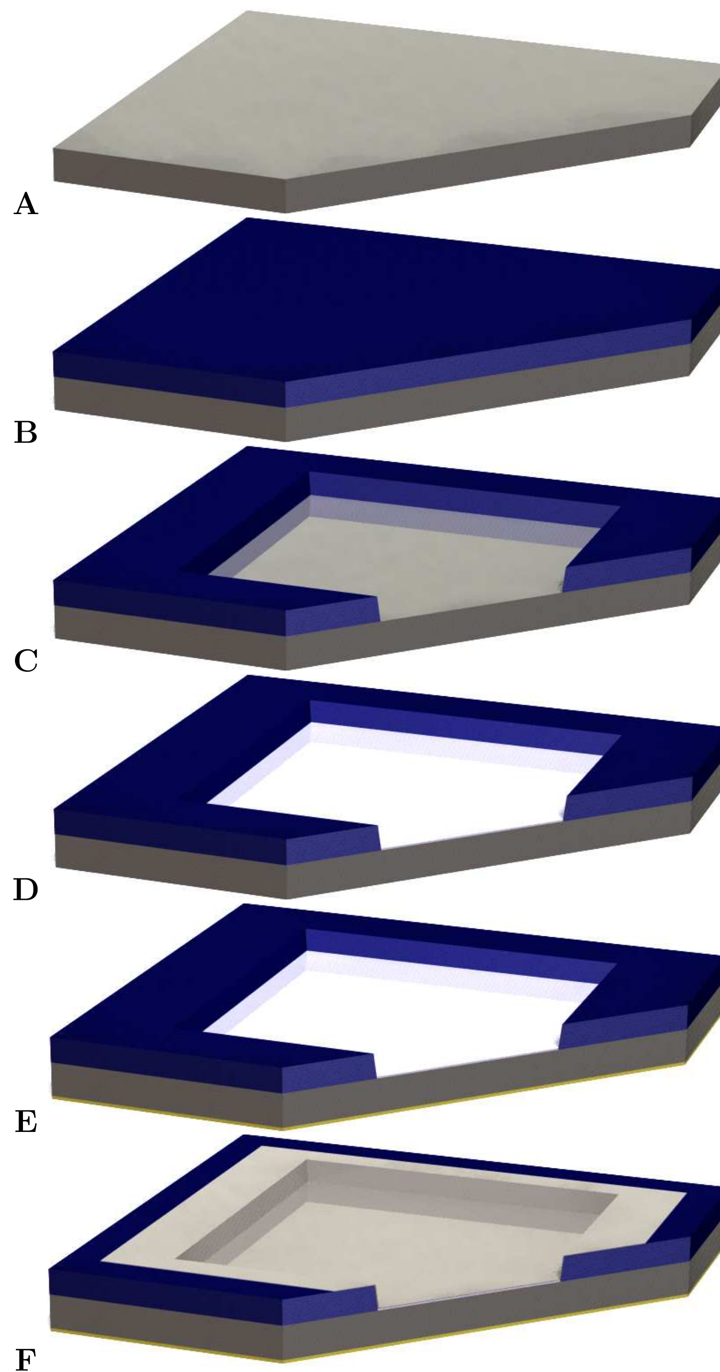

Figure 4.4: Graphical overview of the process sequence. The numbers in parentheses refer to the step number in the detailed process sequence. **A:** (1) Plain wafer. **B:** (2) Thick oxide formation. **C:** (4) Back etching of thick oxide to substrate. **D:** (5) Formation of thin tunnel oxide. **E:** (6) Backside metallization. **F:** (7) Gate metal deposition.

3 Etch Mask Definition Etch mask of 1.5 μm AZ resist is applied to the wafers. Prebake at 90°C for 90 s. UV exposure 10 s with hard contact through a positive mask defining the active areas of the emitters. Development in NaOH for 60 s and rinsed in de-ionized (DI) water, then spin dried. Hard baked at 120°C for 60 s.

4 Back Etching of Active Emitter Areas Wafers etched in 5% buffered hydrofluoric acid (bHF) for 9 min. The etching rate is approx. 80 nm min^{-1}. After the first 9 min. the wafers are visually inspected for hydrophobicity in the active emitter areas each 15 s until such is obtained and the etching is stopped. The wafers are rinsed in DI water. The etch mask resist is stripped in a sonicated acetone bath for 15 min. Rinsed in DI water and spin dried.
The important point in this step is to make sure all of the low quality wet oxide formed in step 2 is removed without over etching which would induce further surface roughness at the Si interface. We visually inspect the wafer with the thinnest oxide formed in step 2 for hydrophobicity in the active emitter areas and rely on the HF dips in the RCA clean in step 5 to remove the last few tenth of nanometers of oxide left on the rest of the wafers.

5 Tunnel Oxide Formation Standard RCA [49] clean with hydrofluoric (HF) acid dips included. Dry thermal oxidation of wafers in ultra-clean furnace at 800°C for 40 min. in 1 bar O_2 with following post anneal in 1 bar N_2 for 20 min. SiO_2 target thickness 50 Å. Film thickness characterized using an ellipsometer.
The RCA clean must be performed immediately prior to oxide formation to avoid native oxide formation and maximize cleanliness. After oxide formation and post anneal the wafers should be removed from the furnace immediately to avoid further oxide formation. The oxide thickness vary monotonically with position in the furnace with approximately 1 nm over 25 wafers.

6 Wafer Backside Metallization SiO_2 film on backside stripped using 5% hydrofluoric acid (HF). Ti/Au layer for ohmic contact to Si substrate deposited using Physical Vapor Deposition (PVD). Film 10 nm Ti + 100 nm Au by Quartz Crystal Microbalance (QCM).

7 Gate Metal Deposition Deposited by PVD through Al shadow mask. For electrical characterization a 10 nm Ti + 100 nm Au is deposited. Otherwise the metal type and thickness is chosen for the specific purpose.

8 Optionally: Wafer Dicing Wafers are scribed using a diamond scriber tool along crystal directions and cleaved into individual chips/devices. *When cleaving the wafer it is important not to place the wafer with the polished side facing down, this will ruin the tunnel oxide. Instead each individual score line is aligned to a sharp edge and the wafer is cleaved by applying pressure vertically downwards on the part extending out from the edge.*

Chapter 5

Ultra High Vacuum Setup

Experiments in this thesis which requires Ultra High Vacuum (UHV) have been performed in the UHV setup described in this section. These experiments were the electron emission experiments in chapter 7, the electron energy dispersion measurements presented in chapter 8, and the experiments towards hot electron chemistry presented in chapter 9.

The UHV setup consists of a main chamber made of stainless steel into which different equipment is fixed through various ports. For an overview of the chamber refer to Fig. 5.1. The chamber is pumped using a turbo molecular pump as the main pump, and an ion pump, a small turbo pump, and a Ti sublimation pump as auxiliary pumps. The ion pump is pumping the x-ray gun, while the small turbo is pumping on the mass spectrometer and the garage. The sublimation pump is used after heavy gas exposures to bring down the pressure of the main chamber overnight. A base pressure below 10^{-9} mbar is achieved routinely.

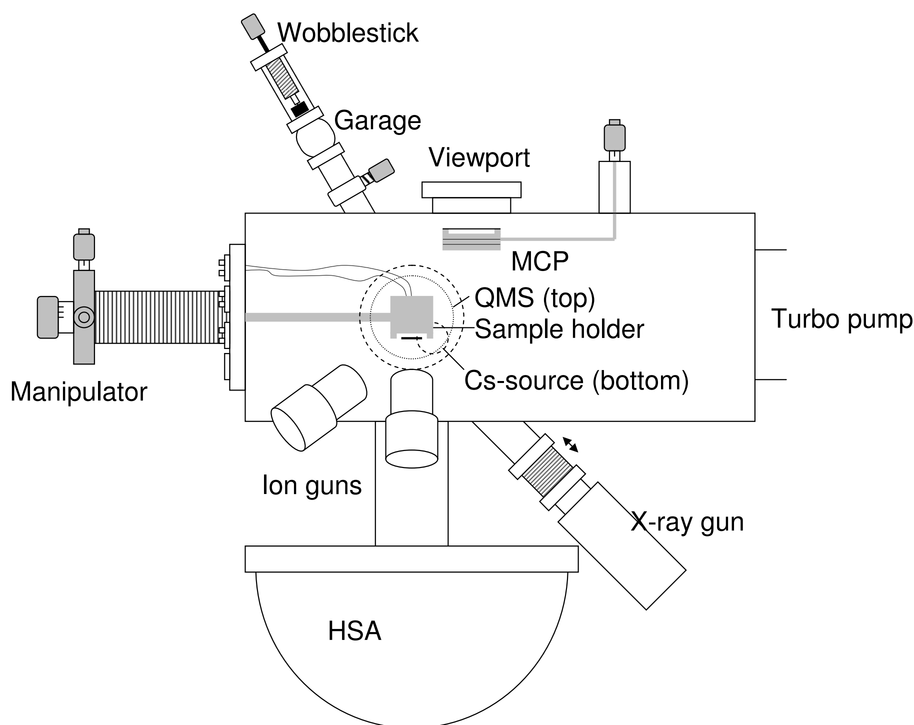

Figure 5.1: Schematic view of the UHV setup.

Before entering the chamber the sample (MIS hot electron emitter) is fixed on a stainless steel frame, see Fig. 5.2. It is fixed using two molybdenum clips with six quartz glass plates as spacers to isolate the device and Mo clips from the steel frame itself. The Mo clips doubles as front side contacts to the hot electron emitter. The steel frame has a hole in the middle to allow indirect heating of the hot electron emitter. Furthermore backside and thermocouple contacts are made through this hole. The circular hole on the end of the steel frame is for the wobble stick to grab on to.

The samples are placed in the garage outside the main chamber, which can be vented and evacuated separately by a small turbo pump. The garage accommodates 16 samples. From the garage the samples can be picked up by a wobblestick and moved into the main chamber.

The main piece of equipment in the chamber is the manipulator which is a retractable and rotatable arm on which the sample holder is fixed. The sample holder accommodates one sample, fixed on the steel frame, at a time.

The sampler holder is a Cu house with a small elevator inside which can be activated using the wobblestick. The elevator retracts a heating filament (tungsten), a backside contact probe, two front contact probes, and a thermocouple probe before the sample is loaded. When a sample is loaded the

Figure 5.2: A MIS hot electron emitter fixed to the stainless steel frame. The two clips of Mo are clamping the device to the frame. Six glass plates act as spacers to isolate the device from the steel frame. In the sampleholder contacts are made to the backside through a hole in the frame. The Mo clips double as front contacts, which in the sampleholder are made from beneath to the clips.

elevator can be pushed back up, using the wobblestick, to make contacts to the sample. The sample sits 1 inch off-axis relative on the manipulator.

Using the manipulator the sample can be placed in front of the various instruments in the chamber. The equipment available is: X-ray gun and Hemispherical analyzer (HSA) for X-ray Photo-electron Spectroscopy (XPS), ion guns with Ar, O, and He for Ion Scattering Spectroscopy (ISS), mass spectrometer for gas analysis, getter source for evaporation of Cs, pressure gauge, Micro Channel Plate (MCP) for imaging purposes, a 3×3 cm Cu plate for measuring emission current, and a gas handling system with leak valves for dosing NO, CO, labeled CO, O_2, Ar, and He.

The mass spectrometer, a Balzers QMA125, is enclosed behind a Cu snout leading into the main chamber. The opening of the snout is 3 mm in diameter under which the sample is placed for desorption and reactivity experiments. The Cu snout prevents desorbed species from the chamber background from reaching the mass spectrometer.

The differentially pumped X-ray gun from VSW is a dual anode type with an Al and a Mg side. The dual polarity (ions and electrons) HSA from VSW is 100 mm in diameter with variable entry/exit slit sizes and a close ended channeltron for pulse counting measurements. A more thorough description of the HSA is available in chapter 8.

Chapter 6

Tunnel Barrier Thickness and Variations

The work presented in this chapter have been devoted to exploration of the tunnel barrier thickness and thickness variation. The experimental methods used to extract thickness and roughness information are IV- and CV characteristics as well as ellipsommetry. Each technique is based on different physical phenomena to extract information on the thickness. It is very important to characterize the tunnel barrier in order to obtain information on the thickness and variations in thickness across the MIS hot electron emitter structure.

In our hot electron emitter the tunnel barrier, as explained in Sec. 4.1, is a thermally grown SiO_2 layer. Due to differences in heat and oxygen flows across the wafers in the furnace, as well as variations in the donor concentration[50, 51], polishing, roughness and thickness variations can be introduced in the SiO_2 layer and some degree of roughness and thickness variations is to be expected. As made clear in Sec. 3.3 about electron tunneling through insulating layers, the current density is exponentially dependent on the thickness of the insulating oxide. The thickness directly determines the current density of hot electrons that are available in the metal layer for enhancing surface chemical reactions.

The reaction rate, as seen in Sec. 9.6, is furthermore very dependent on the voltage applied across the tunnel barrier, since the reaction probability of the molecular resonances for hot electrons is controlled by the electron energy which is given by the applied bias voltage. The current density must be optimized for bias voltages close to the relevant resonances, which can be done by tailoring the thickness of the tunnel barrier. Furthermore there is a limitation to how thin the oxide can be made in order for it to be able to withstand large bias voltages. The thickness of the tunnel barrier must

be optimized to deliver the highest possible current density at the desired resonance energy while avoiding failure of the tunnel barrier. In order for this optimization to succeed it is of paramount importance to be able to grow a tunnel barrier oxide with a very well-defined thickness.

Not only is control of the thickness of the tunnel barrier important for optimal operation of the hot electron emitter as a tool for enhancing surface chemistry, but so is also the roughness or thickness variations of the tunnel barrier. Since the tunneling current is exponentially dependent on the thickness of the barrier, areas of the hot electron emitter with relatively thinner tunnel barrier oxide thickness will become hot spots with extremely high current density compared to the areas with relatively thicker barrier. As with the thickness, the impact of tunnel barrier thickness variations will be two-fold and related to hot electron chemistry and failure of the tunnel barrier. In relation to hot electron chemistry it is obvious that the areas with a relative thick tunnel barrier will be completely inactive compared to the areas with a relative thin tunnel barrier. The device would then have to rely on the ability of adsorbed species to readily diffuse to the hot spots.

Due to the exponential dependence of the current density on the tunnel barrier thickness there can be orders of magnitude in difference between reaction rates at hot- and cold spots. Furthermore the failure probability of the tunnel barrier is dependent on the thickness. The tunnel barrier failure process is of a weakest link nature [52, 53] where the areas of thin tunnel barrier, statistically, will fail first and to a large extent render the whole device broken.

6.1 Roughness

In order to get a quantitative measure of the importance of keeping roughness to an absolute minimum this section will present a simulation illuminating some of the effects of tunnel barrier roughness. The different ways different experimental techniques averages the roughness and or gradients in the tunnel barrier thickness can be exploited to yield information on the roughness from microscopic to macroscopic length scales.

The first thing to be simulated is how the current in a large MIS electron emitter is distributed over the area as a function of the roughness of the tunnel barrier thickness. This is simulated by assembling an array of 10^4 elements each representing a small area of tunnel barrier with a certain thickness given by normal distributed random numbers. The normal distribution of tunnel barrier segments are characterized by a mean thickness and a standard deviation. The normal distribution is cut off at three times the

standard deviation away from the mean value. In Fig. 6.1 the cumulative current carried versus cumulative area is shown for four values of the standard deviation (σ) for a tunnel barrier with a mean thickness of 50 Å. The curve with $\sigma = 0$ correspond to no roughness, thus the current is evenly distributed across the entire area, which yield a straight line with a slope of 1. For increasing roughness the current is distributed towards the areas with thin tunnel barrier and most of the current is carried in a small part of the active area.

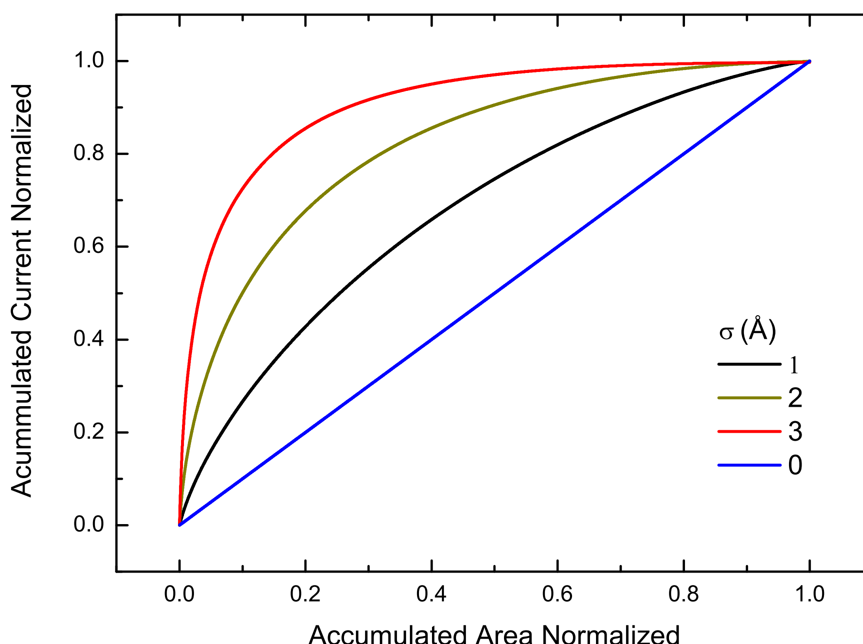

Figure 6.1: Accumulated current as a function of accumulated area for several values of the standard deviation of normal distributed tunnel barrier thicknesses around a mean thickness of 50 Å.

From Fig. 6.1 it is clearly seen how important the roughness is for the current distribution across the MIS emitter. For a σ of 3 Å 70 % of the current is carried in only 10 % of the emitter area!

As mentioned earlier roughness also influence the thickness extracted from various measurement techniques due to the different ways the techniques average over the area measured. Two electrical characterization tools used for extracting the tunnel barrier thickness is IV and CV characteristics. The IV characteristics is seing the transmission of electrons through the barrier

which is exponentially dependent on the thickness of the tunnel barrier, while CV is averaging more linearly due to the inverse relation of the capacitance to the thickness.

A good approximation to the tunneling current through the oxide in the Fowler Nordheim regime is given by Eq. 6.1[35, 54, 55]:

$$J_{\mathrm{FN}} = A\varepsilon_I^2 \exp(-\frac{B}{\varepsilon_I}) \tag{6.1}$$

where ε_I is the electric field in the oxide given by $\varepsilon_I = \frac{V_I}{X_I}$, A and B are constants given by:

$$A = \frac{q^3}{16\pi^2\hbar}\frac{m_S^*}{\Phi_B m_I^*} \text{ and } B = \frac{4}{3}\frac{\sqrt{2m_I^*}}{q\hbar}\Phi_B^{3/2} \tag{6.2}$$

From the constant B it is seen that the tunnel current is exponentially dependent on thickness. In the following the expression in Eq. 6.1 will be used to convert between current and tunnel barrier thickness. The following expression will be used to convert between capacitance and thickness:

$$C = \frac{\epsilon_r A}{X_I} \tag{6.3}$$

where ϵ_r is the permittivity of the insulator and A is the active area of the MIS emitter structure.

In order to investigate the difference in tunnel barrier thickness the two different techniques will yield for the same device, given a thickness variation the capacitance and current are calculated on each individual patch of tunnel barrier using Eq. 6.1 and 6.3. The contributions for each segment are then summed for the entire device and a thickness is then extracted for the entire device by solving Eq. 6.1 and 6.3 numerically.

In Fig. 6.2 it is shown how the thickness extracted from CV and IV characteristics will depend on the roughness of the oxide. As before the roughness is modeled by a normal distribution of roughness around a mean thickness of 50 Å, but here also for a uniform distribution and an extreme distribution. The uniform distribution is cut off at 3 σ. For the extreme distribution 5 % of the area of the tunnel barrier is 3 σ lower in thickness than the rest of the active area.

In the above the area of the tunnel barrier is implicitly infinitely larger than the characteristic length scale of the roughness. A way to get information on the length scale of the roughness would be to extract the tunnel barrier thickness on several tunnel barrier areas and compare them. When the side-length of the device becomes comparable to the characteristic length scale the extracted thickness will become statistically distributed.

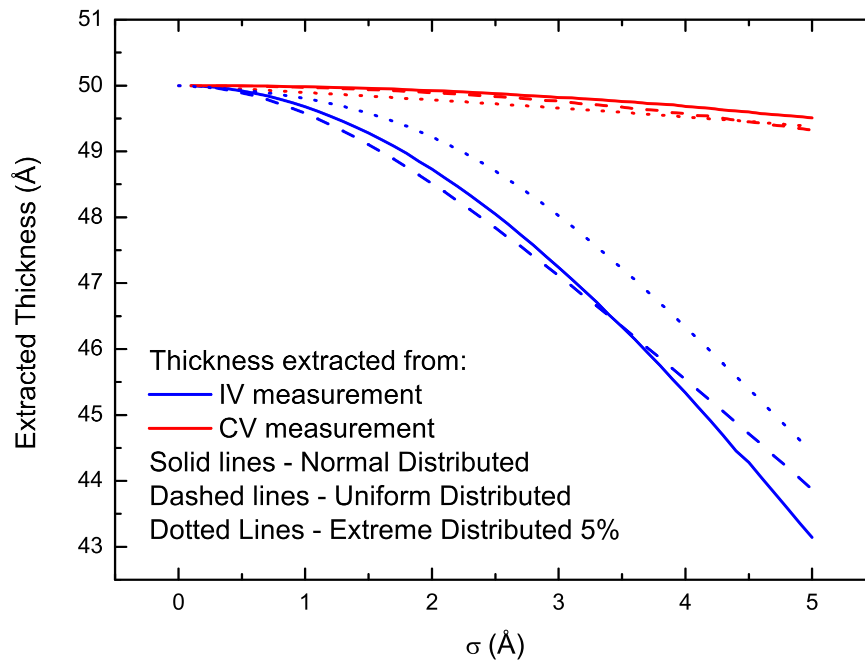

Figure 6.2: The thicknesses as extracted from simulated measurements of the IV and CV characteristics for three types of distributions of tunnel barrier roughness as a function of the σ of the roughness around a mean value of the thickness of 50 Å.

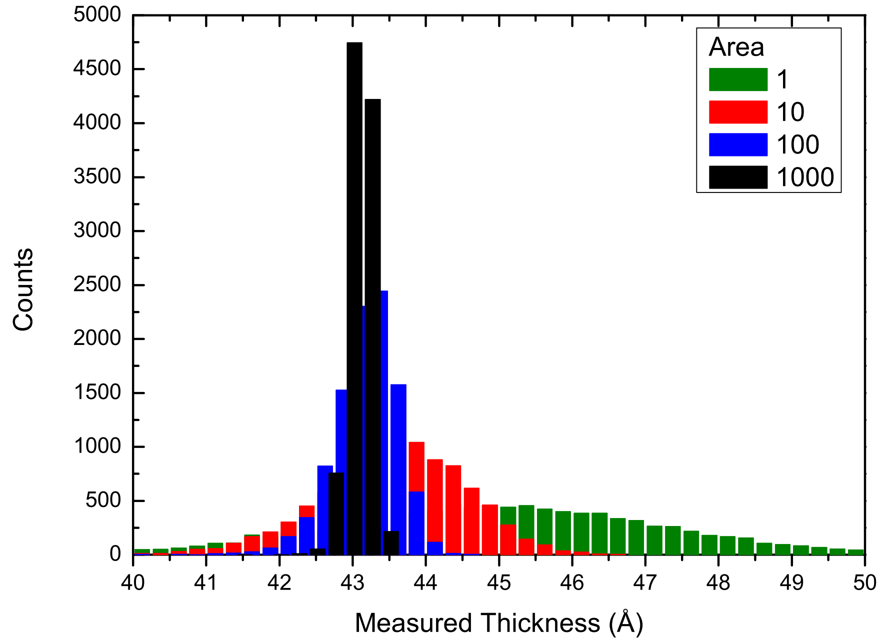

Figure 6.3: Distribution of tunnel barrier thicknesses extracted from simulated measurements on 10^4 devices with areas of 1, 10, 100, and 1000 segments. The thickness of the individual segments are normally distributed with a mean of 45 Å and a standard deviation of 3 Å. The more thickness segments a devices covers the more narrow the distribution of thicknesses extracted becomes.

In Fig. 6.3 the distributions of extracted thicknesses from simulated measurements on 10^4 devices with different tunnel barrier areas are shown. For an area equal to 1 the device contain one thickness element, while areas equal to 10 contains 10 elements and so on. The more elements the narrower the distribution becomes around the mean of the distribution weighed with respect to the tunnel current. In this way measurements on devices with a variety of areas can be used to characterize the length scales of the tunnel barrier roughness and thickness variation.

6.2 Experimental

With the preceding discussion of the importance of tunnel barrier thickness and roughness in mind an experimental investigation of the roughness has been conducted. First the experimental procedures and basic results will be presented followed by a discussion linking the results with the discussion in the previous section.

The results presented in this section were obtained on MIS hot electron emitter devices fabricated in the batch labeled as batch 11. The wafers in this batch were all from the same package of wafers and were batch processed all the way through fabrication to avoid errors from variation in process conditions.

The devices were produced using the process sequence described in Sec. 4.2 with 40 min. oxidation time to produce an approximately 5 nm thick tunnel oxide. The gate metal layer is 10 nm Ti and 100 nm Au, for low resistance and easy contacting.

The oxide thickness of each wafer was measured in the center of the wafer by ellipsommetry before metal deposition. The ellipsommetry measurements in general yield larger thicknesses of the tunnel oxide than the electrical measurements. It has previously been established that the ellipsommeter setup used yield 8 Å larger oxide thicknesses compared to Atomic Force Microscopy (AFM) measurements [56], which explains the offset compared to the electrical measurements observed here. The first electrical measurement performed on each device was CV characteristics, since there is less possibility of device breakdown due to the relative low bias voltages applied compared to IV measurements. After the CV characteristics was obtained the IV measurement was performed.

6.2.1 CV Measurements

The capacitances of the devices were, in this experiment, measured using a home-built analog integrator. The reason for using the home-built integrator was that we at the time did not have any other charge measuring instruments at our disposal and the capacitance of our devices is so large that most traditional instruments become unstable when connected to the devices.

The analog integrator, see Fig. 6.4, was equipped with seven reference capacitors from 4.7 pF to 47 μF to cover a wide range of inputs. Each of the reference capacitors was calibrated using a static capacitance meter. In order to circumvent tunnel or other leakage current from disturbing the capacitance measurement the capacitance was measured in the following way:

A signal of the form shown in Fig. 6.4 is applied to the MIS structure

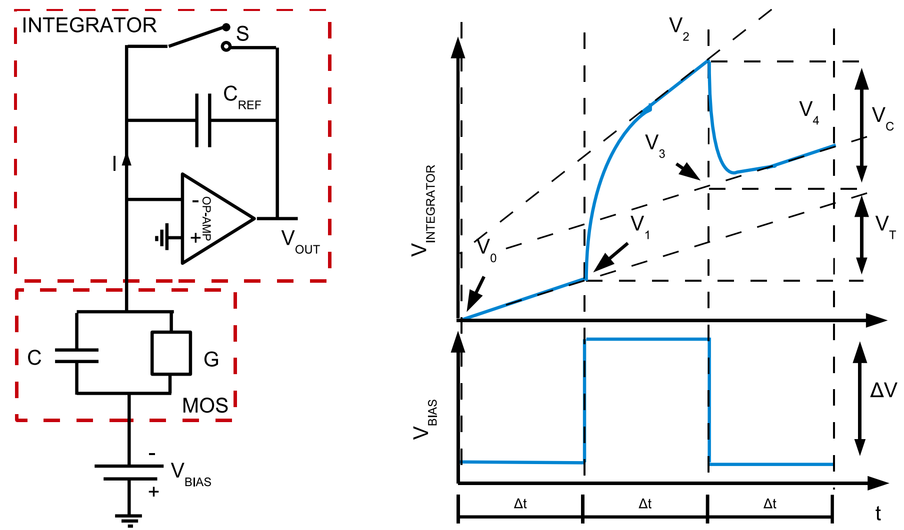

Figure 6.4: Left: The MIS structure and analog integrator setup. The charge flowing to and from the MIS structure (or MOS Metal Oxide Semiconductor) is stored on the reference capacitor and a voltage proportional to the stored charge is added at V_{OUT}. The switch S resets the integrator between two consecutive measurements. Right: The applied signal and an example of the corresponding integrator output. The signal V_{BIAS} is applied to the MIS structure. At first there is a steady current due to leakage current in the system, when the potential step is applied a charging of the MIS structure occurs which produces a sharp transient on the integrator followed by constant charging due to leakage currents at the applied voltage. When the applied potential steps down the MIS structure is discharged creating a transient discharging of the integrator followed by another constant charging from leakage current. In the text it is described how the capacitance of the MIS structure is extracted from the signal.

under test. The square voltage waveform is applied to the MIS structure to be able to correct for due to signals from leakage current not related to charging of the capacitance of the MIS structure under test. When the square signal is applied to the MIS structure the signal on the integrator steps up with an almost vertical flank due to the charging of the capacitance of the MIS structure. When the square voltage signal end the MIS capacitor is discharged again. Between changes in the square voltage signal the signal on the integrator is changing at a constant rate due to current flowing through the MIS structure and integrator system.

By measuring the voltages V_0, V_1, V_2, and V_4 the capacitance of the MIS structure can be obtained without influence of transient charges flowing in

the system since these voltages are measured as far after changes in the square voltage signal occurred as possible. To calculate the capacitance of the MIS structure the signal difference between V_2 and V_3 must be obtained, and since V_3 is not measured it must be determined from V_4 by assuming a constant leakage current through the measurement setup over Δt at the low voltage of the applied bias voltage. V_3 is obtained as $V_4 - (V_1 - V_0)$ and the capacitance of the MIS structure is obtained as:

$$C_{\mathrm{MIS}} = \frac{(V_2 - V_3) \cdot C_{\mathrm{REF}}}{\Delta V} = \frac{(V_2 - V_4 + V_1 - V_0) \cdot C_{\mathrm{REF}}}{\Delta V} \tag{6.4}$$

where C_{REF} is the capacitance of the reference capacitor.

The CV characteristics are then obtained by acquiring the MIS structure capacitance with the square voltage signal on top of a bias voltage changing in steps between each measurement of the capacitance.

6.2.2 CV data and Modeling

The CV-characteristics obtained for these experiments were fitted with the model described in Sec. 3.2.1. In Fig. 6.5 a representative example of the CV data and the fitted curve can be seen. The CV data is measured in steps of 0.1 V in the accumulation region of the MIS electron emitter in bias voltage. The model has been fitted with allowance for variation of the metal workfunction, the donor concentration, and the oxide thickness.

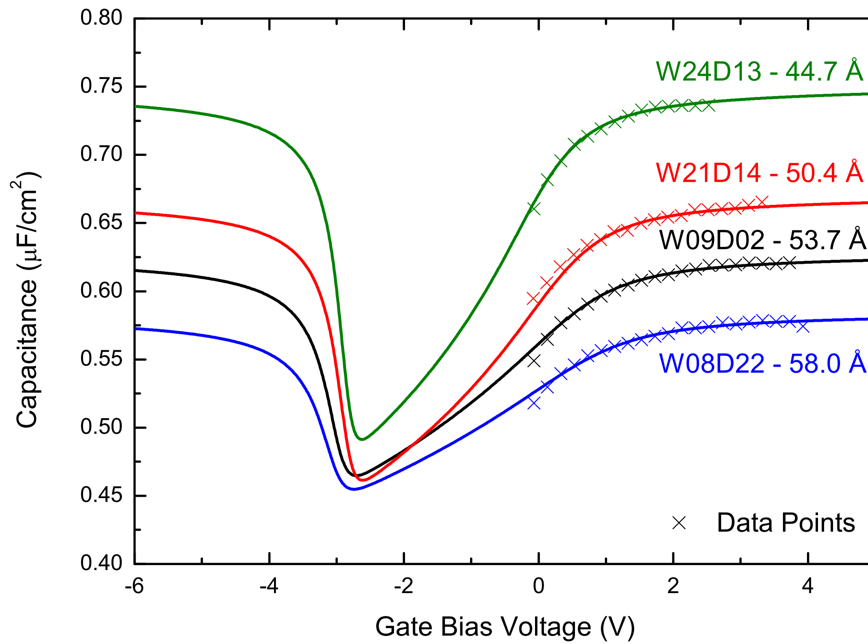

Figure 6.5: Four CV-characteristics obtained on four different wafers from batch 11. The cross symbols refer to the data points measured while the solid lines are the fits to the model described in Sec. 3.2.1. The extracted thickness is shown after each device designation.

Even though there are some discrepancies between the data and the model the thickness of the oxide, which is what is of main interest here, is well-defined to the extent relevant for this discussion.

6.2.3 IV Data

The IV-characteristics were measured by ramping up the bias voltage in steps of 0.05 V and measuring the current at each voltage step using an amperemeter. In Fig. 6.6 several IV curves of 1 cm^2 MIS structures from the four wafers are shown. For each device where the IV curve was measured the CV characteristics was obtained as well and the thickness extracted, is printed after each device designation. The oxide thickness measured by ellipsommetry for each wafer is shown in parenthesis after each wafer number.

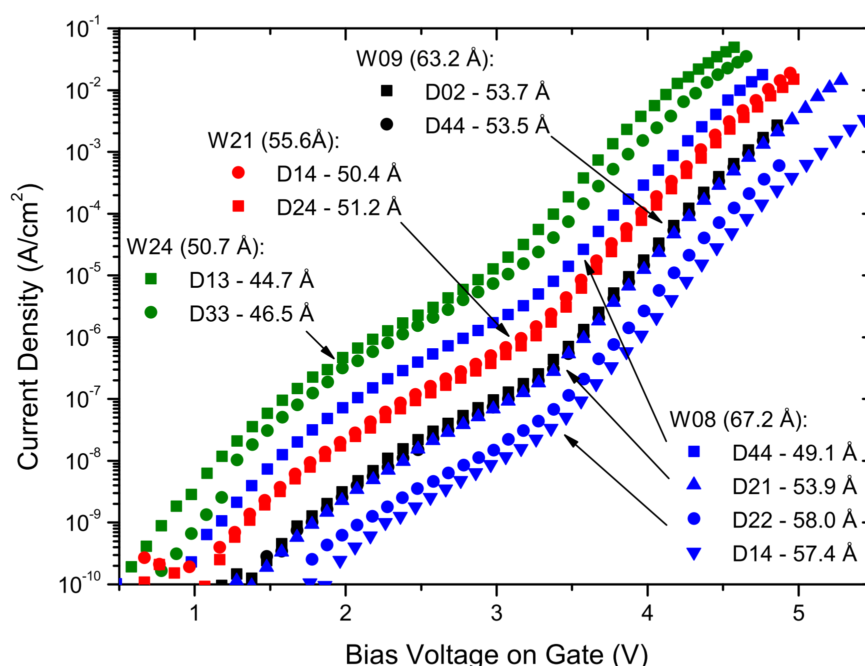

Figure 6.6: Ten IV characteristics measured on 1 cm^2 devices on the four wafers from batch 11. There is clearly variation in the oxide thickness as seen from the current density at a given bias voltage. The higher current density the thinner the oxide. From the indicated thicknesses extracted from CV characteristics and the apparent thickness variation seen in the IV characteristics correspond relatively well.

The IV characteristics in Fig. 6.6 show both qualitatively and systematic agreement to the thickness extracted from the CV characteristics. It is clear from the figure that both variations in the oxide thickness from wafer to wafer, but also from device to device on the same wafer. The thickness variation

across a single wafer is in the range of 5 Å and up to 15 Å from wafer to wafer are seen. Variation in substrate dopant concentration is known to affect oxidation rates [50, 51], which can explain variations in oxide thickness.

6.2.4 Fowler Plots

In order to determine the current transport mechanism through the oxide of the MIS structures the IV characteristics from Fig. 6.6 are shown in a Fowler plot[35] in Fig. 6.7. The IV characteristics yield a straight line in a Fowler plot if the data can be described by the Fowler-Nordheim model of eq. 6.1 which can be rewritten as:

$$\ln\left(\frac{J}{V_I^2}\right) = \ln(A') - \frac{B'}{V_I} \qquad (6.5)$$

where $A' = \frac{A}{X_I^2}$ and $B' = B \cdot X_I$. By plotting the logarithm of the ratio of the current to the oxide voltage squared versus the inverse oxide voltage a straight line is obtained for data in agreement with the Fowler Nordheim equation. From Fig. 6.7 it is seen that above a bias voltage of 3.4 V the data from the IV characteristics agree very well to the Fowler-Nordheim model. This shows that the dominant conduction mechanism of the oxide is tunneling, which is a very important result, since it is a strong evidence that the devices are indeed producing hot electrons in the metal layer.

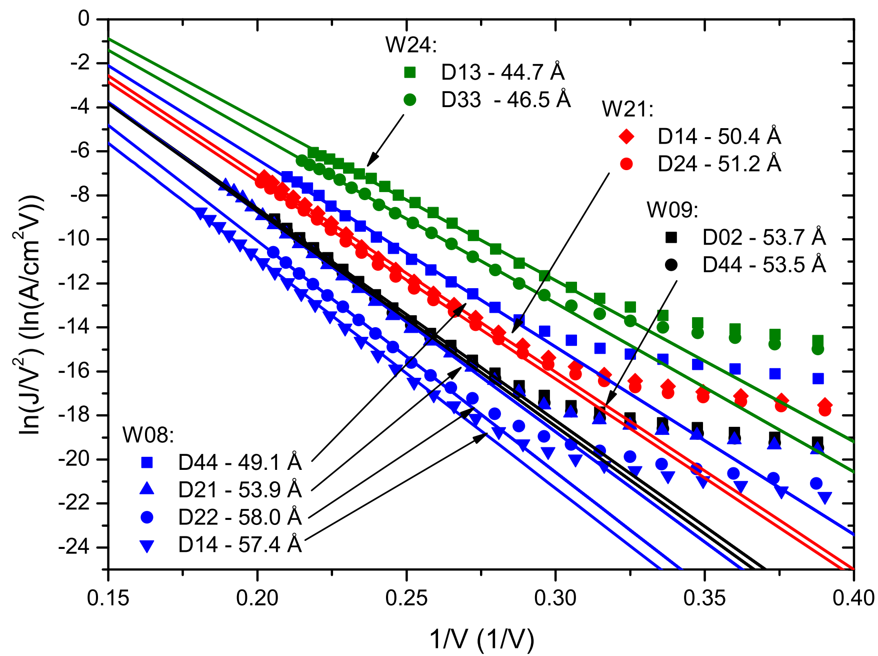

Figure 6.7: The IV characteristics from Fig. 6.6 are plotted in a Fowler plot to evaluate how well they are described by the Fowler-Nordheim model. The data all yield straight lines above a voltage of 3.4 V or ~ 0.29 on the inverse voltage axis which is a strong evidence for tunneling in the devices.

6.3 Thickness Variation

The CV characteristics showed a high variation in the oxide thickness between both devices on the same wafer as well as from wafer to wafer. When comparing the thickness extracted from the CV characteristics with the IV characteristics and the slopes of the Fowler plots there is a qualitatively good agreement. From Fig. 6.6 it can be seen that there is a systematic variation in the IV characteristics with the thickness extracted from CV characteristics. The slopes from the Fowler plots in Fig. 6.7 are plotted against the thickness extracted from the CV characteristics in Fig. 6.8.

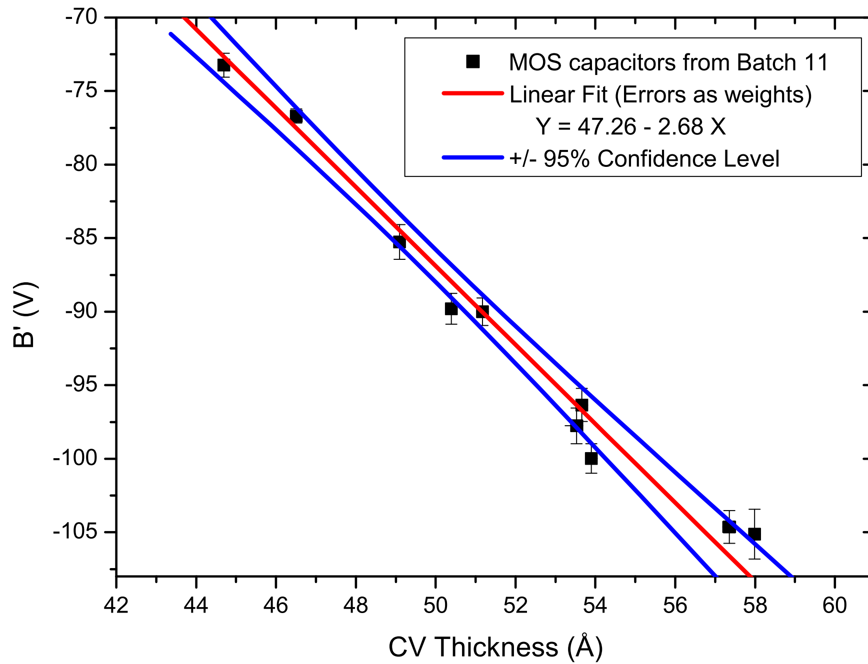

Figure 6.8: The apparent thickness extracted from IV characteristics versus the thickness versus the thickness from CV characteristics for devices from Batch 11. There is a clear linear relation between the thickness extracted from the two measurement types.

From eq. 6.1 it is seen that the slope of the Fowler plot is directly proportional to the thickness of the oxide. One should expect to obtain a straight line through (0,0) when plotting the slope of the Fowler plot against the CV extracted thicknesses, but it is seen from Fig. 6.8 that this is not the case.

The CV thickness versus the slope of the Fowler plot (B') do yield a straight line, but it does not intercept the origin of the coordinate system when extrapolated. The B' value can be converted to a thickness using the linear relation from Fig. 6.8 and the apparent thickness from IV measurements can be plotted versus the CV thickness, see Fig. 6.9. From this figure it is seen that the offset correspond to 17.5 Å. This offset, however, can be attributed to several effects. It could be an overestimate of the thickness from the CV model or it could be due to lowering of the height of the tunnel barrier as a function of decreasing thickness, but the offset do indicate some roughness in the tunnel barrier, as discussed in Sec. 6.1.

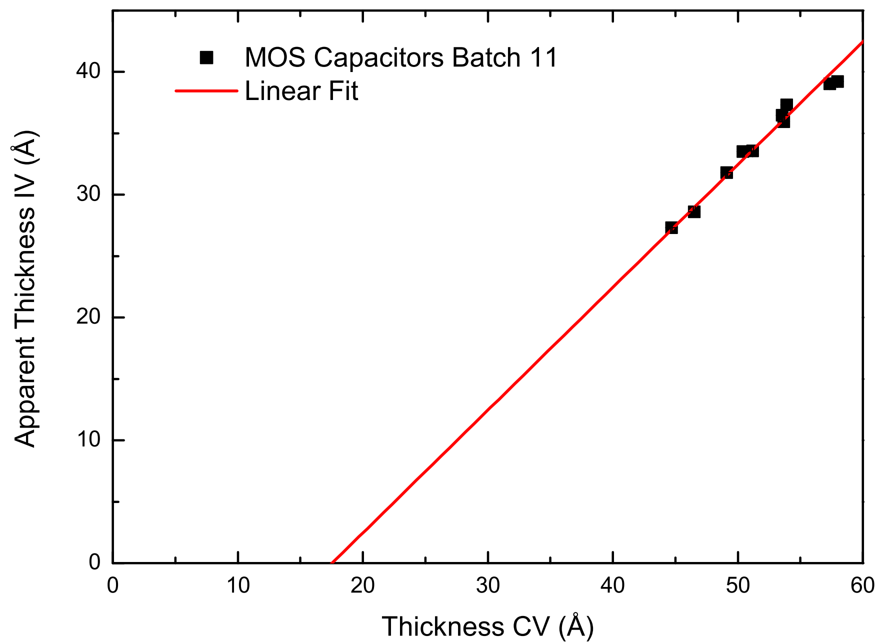

Figure 6.9: IV apparent thickness versus CV extracted thickness. The IV thicknesses are calculated from the B' value divided by the slope from Fig. 6.8.

6.4 Length Scales of the Thickness Variation

To examine the roughness and thickness variation of the oxide in further detail IV characteristics were measured on MIS structures with a range of areas from 1 cm^2 to 100 μm^2 with a decrement in area of a decade between each device size. In Fig. 6.10 seven IV characteristics are plotted scaled with area to show the current density. Only the smallest device lies off the rest in current density with a factor of 2 to 3 lower current density.

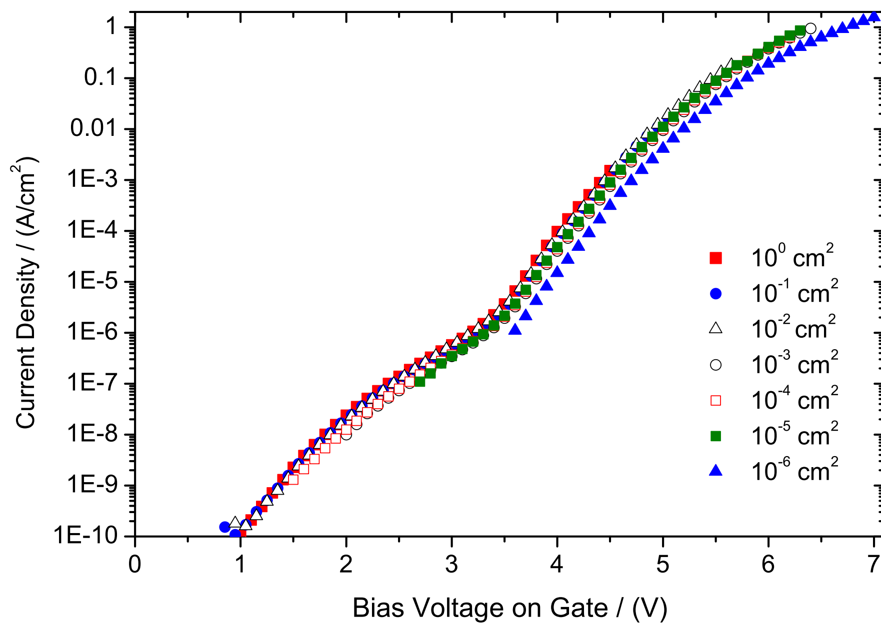

Figure 6.10: The current density versus gate voltage for seven devices with areas ranging from 10^{-6} cm^2 to 1 cm^2. It is seen that the smaller the device the higher voltage the break down voltage, which is well-known from literature [57].

In order to investigate the variations in thickness of the oxide as a function of area the relative offset of the slope extracted from a Fowler plot is plotted against the nominal area of the devices for four series of devices in Fig. 6.11. Each series is seven devices from 1 cm^2 to 10^{-6} cm^2 in oxide area, placed closely together on the same wafer.

As mentioned earlier the slope extracted from a Fowler plot is directly proportional to the thickness of the oxide, the relative offsets in Fig. 6.11 can be seen as variations in oxide thickness. From Fig. 6.11 it is observed that

the smallest devices are measured to have significantly thicker oxide than the larger devices. Furthermore the largest devices show large variations relative to the mean of the seven devices in each series. This way of plotting the apparent thicknesses extracted from the Fowler plots yield information on the variation in the oxide thickness as well as revealing the length scale of the thickness variations or roughness. The reason for the largest devices having a thicker oxide must be due to a gradient in the oxide thickness across the wafer, since roughness that is being averaged over the entire area can only lower the measured thickness compared to smaller devices as discussed in Sec. 6.1. The data in Fig. 6.11 suggest that there are two important length scales in the system. The macroscopic variation of thickness across the wafer on the cm scale as well as a roughness on a microscopic length scale of ~ 10 μm.

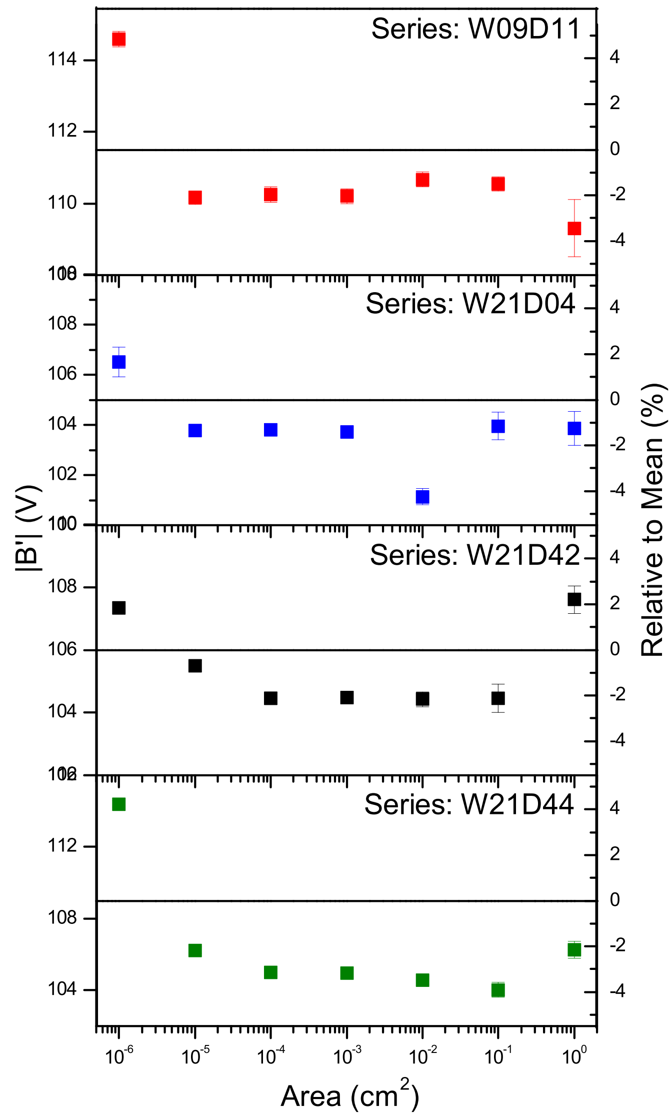

Figure 6.11: The B' value for four series of devices with oxide areas ranging from 1 cm^2 to 10^{-6} cm^2. The small devices yield a significantly larger value of the B' parameter or apparent thickness.

Chapter 7

Electron Emission

The motivation for the design and fabrication of the devices produced in this project is to test the ability for hot electrons to enhance the reactivity of surface reactions. A nice feature of the MIS hot electron emitters is that they can be used as free electron emitters, as was explained in Sec. 3.3. When the bias voltage across the MIS structure is increased beyond the workfunction of the metal gate layer electrons become energetic, or hot, enough to be emitted to vacuum as free electrons. In this way we have been able to emit electrons with efficiencies of up to 8 % at a bias voltage of only 3 V. There are various reports in the literature where MIS type emitters have been investigated [58, 59, 60, 61, 62, 63, 64, 65].

Electron emitters are central to a range of applications [66]: Pressure gauges, electron microscopes, e-beam evaporators, ionizers, mass spectrometers etc. In many of these applications old fashioned hot filaments of tungsten [67] are still in use due to their reliability and low cost. These hot filaments however have several drawbacks such as heat generation, light emission, high pressure incompatibility, poor control of directionality, and outgassing. Almost all of these drawbacks can be remedied by solid-state cold cathodes, which might even be cheaper to produce. Therefore, for decades, it has been the goal to develop solid-state cold cathodes. Today field emitters [65] based on Micro-Electro-Mechanical-Systems (MEMS) technology have found broad application in high-end products such as electron microscopes. The drawbacks of the field emitters are high pressure incompatibility, they are point sources, and need high extraction voltages. These are all drawbacks the MIS emitters do not suffer from. The MIS emitter is operating below 5 V [68], in high pressures of gas [68, 65], and they can be fabricated to emit electrons in arbitrary patterns [69]. The drawbacks of the MIS emitters are low current density and reliability.

The ability to fabricate the MIS electron emitters in various patterns finds

application in eg. Hot Electron Emission Lithography [69] (HEEL) where a MIS emitter is fabricated as a positive mask to emit electrons onto an electron sensitive resist. In this way the high definition of electron lithography can be applied in parallel. Another example of an application where the use of a MIS emitter could be beneficial is in mass spectrometry. Currently most mass spectrometers use hot filaments which outgas molecules which yield a background in the signal, this background could be avoided using MIS electron emitters or cold cathodes in general and in principle give much higher sensitivity of the mass spectrometer.

The electron emission is also a very neat characterization tool for these devices. The electron emission gives information on the energy of the hot electrons, their dispersion in energy, the number of hot electrons that we can expect to generate, and how much of the electrons energy that is lost in the metal layer. This section is devoted to investigate the characteristics of the electron emission from our devices.

7.1 Total Emission Current

To quantify the electron emission from the MIS hot electron emitters the current of emitted electrons was measured by placing a collector plate in front of the device. In this setup both the transmission current, the current through the oxide not being emitted to vacuum, and the emission current of electrons emitted to vacuum is measured. In order to relate the emission current to the transmission current both currents were measured simultaneously as a function of voltage. The setup used for this experiment can be seen in Fig. 7.1. The experiments were carried out in the UHV setup described in chapter 5.

The integrated emission current has been measured for a variety of types of metal layers and thicknesses. As a representative measurement a measurement on a 12 nm Au film on top of a 1 nm Ti wetting layer is chosen. The total emission current along with the transmission current for a typical measurement is shown in Fig. 7.2 as a function of bias voltage.

In the first run the IV of the transmission current curve look very smooth and follows the Fowler-Nordheim relation for the current density which indicates that highly energetic electrons are injected into the conduction band of the insulating SiO_2 layer. The high energetic electrons will be emitted to vacuum if their initial energy is higher than the energy required to escape the metal layer, the work function, and they do not loose too much energy in the process of reaching the metal layer surface. From Fig. 7.2 we see that for the first run emission is appearing from 4.6 V and increasing rapidly from

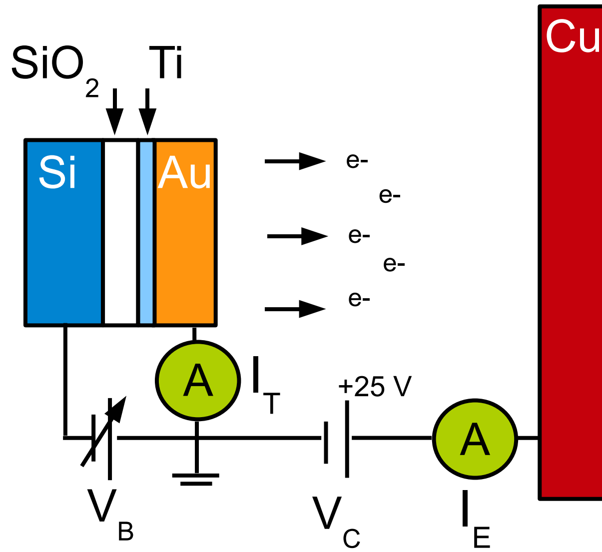

Figure 7.1: Schematic view of the setup used for measuring the integrated emission current from the MIS electron emitters. To the left the MIS emitter is emitting electrons which is collected by the collector plate. The collector plate is biased positively compared to the emitter surface to attract and collect emitted electrons. The emission current (I_E) is measured by an amperemeter and so is the transmission current (I_T).

there on. The apparent work function of 4.6 eV is realistic since no effort was taken to clean the Au surface for carbonaceous residues. The reason for not cleaning the devices was that sputtering the devices in-situ with 500 eV O^+ ions [70] changed the emission current by several orders of magnitude. This was probably due to roughening of the Au surface yielding areas with relatively lower Au thickness. It was very hard to reproduce the effects of this cleaning procedure from sample to sample and it was omitted in experiments where consistent results were more important than overall emission current.

In the second and third run the oxide layer of the device have clearly been damaged and a lot of leakage current is visible. In the higher voltage regime above 4.5 V the Fowler-Nordheim transmission is still dominant. Even though the oxide is damaged the device is still emitting electrons. The emission is the same in the high voltage end, but emission is also appearing at relatively low voltages. The emission at low voltages might be related to pin holes in the Au layer with emission directly from the Ti wetting layer or SiO_2 conduction band.

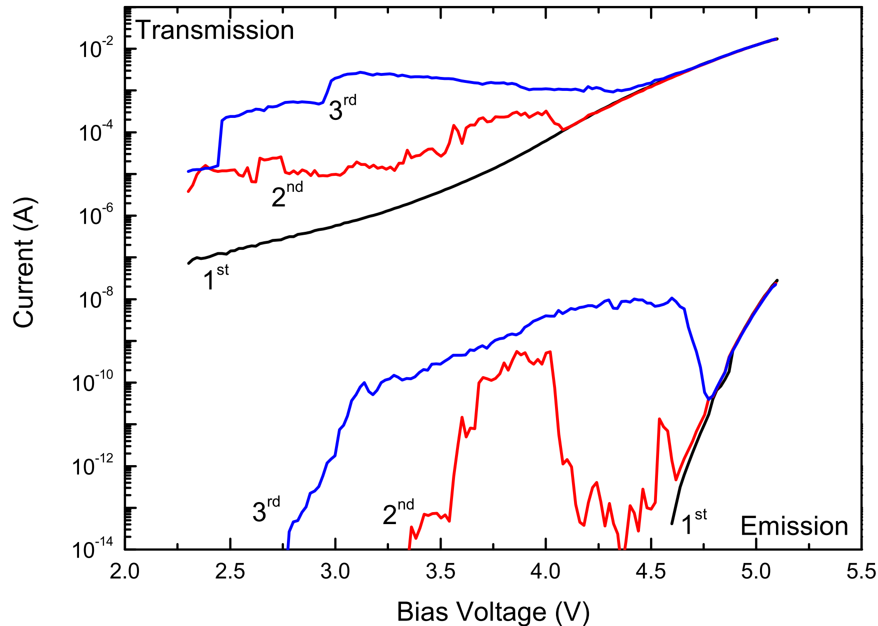

Figure 7.2: The IV characteristics with emission current measured for three consecutive measurements on the same device. In the first measurement the IV characteristics is smooth and emission is seen from above 4.6 V. In the second and third consecutive measurements more leakage current is seen at lower voltages and also some unstable emission, but above 4.6 V the emission curve resembles the one from the first measurement.

7.2 Electron Emission from Cesiated Au

The work function of Au is rather high (5 eV) [71] and only electrons with energy above this value is emitted to vacuum and measured. Therefore it would be interesting to lower the work function of the hot electron emitter surface to increase the emission efficiency. The element with the lowest work function of all in the periodic table of elements is Cs and thus it was the obvious choice for this effort and earlier studies have proven this method successful [72, 73, 74]. The work function of Cs is $\sim$1.9 eV [71] and it is easily deposited using a getter source.

The Cs getter was heated by direct current and the deposition was timed to control the amount of Cs that was deposited. Since this was basic experiments there was no effort to quantify the amount of Cs deposited other than the timing. X-ray Photo-electron Spectroscopy (XPS) was used to detect

deposited Cs on the Au surface, however.

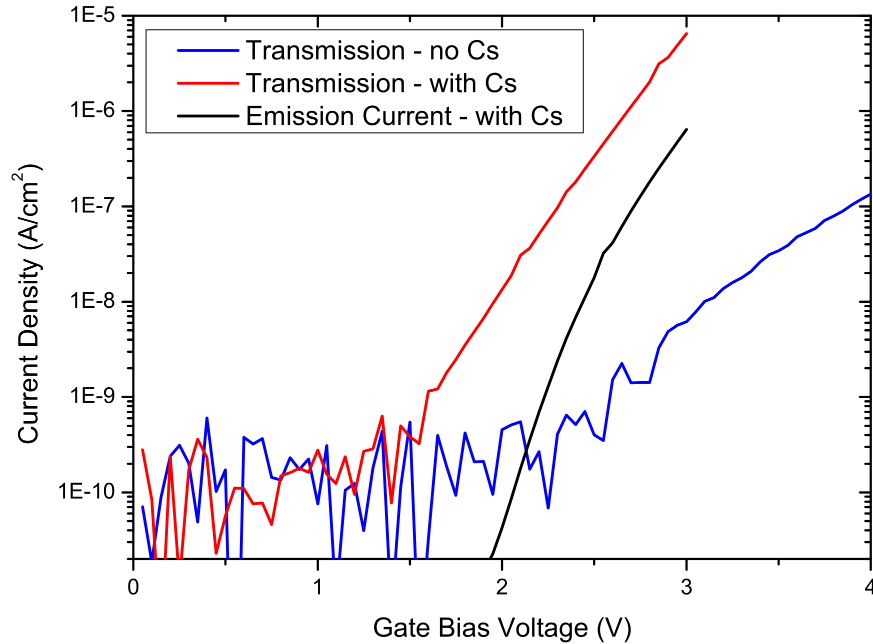

Figure 7.3: The transmission current with and without Cs. The transmission current is clearly affected by the Cs deposition. For the surface without Cs there is no visible emission in the region below 4 V, but with Cs emission is already visible from 2 V. The emission reaches an efficiency of 8 % at 3 V.

In Fig.7.3 the transmission and emission IV characteristics for an Au device with and without Cs is shown. It is clearly seen that the Cs deposited lowers the workfunction of the MIS hot electron emitter. Before Cs deposition no emission is observed below 4 V, but with Cs emission current is already observed from 2 V. The efficiency of electron emission of current through the oxide layer is reaching 8 % at 3 V. The expected Cs coverage is close to 1 mono layer (ML) since the work function is approximately that of Cs cite72.

Another interesting phenomena for the devices with Cs deposited is the change of the IV characteristics for the transmission current. As can be seen in Fig. 7.3 the transmission current is increasing rapidly above 1.5 V. We expect this to be due to Cs deposited directly on Ti or SiO_2 or migrating to the SiO_2 interface. Cs is known to be able to alloy with Au [75]. The lower work function of Cs lower the tunnel barrier and increase the tunnel

current. The effect of Cs deposition increasing the tunneling current has been observed earlier by Hansma *et. al.* [73].

7.3 Extraction of the Mean Free Path

The emission efficiency and the mean free path of the hot electrons in the metal layer are important for the application of hot electrons for enhancing chemical reactions on the surface. The emission efficiency is defined as the ratio of electrons being emitted to vacuum to the total amount of electrons transmitted through the oxide:

$$\eta(E) = \frac{I_E}{I_T + I_E} \tag{7.1}$$

The efficiency is very dependent on the metal layer thickness, the thicker the metal the less electrons will reach the metal vacuum interface with enough energy to overcome the workfunction and be emitted.

The mean free path of electrons is important, since it describes how far an electron with a certain energy can travel statistically in a metal film without scattering and loosing energy. The probability of an electron traveling a distance in a metal without being scattered is given by:

$$P(x) = e^{-\frac{x}{\lambda(E)}} \tag{7.2}$$

where x is the distance traveled and λ is the mean free path of electrons as a function of kinetic energy.

The mean free path can be extracted from a series of efficiency measurements:

$$\eta(\ell) \propto \exp\Big(-\frac{\ell}{\lambda}\Big) \tag{7.3}$$

where ℓ is the thickness of the Au layer. $\eta(\ell)$ is the efficiency as defined by eq. 7.1 as a function of the Au film thickness. The emitter voltage for which the efficiency is extracted must be close to the work function in this type of experiment, since we only want to measure the ballistic electrons and not electrons which have been scattered in the metal layer. For this reason 5 V, which yield electrons of 5 eV kinetic energy in Au and is relatively close to the work function of 4.6 eV of the device, was chosen as the voltage at which the emission efficiency was extracted from transmission and emission current measurements.

In order to determine the mean free path for hot electrons in the Au layers the IV characteristics of the emission and transmission currents were

measured using the same setup as presented earlier in Sec. 7.1. A batch of wafers was fabricated and a 1 nm Ti wetting layer along with an Au layer of variable thickness was deposited as the gate metal layer. Six wafers were produced with Au layer thicknesses from 5 to 60 nm nominally and emission efficiencies for several devices from each of these wafers were extracted. In Fig. 7.4 measurements on a number these devices are presented.

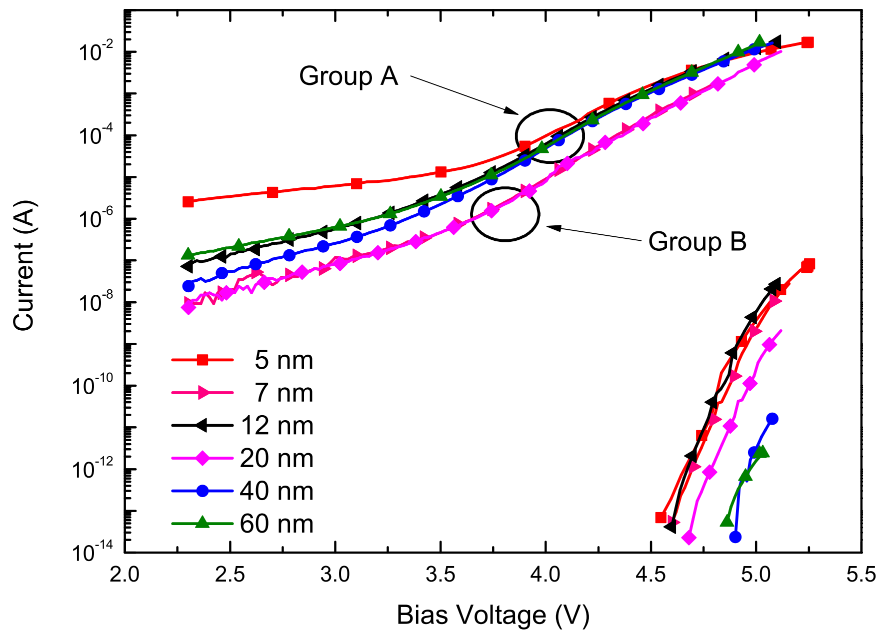

Figure 7.4: The transmission and emission currents for MIS electron emitters with a range of Au metal layer thicknesses from 5 to 60 nm nominal thickness. The oxide thickness of the 7 and 20 nm (Group B) devices seem larger than the rest (Group A), but this does not seem to have an influence on the efficiency of the electron emission as seen in Fig. 7.6.

Using AFM the thickness of the metal layer was measured in several spots on each wafer to yield an average thickness of the metal layer on each wafer. An example of the extraction of the metal layer thickness can be seen in Fig. 7.5.

In Appendix E a calibration between nominal Au thickness and thickness as measured by AFM can be seen.

Fig. 7.6 show the emission efficiency extracted from the measurements shown in Fig. 7.4 versus the metal layer thickness measured by AFM. It is

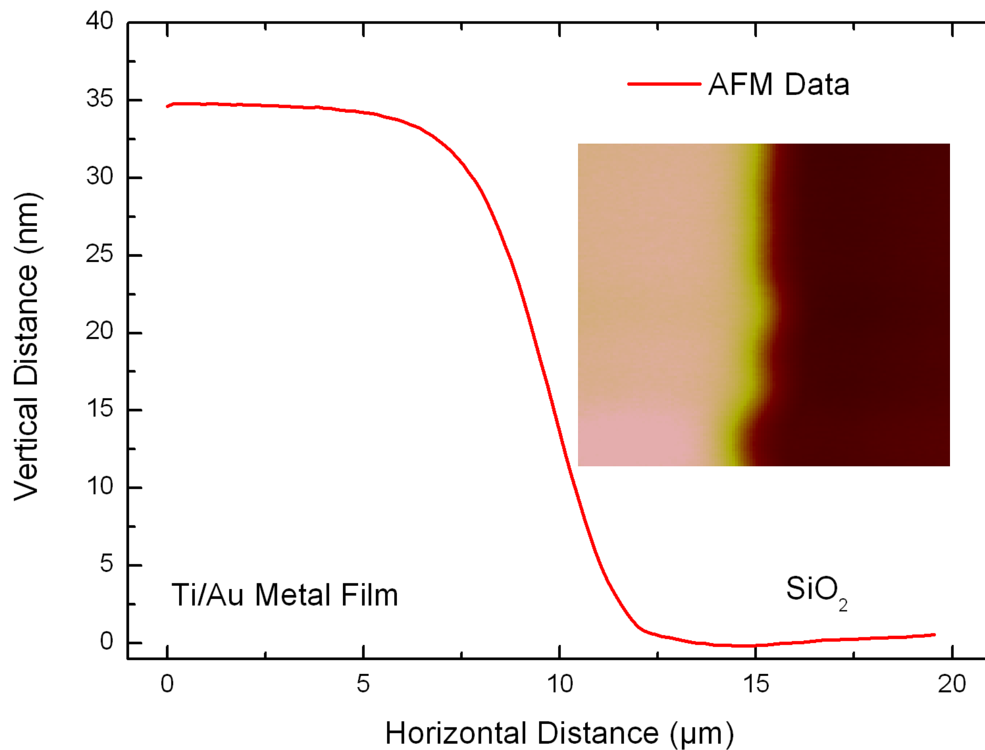

Figure 7.5: The step trace from the AFM image shown as an inset. The AFM image was plane fitted to yield two flat regions. The red line represents the average of all 128 horizontal lines in the image. The step height extracted from this analysis is 35 nm, which is the thickness of the combined Ti Au layer. The nominal thickness for the Au metal film was 40 nm.

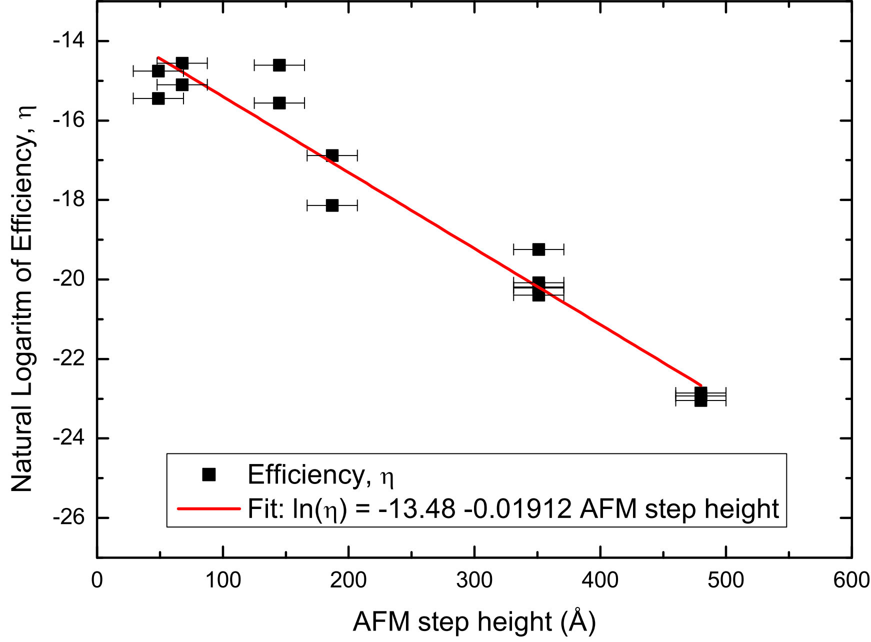

Figure 7.6: The efficiency as a function of Au layer thickness. The electron mean free path is given by the inverse of the slope of the linear fit to the data.

seen that the emission efficiency is decreasing exponentially with thickness. From the figure the electron mean free path can be extracted as the inverse of the slope of the fitted line, as seen from Eq. 7.3; this yields a mean free path of electrons with an energy of ∼5 eV of 52 Å. This is in good agreement with the previously obtained experimental value of 45 Å for electrons with an energy of 5.5 eV [76] and in excellent agreement with the theoretical predictions by Krolikowski *et. al.* [77]. In the region around 5 eV the mean free path is expected to increase towards lower energies [77], which support our observation of a mean free path above what was measured for 5.5 eV electrons.

7.4 Influence of the Ti Wetting Layer

In order to investigate the influence of the Ti wetting layer on the emission efficiency three wafers were prepared with different nominal thicknesses of

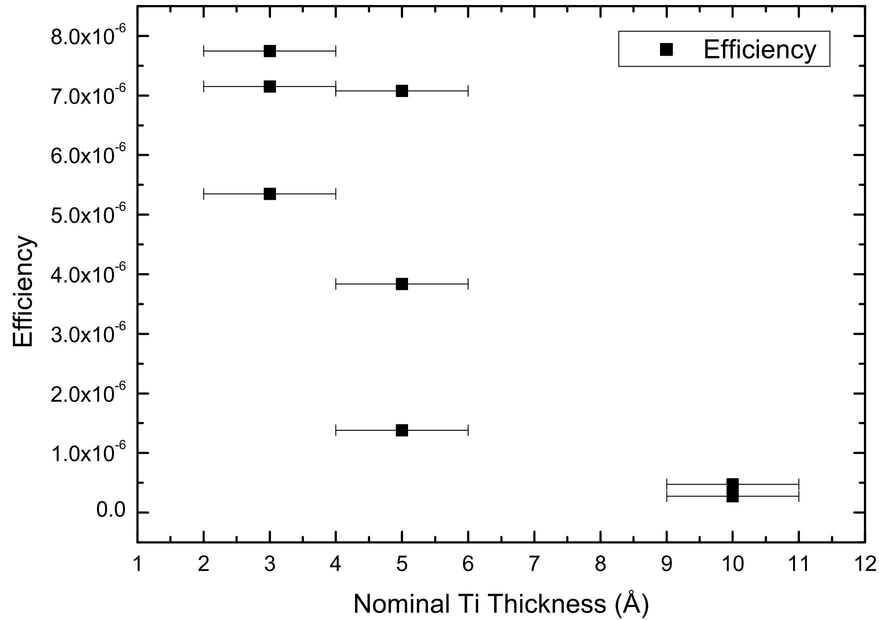

Figure 7.7: The emission efficiency as a function of Ti layer thickness for devices with a 7 nm Au film as the gate layer. The efficiency is dropping approximately one order of magnitude by increasing the Ti wetting layer from 3 Å to 1 nm.

the Ti wetting layer below 7 nm of Au. In Fig. 7.7 the electron emission efficiencies extracted are shown. It is seen that 1 nm Ti wetting layer is lowering the efficiency by an order of magnitude, which is a quite large effect. This high scattering yield of the Ti wetting layer is probably due to the workfunction difference between Ti and Au, which give rise to an electric scattering potential.

This large effect of the Ti layer shows that it would be extremely interesting to avoid a wetting layer all together. Unfortunately a pure Au layer sticks extremely poor to the bare SiO_2, but it is possible to make a Pt metal layer without using a wetting layer. A wafer with a 20 nm nominal thickness Pt film was produced and the emission efficiency was measured. The 20 nm Pt film turned out to give an efficiency of 4.91×10^{-7} at 5 V as high as a 7 nm Au film on 1 nm Ti wetting layer. This is marked with blue in Fig. 7.8.

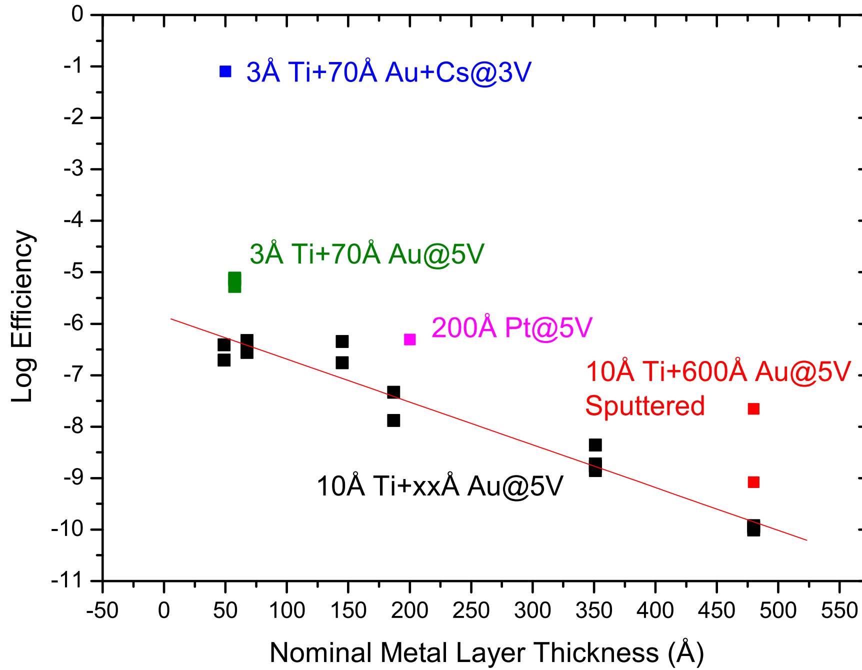

Figure 7.8: Black symbols: Data from Fig. 7.6. Green symbols: Data from devices with 3 Å Ti and 7 nm Au from Fig. 7.7. Pink symbol: Device with 200 Å Pt and no wetting layer. Red symbols: Device with 1 nm Ti and 60 nm Au nominally sputtered for 10 and 20 min. respectively. The longer sputtering time the higher the emission. The Au surface was sputtered using 500 eV O^+ ions. Blue symbol: 3 Å Ti and 5 nm Au nominally with approximately 1 ML Cs deposited and an efficiency of 8 %.

7.5 Overview of Emission Efficiencies

In order to give an overview of the measurements of the total emission and the efficiencies of the different metal layers, the main results from this chapter so far is shown in one plot in Fig. 7.8. The most obvious thing that springs to mind when observing the results in Fig. 7.8 is the great variation in efficiencies from one type of metal layer to the next. It is clear that this is an area where huge improvements are within reach. Either by choosing other metals, workfunction lowering agents, changing wetting layer, tuning the tunnel barrier thickness, or by tuning the morphology by sputtering or annealing the metal layer at higher temperatures.

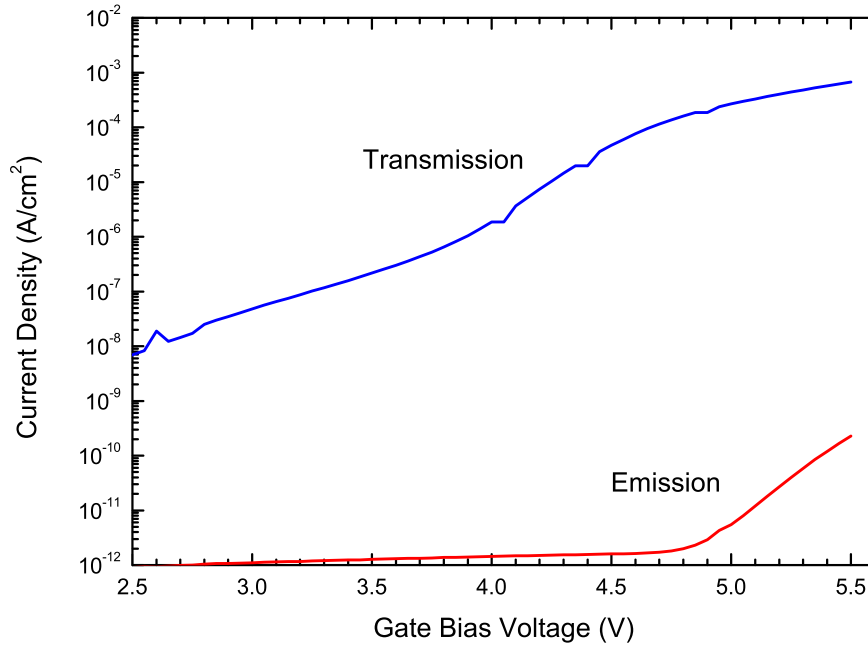

Figure 7.9: The transmission and emission current from a MIS hot electron emitter with a 3 Å Ti and 5 nm Au metal layer under ambient conditions. The spacing between collector and emitter is 0.1 mm. Electrons are emitted at a bias voltages above 4.8 V.

7.6 Electron Emission in Air

As opposed to other types of electron emitters the MIS emitter can be operated under high gas pressures of up to several bars as mentioned earlier. The MIS emitter does not rely on extreme fields across the surface of the devices to emit electrons, such as field emitters [65], and thus they work in any surroundings that are not degrading the device chemically or physically.

In order to test the performance of the MIS hot electron emitters under high pressure, emission measurements were performed under ambient air pressure, as can be seen in Fig. 7.9. The electron emission was measured using a Cu collector plate placed on top of the emitter using a 0.1 mm thick piece of Mica sheet as a spacer and insulator. The collector plate was biased at +25 V compared to the surface of the MIS hot electron emitter. As can be seen in Fig. 7.9 electrons are emitted even in 1 atm. of air.

To test how the emission varies with pressure and gas, a mini reactor

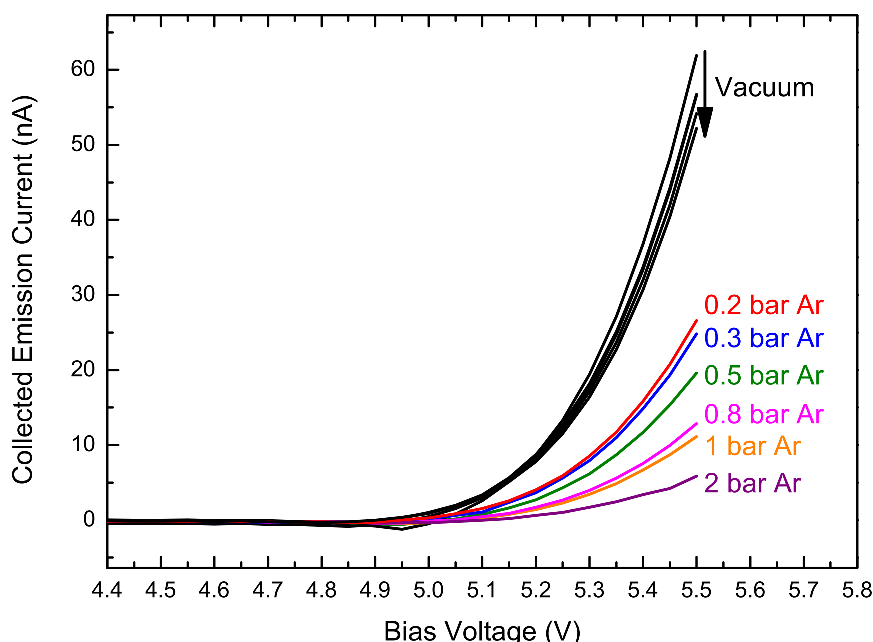

Figure 7.10: The collected emission current for different pressures of Ar. The higher the pressure the lower the collected emission current. Between each measurement at high pressure the reactor is evacuated to vacuum and the collected emission current is measured as a reference. The overall emission current in vacuum was slowly decreasing as the experiments went on, but the pressures at which we measured the emission current were chosen in a random fashion, so this is not the origin of the pressure dependence.

designed by Søren B. Vendelbo, was used in which the pressure, gas and collector voltage could be controlled. The mini reactor could be filled with different gasses and pumped down to vacuum. In this case vacuum is defined as below 10^{-3} mbar. In Fig. 7.10 the collected emission current at several pressures are shown.

From Fig. 7.10 it is seen that the collected current is decreasing rapidly with pressures in the range of bars. At at a pressure of 2 bars of Ar the collected emission current have decreased by a factor of ten compared to the emission in vacuum.

The collected emission current versus gas pressure is presented in Fig. 7.11. It is seen that the decrease of collected emission current as a function of Ar gas pressure is well described as an exponential decay. This could point in

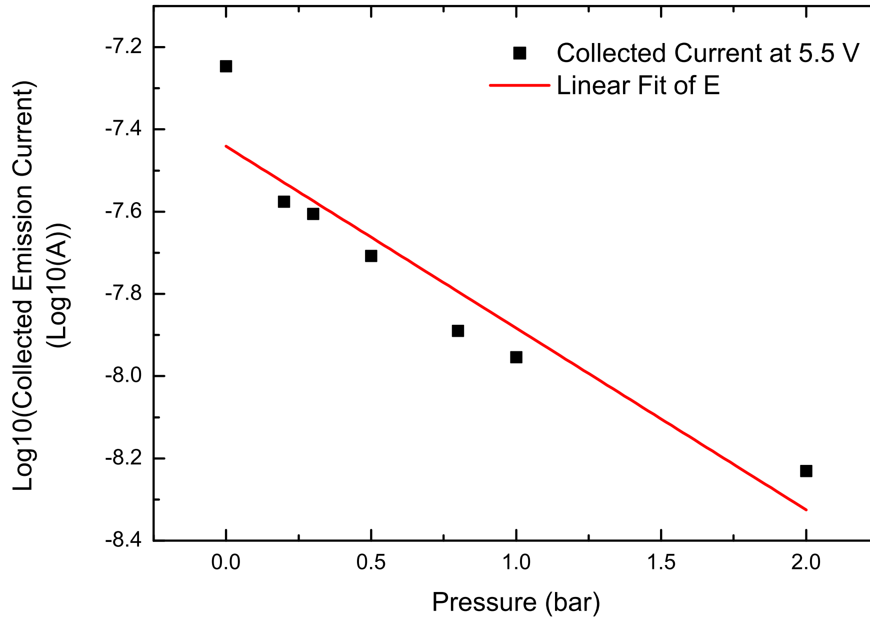

Figure 7.11: The base 10 logarithm to the collected current versus pressure. The data is well-described by an exponential decay as seen from the fitted line. The collected current in vacuum is very high compared to the rest of the data, this is probably due to the lack of scattering here.

the direction that the mean free path of electrons in the gas is important. We suggest that the origin of the pressure dependence is back scattering of electrons in the first sheet of the gas phase within a characteristic distance, where the electrons can be scattered directly back into the surface. This characteristic distance is proportional to the mean free path of electrons in the gas divided by the electric field. This requires the collection efficiency to be a function of collector bias voltage, pressure, gas type and distance. Further away from the surface the electron movement would be described by a Drude type drift velocity, carrying the electrons surviving the first characteristic distance from the device surface to the collector.

Chapter 8

Electron Energy Dispersion

In the last chapter the ability of the MIS electron emitter to emit electrons to vacuum was explored from a quantitative point of view. This is of course important when making an electron emitter for supplying free electrons, but with our objective in mind also the energy dispersion of the hot electrons in the metal layer is important. In order to selectively activate one resonance orbital of an adsorbed molecule on the surface of the device the energy distribution must be relatively narrow. As seen in Sec. 3.3 the theoretical prediction is that the hot electrons entering the metal layer are very narrowly distributed in energy. The electrons have to transverse the metal layer in order to reach the surface of the device, and underway they can be scattered and loose energy and change momentum.

8.1 Experimental Setup

The electrons emitted from the MIS hot electron devices were detected using a standard HemiSpherical Analyzer (HSA) produced by VSW. A diagram of the setup is shown in Fig. 8.1. The radius of the center path between the two hemispheres of the HSA is 100 mm. The potentials of the HSA were controlled by a custom control system comprised of a Data Acquisition (DAQ) Card, an amperemeter and two high voltage supplies. The analyzer was programmed to accept electrons with 5 eV kinetic energy and a pass energy of 1 eV. The sample bias potentials, and thus kinetic energy of the electrons, were scanned compared to the HSA to measure a spectrum of the emitted electrons.

The reasons for implementing a custom control of the HSA were all technical. We learned that the pass energy as set by the standard VSW HAC5000 controller drifted off the set point below 100 eV kinetic energy. Furthermore

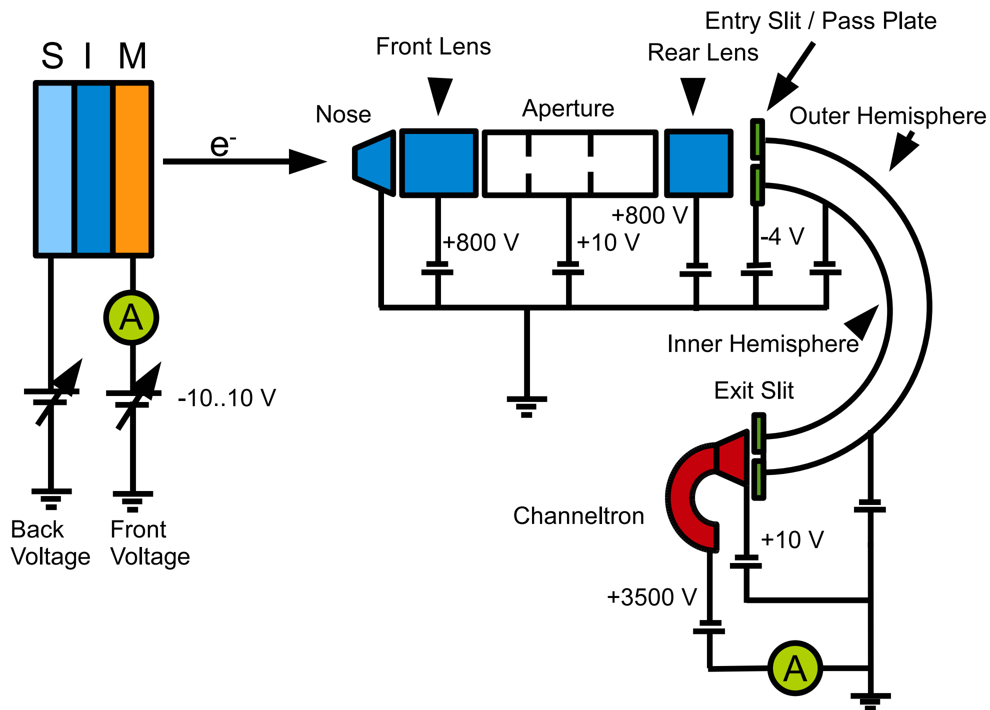

Figure 8.1: Schematic view of the setup to measure electron energy spectra. To the left is the MIS electron emitter comprised of the three layers: Si, SiO_2 and a Ti/Au metal layer. The front and back side potentials are controlled by two voltage supplies and the transmission current is measured using the amperemeter connected to the metal gate layer. Electrons emitted from the surface are entering the HSA through the grounded nose piece and focussed and accelerated by the front lens before entering the aperture where diverging electrons are rejected. After the aperture the electrons are refocussed before reaching the entry slit and pass plate. The pass plate is biased to retard electrons from a preselected energy to the pass energy, defined by the inner and outer hemisphere potentials, which yield the center trajectory. In this case the pass energy is 1 eV and the retarding potential is -4 V so the preselected energy is 5 eV. Exiting the hemispheres, only the electrons close to the center trajectory are allowed through by the exit slit. The electrons exiting through the exit slit have the preselected energy and are amplified by the channeltron and measured using the amperemeter.

the lowest pass energy setting was 10 eV, which resulted in a too low resolution for these measurements and excessively high count rates for our channeltron, which was remedied by decreasing the pass energy to 1 eV giving better resolution and less signal.

As mentioned, the electron current was amplified using a close-ended channeltron with a variable gain, with a stated maximum of $\sim 10^8$ when biased with a high voltage of 3.5 kV across. The high voltage at the end of the channeltron was delivered by a galvanostatically isolated high voltage supply and the amplified electron current was measured on the low voltage side using an amperemeter connected to ground. Measuring the channeltron current using an amperemeter is here labeled as current mode as opposed to the normal pulse counting mode. In pulse counting each electron is counted as a pulse, while in current mode each electron is generating a current pulse. These current pulses averages to a steady current, when a high number of electrons are detected, and this current is then measured as the signal. Due to the resistance of the channeltron being finite ~ 1.75 GΩ there is a bias current at 3.5 kV of $\sim 2\ \mu$A which must be subtracted as a background. In order not to overload the channeltron in current mode, the current corresponding to 100 kCounts/s in pulse counting mode was calculated as:

$$I_{max} = NqG = 10^5\ \text{s}^{-1} \cdot 1.602 \times 10^{-19}\ \text{C} \cdot 10^8 \approx 1.6\ \mu\text{A} \tag{8.1}$$

where N is the maximum pulse frequency and G is the gain. This current was used as the maximum allowed current for measurements. In order to calibrate the gain at different bias voltages across the channeltron an electron spectra was recorded at several bias voltages and a calibration curve was produced by relating the integrals of the signals. The calibration curve can be seen in Fig. 8.2.

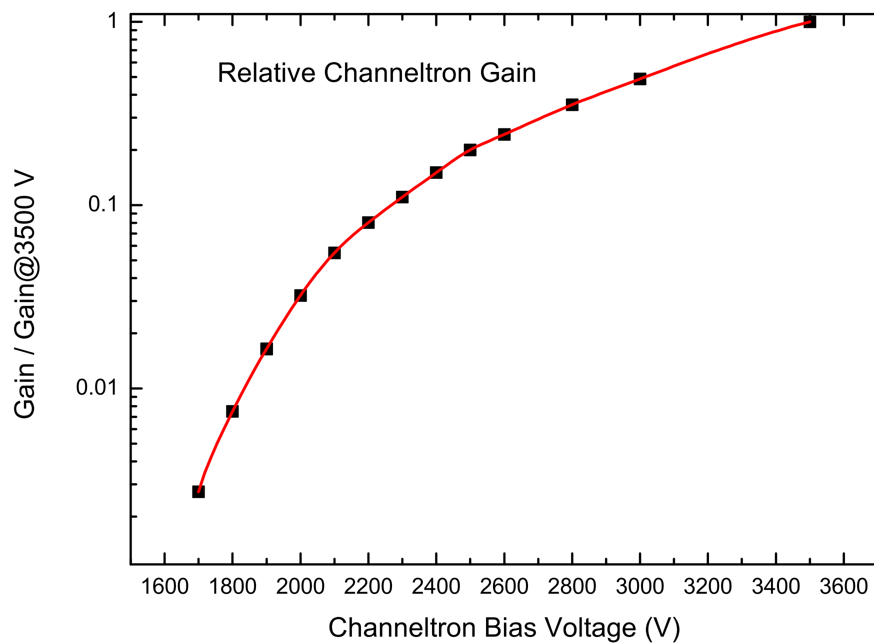

Figure 8.2: Channeltron gain relative to the gain at 3.5 kV as a function of bias voltage across the channeltron. The gain was calibrated using the integrals of spectra obtained from a MIS electron emitter for several values of the channeltron bias voltage.

8.2 Energy Band Diagram

In Fig. 8.3 the energy band diagram for emission of electrons from the MIS electron emitter and detection by the HSA is shown. The kinetic energy measured by the HSA is relative to the vacuum level of the analyzer and the electrons must have a positive kinetic energy to be detected by the HSA. The work function difference between the HSA and the MIS electron emitter results in an electric field which the electron must be able to overcome to be detected. In order to circumvent this issue the MIS electron emitter is biased negatively at -5 V compared to the HSA, accelerating the electrons into the HSA.

From Fig. 8.3 it is also seen that it is the potential of the back side of the device, the Si substrate, that control the kinetic energy, at which the ballistic electrons are detected. The potential of the front metal layer of the MIS electron emitter control the position of the workfunction of the metal layer in the energy spectrum.

One could imagine a potential drop across the metal film due to resistance and what effect it would have on the spectrum measured. The kinetic energy of the hot electrons in the metal will vary with the potential of the metal film, but electrons escaping from regions with a lower potential would see a larger acceleration voltage on the way to the HSA. Thus they will have the same kinetic energy as those from regions in the metal film with large potential at the HSA. This is due to the fact that a lower potential across the oxide of the MIS electron emitter would give an equally larger negative potential difference to the HSA from the metal film. Ballistic electrons from the MIS electron emitter will be measured with the same kinetic energy at the HSA independent on the actual energy in the metal layer. Thus the spectrum cannot be broadened due to potential drops across the metal layer.

Another concern is voltage drops across the wires and contacts resistances. These voltage drops would narrow the spectrum since the workfunction is moving up in energy, while the ballistic electrons move towards lower energies.

8.3 Electron Emission Energy Spectra

The electron emission spectra presented here were obtained using an electron emitter with an area of 2 mm^2. The electron emitter was fabricated with a target oxide thickness of 50 Å and a metal gate layer consisting of a 1 nm Ti wetting layer and a 7 nm Au layer.

In Fig. 8.4 normalized electron emission spectra are shown for bias voltages from 5.0 V to 6.3 V. The first spectrum at 5.0 V shows a distribution of

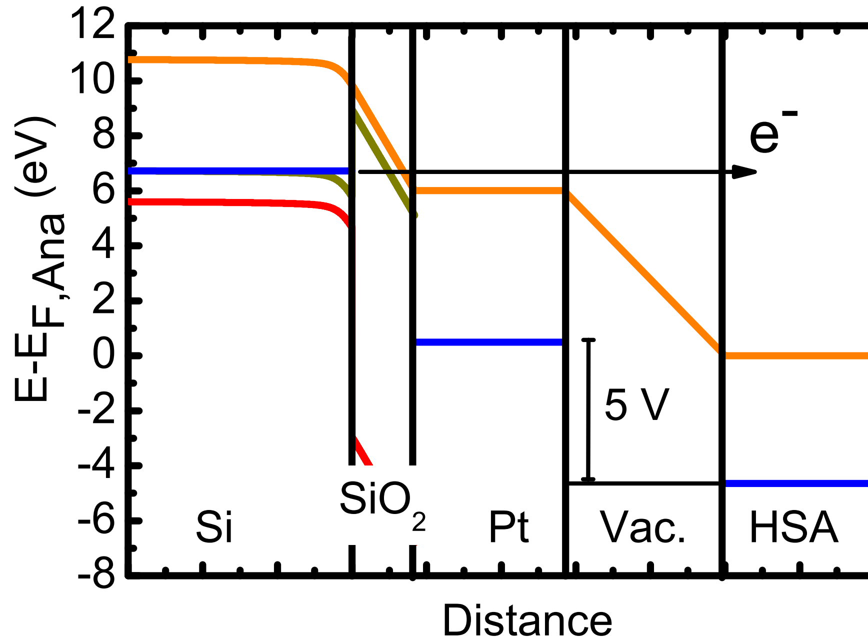

Figure 8.3: (Color convention as in Fig. 3.2). The energy diagram for electron emission from a MIS electon emitter and detection by the HSA. The kinetic energy measured by the HSA is relative to the vacuum level. The sample bias voltage of 5 V indicated secure that the electrons have enough kinetic energy to overcome the electric field between the device and the HSA, due to difference in work functions. For ballistic electrons it is the Fermi level of the Si that controls the final kinetic energy at the HSA detector. A potential drop across the front metal film would change the position of the vacuum level relative to the detector across the device.

electrons emerging from beyond the workfunction. The very sharp cut-off to low energies around 0.5 eV is due to the workfunction of the metal layer. At higher bias voltages a ballistic peak is emerging moving proportionally to the increase in bias voltage. The peak has a tail of scattered electrons towards the workfunction. The workfunction remains relatively well-defined over the range of the spectra.

The energy axis in Fig. 8.4 is relative to the vacuum level of the HSA which is 4.65 eV. The cut-off due to the workfunction of the device metal layer at 0.5 eV yield a workfunction of 5.15 eV, which is very realistic for an Au surface[71].

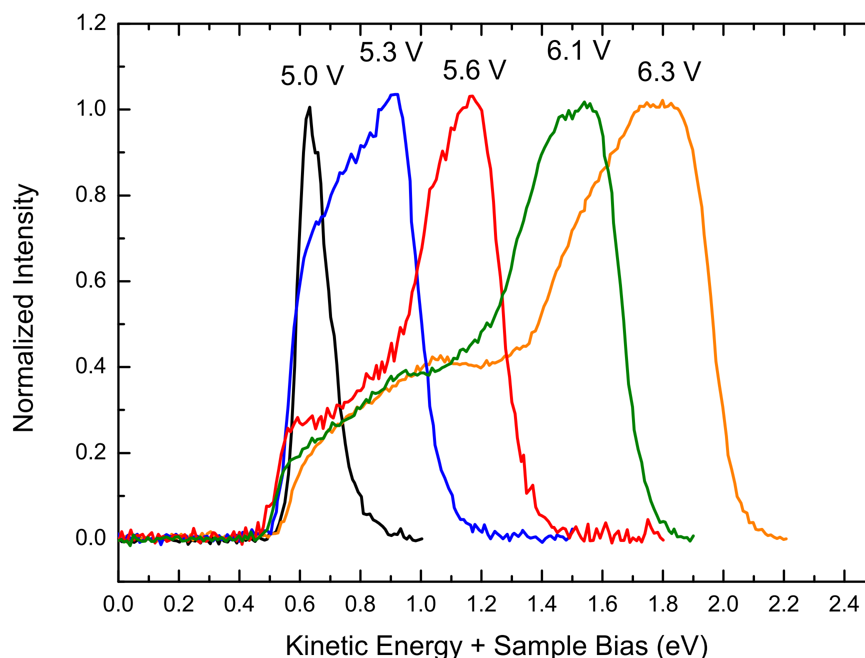

Figure 8.4: Five emission spectra obtained on the same MIS electron emitter for different bias voltages across the oxide. The first emission spectrum obtained for a bias voltage of 5.0 V is very narrow with a very sharp cut-off towards lower energies. This cut-off is due to the work function which set the lower limit in energy for electrons escaping the Au surface of the device. For higher bias voltages the high energy flank of the distribution moves towards higher energies and a peak is evolving which moves with bias voltage while second order electrons are tailing down to the work function cut-off defined by the low energy flank of the 5.0 V spectrum. The energy axis is relative to the vacuum level of the HSA which has a workfunction of 4.65 eV. This indicates a workfunction of 5.15 eV for the device. The FWHM of the peaks go from 0.3 to 0.5 eV.

Fig. 8.5 shows the spectra from Fig. 8.4 but with the intensity calibrated using the calibration shown in Fig. 8.2. The intensity is rapidly increasing with bias voltage as was also seen from the total emission spectra.

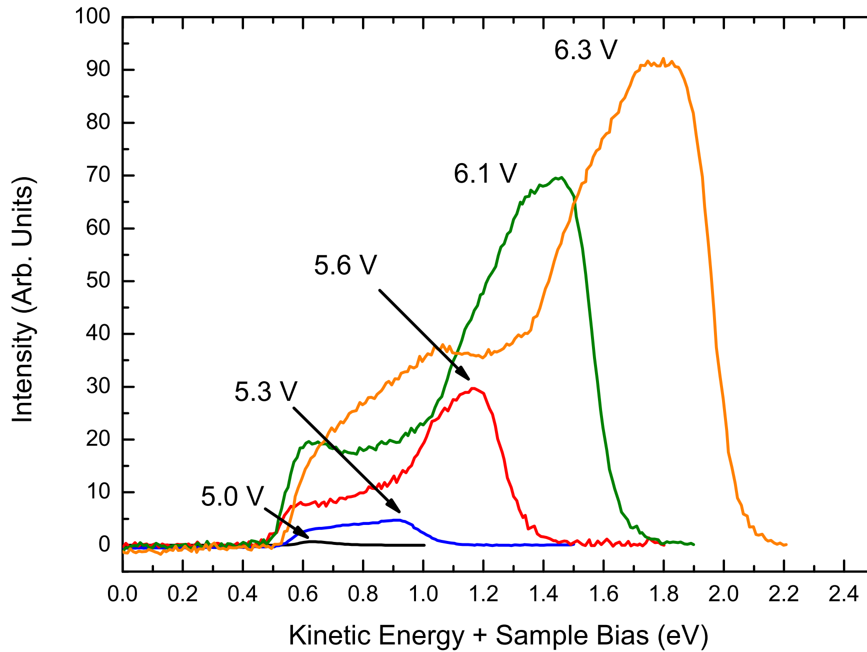

Figure 8.5: The emission spectra from Fig. 8.4 calibrated using the data in Fig. 8.2. The emission intensity is increasing with bias voltage and the emitted electrons move to higher kinetic energies.

In Fig. 8.6 the position of the high energy flank is plotted against the bias voltage. Furthermore the position of the peak maximum is plotted. The two data series are fitted with a linear line with a slope of one, showing that the electrons with highest energy in the distribution move proportionally in energy with the increase in applied bias voltage. This is strong evidence that the observed peak is consisting of ballistic electrons with a narrow distribution in energy.

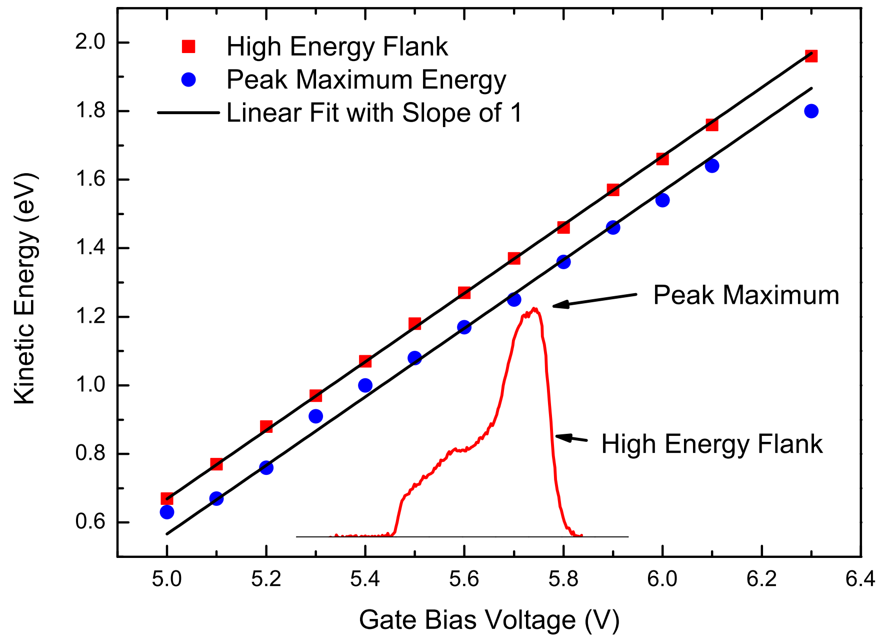

Figure 8.6: The position in energy of the high energy flank and maximum of the emission peaks from Fig. 8.4 as a function of applied bias voltage. The high energy flank is defined as the point with the steepest slope on the high energy side of the peak in the emission spectrum. The linear fits with a slope of one indicate that the kinetic energy of the emitted electrons increase proportionally to the increase in applied bias voltage, as it is expected for ballistic electrons.

Chapter 9

Towards Hot Electron Chemistry

In order to study surface chemistry enabled by hot electrons from our MIS hot electron device it has been characterized in the previous experimental sections with regard to oxide thickness and roughness, metal layer thickness and electron emission. In this chapter the focus is on the early attempts to observe basic reaction steps such as desorption activated by hot electrons.

To even get to the situation of attempting hot electron chemistry using the MIS hot electron emitter some prerequisites must be available, such as a clean surface of a suitable metal on top of a working MIS device. A system consisting of the metal layer, forming the template for hot electron chemistry, and the reactants must be selected. A strategy for the measurement technique and procedure must be found and an estimate of the detection limit and amount of products would be beneficial. These challenges are addressed in this chapter.

9.1 Choice of Test System

Platinum was chosen as the metal layer due to several advantages. Pt hardly oxidizes, binds several gas phase molecules at room temperature, such as CO and NO, and can deposited in thin films on SiO_2 by PVD without a wetting layer. The reactivity of Pt is used in a self-cleaning procedure where carbonaceous residues are combusted using O_2 as is demonstrated later in this chapter.

The target reaction which we chose was desorption of CO from the Pt surface. CO binds very well to Pt ($E_D = 1.37$ eV [32]) and has a high coverage of 0.5 monolayers (ML) at room temperature on Pt [78]. A high saturation

coverage and a low desorption rate at room temperature are essential to be able to measure desorption induced by hot electrons. A high coverage yield a high probability for a hot electron hitting a target molecule and a low desorption rate makes it possible to conduct long lapsed batch experiments. A drawback of using CO is that it has a high background pressure in the UHV chamber from hot filaments. This was somewhat remedied by using isotopically labeled CO (^{13}CO) as the test molecule, which has a factor of 100 lower background pressure due to the 1% ^{13}C to ^{12}C ratio present in nature [79].

9.2 Heating and Temperature Monitoring

The MIS electron emitter can be heated by driving a current through the metal film in this case Pt. The advantage of this technique over indirect heating, such as using a tungsten filament, is that the power is deposited in the metal film alone. This allows for faster heating, faster cooling, and less outgassing from external parts. After heating to 300 °C using the filament in the sample stage the cool-down time to 30 °C was approximately two hours, which was shortened to approximately 20 min. by heating using the metal film. Furthermore the outgassing from the sample stage getting hot was circumvented almost completely.

Another feature of the Pt thin film is the temperature dependence of the resistance. One problem we discovered was that our thermocouple pressed to the backside of the device was way off the real temperature of the sample. A resistance measurement however would give a much more accurate measure of the temperature of the Pt film, assuming that a good calibration could be obtained.

We noticed that when our MIS device was cooling down from a heating cycle the resistance would become linear to the temperature measured by the thermocouple which indicated that the thermocouple and the device were in thermal equilibrium, an example of this is seen in Fig. 9.1. Using the Thermal Coefficient of Resistivity (TCR or α) of Pt the resistance at 20°C could be extrapolated, and using the width and length of the Pt metal film, the thickness of the film could be estimated. A step through of the analysis is given here.

In general the resistance as a function of temperature can be expressed as [80]:

$$R(T) = R_0(1 + \alpha T) \tag{9.1}$$

where R_0 is the resistance at 0°C . The slope of the fit from Fig. 9.1 is denoted A. From A the value of the resistance at 0°C can be found as:

$$R_0 = \frac{A}{\alpha} \tag{9.2}$$

The geometric resistance of the Pt film is given by:

$$R = \frac{\rho L}{wX} \tag{9.3}$$

where ρ is the resistivity, L is the length, w is the width and X is the thickness of the film. By combining equations 9.1 and 9.3 the thickness of the film is determined:

$$X = \frac{\rho L}{wR_0(1+\alpha T)} = \frac{\rho L \alpha}{wA(1+\alpha T)} \tag{9.4}$$

For nominally 20 nm Pt films the extracted thickness yields 16 nm, which is very consistent. This result becomes even more consistent when it is compared to the results for the thickness measurements by AFM presented in Fig. E.1. Applying this calibration yield a thickness of 17.5 nm for the Pt metal film. In the above analysis an α-value of 0.00395 °C^{-1} [81] and a resistivity (ρ) at 20 °C of 11×10^{-8} Ω cm [81] were used.

With this consistency check worked out the temperature can be obtained using the linear fit from Fig. 9.1 as:

$$T(R) = \frac{R - R_I}{A} \tag{9.5}$$

where R_I is the intercept from Fig. 9.1. The contact and lead resistance can also be estimated from this analysis as:

$$R_C = R_I - R_0 \tag{9.6}$$

Which yield a contact resistance of 4.85 Ω for the data presented in Fig. 9.1. The calibrated temperature scale from the analysis presented is given as the right axis in Fig. 9.1. The most probable sources of error for this type of temperature calibration, other than unlinearity of the TCR value as a function of temperature, is annealing and morphology changes in the Pt film at high temperatures. To circumvent errors induced from annealing the cooling slope after each heat up can be used for calibrating the temperature scale for the next heating cycle. The accuracy of this method could be improved significantly by four terminal resistance measurements by eliminating R_C.

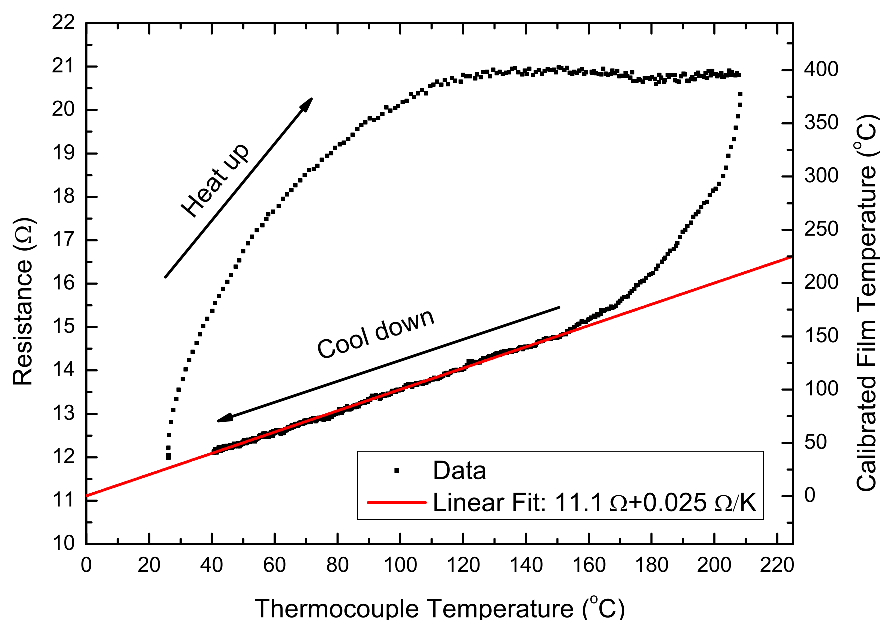

Figure 9.1: The resistance of the Pt metal film versus the temperature measured by the thermocouple pressed against the backside of the MIS device in the sample holder. The heating current used was 0.3 A. The resistance increases very rapidly in the heat up compared to the temperature of the thermocouple (TC) indicating that the TC is lagging behind the temperature of the Pt film. On the cool down the resistance becomes linear with the TC temperature indicating equilibrium. The red line is a linear fit to the data on the cooling slope. From the fit the resistance can be translated to a temperature. The calibrated temperature scale of the Pt film is shown as the right axis. The fact that the resistance of the cool down undershoots the resistance before the heat up indicate annealing of the Pt film decreasing the resistance.

9.3 Cleaning Platinum

Since Platinum was chosen to be the metal for the experiments with hot electron chemistry it was necessary to find a way to clean it in-situ. Pt was deposited on our devices in the cleanroom by PVD, as described in Sec. 4.1, and had been exposed to air before being placed in the UHV chamber for hot electron experiments. Even though Pt was deposited using a shadow mask it very quickly developed several monolayers of carbonaceous residues on the surface as can be seen in XPS[1] spectrum of the surface in Fig. 9.2. A quantitative analysis of the relatively weak carbon peak (C1s) marked in the spectrum actually corresponds to several MLs of carbon on the surface. The surface need to be absolutely clean for the reactant molecules such as CO and NO to stick to the surface. Thus a good cleaning procedure was needed.

There are two very common ways to clean surfaces in UHV surface science, they are sputtering and heating, often in reactive gasses. Sputtering is often very efficient and work by bombarding the surface with ions of eg. Ar or Ne having energies in the keV range. In our case sputtering is not a good solution since the energetic ions penetrate through the thin metal layers and induce defects into the oxide layer ruining the device [70].

Instead another approach was taken where the MIS electron emitter was heated to approximately 400 °C in a background pressure of O_2 of 3×10^{-7} mbar. By following the relevant masses in the mass spectrometer the cleaning process can be monitored, as seen in Fig. 9.3. The heating of the device begin after 60 s and the temperature is increasing rapidly. When the temperature reaches 100°C CO[2] begin desorbing from the device along with H_2. A small dip in the O_2 signal is observed at the same time , which is either due to combustion of C-species using O_2. After approximately 115 s at a film temperature of approximately 250°C a large dip in O_2 is observed along with a peak in CO_2, which is probably due to ignition of Pt and subsequent burn-off of carbon species from the surface forming CO_2 by a reaction with O_2.

[1]For a description of the XPS technique and quantitative analysis see reference [82]

[2]The signal with a charge to mass ratio of 28 in Fig.9.3 is assigned to CO and not N_2 due to the lack of signal with a mass to charge ratio of 14 (not shown).

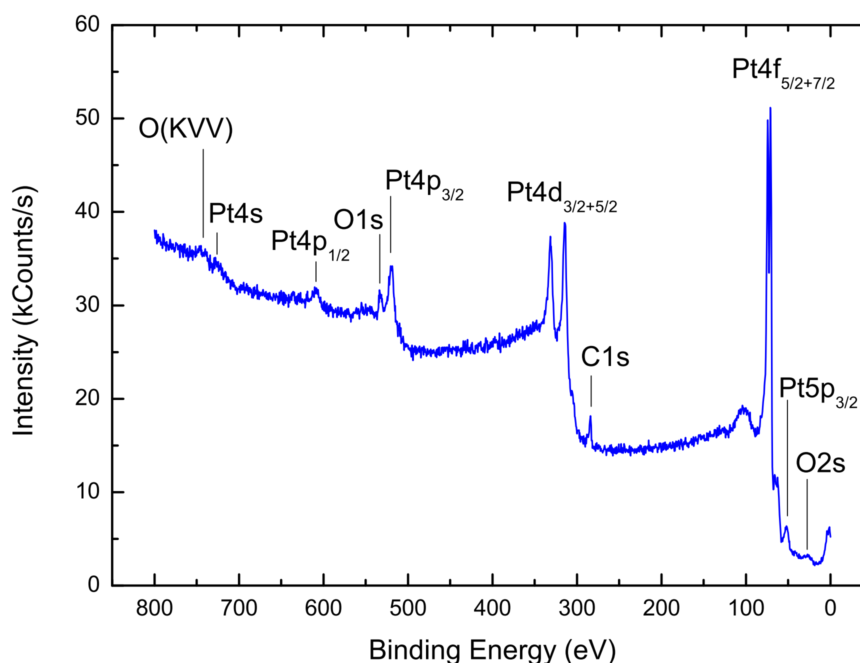

Figure 9.2: An XPS overview spectrum of a MIS hot electron emitter with a 20 nm Pt metal layer. The peaks of Pt are dominating the spectrum, but also O and C are present. The O contribution stem from either carbon related surface species or the SiO_2 parts of the device. The carbon stem from residues of pollution from sources such as storage under ambient conditions, pump oil, hot filaments etc. The carbon peak (C1s) at 287 eV seem insignificant, but the so-called Atomic Sensitivity Factor (ASF) for the C1s peak is only 0.205, while that of the $Pt4f_{7/2}$ peak is 1.75. This means that the area of the C1s peak must be multiplied by 8.54 to compare to the $Pt4f_{7/2}$ peak.

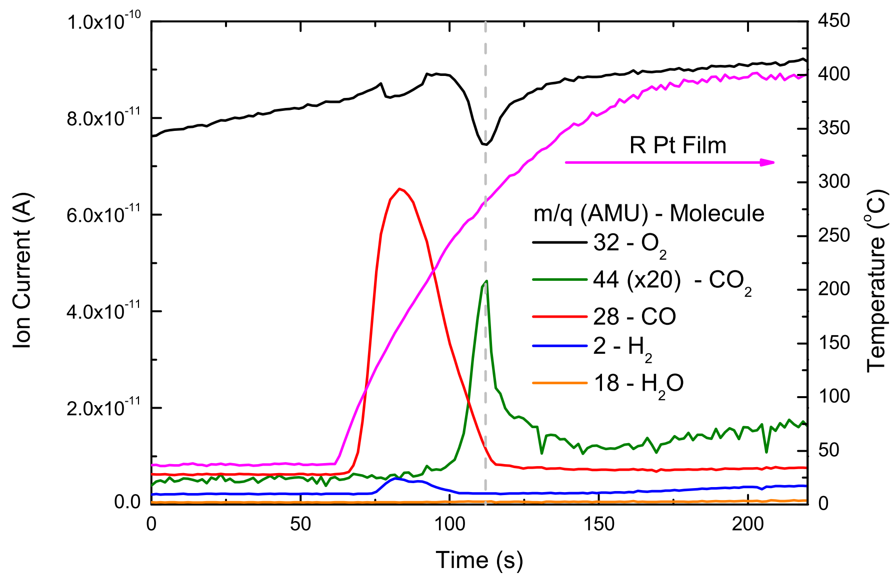

Figure 9.3: This figure is showing the signals obtained by the mass spectrometer during the cleaning procedure of heating up the device in a background pressure of 3×10^{-7} mbar of O_2. CO and H_2 are desorbing from 100°C to 300°C while O_2 is consumed by combustion of carbon residues around 250°C producing CO_2.

After the burn-off of carbon the surface is presumably clean. The cleanliness of Pt can be tested by letting in CO, which will be oxidized to CO_2 on the free Pt sites at these temperatures[83, 84]. In Fig. 9.4 labeled CO (^{13}CO) is introduced in the chamber. As the labeled CO is introduced O_2 is consumed and labeled CO_2 is produced indicating a clean Pt surface.

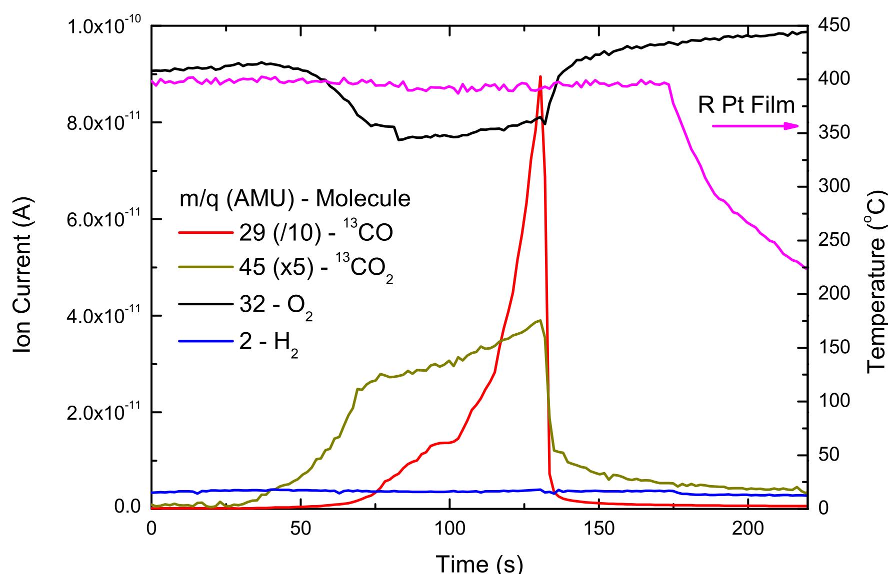

Figure 9.4: CO oxidation on Pt in a background pressure of 3×10^{-7} mbar. (^{13}CO) is introduced and oxidized by O_2 on the free Pt sites producing CO_2. For a dirty Pt film no CO_2 is produced when introducing CO in an O_2 background pressure.

For another MIS hot electron emitter the cleanliness of the Pt surface was checked using XPS before and after the same cleaning procedure as can be seen in Fig. 9.5, where spectra of the Pt and C windows are presented. The Pt signal has increased after the cleaning procedure because of less damping by carbon and the Carbon signal has vanished altogether. Before the cleaning a quantitative analysis yielded 48% Pt and 52% C assuming a homogeneous distribution of Pt and C in the sample. This is however not a good description, since it is more favorable for C to sit on the surface and this signal therefore probably correspond to several monolayers of carbon.

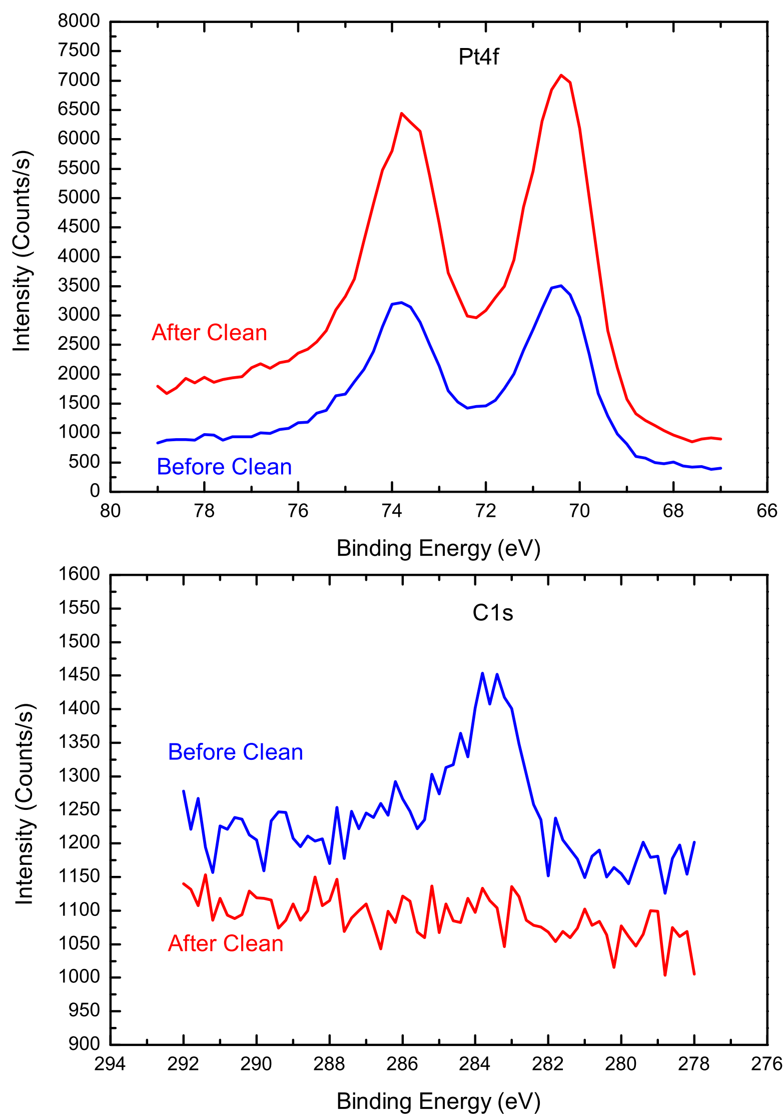

Figure 9.5: XPS spectra of the Pt4f peaks and the C1s peak before and after the cleaning procedure. The intensity of the Pt4f peaks have increased after the cleaning procedure. The reason for the increase is the removal of the carbon residues damping the signal from Pt. The C1s peak has vanished from the cleaning procedure showing that the carbon residues have been removed by the cleaning.

In Fig. 9.6 an Ion Scattering Spectroscopy (ISS)[3] spectrum is shown showing only scattering of He^+ ions at an energy corresponding to Pt and a very small background in the low energy region corresponding to low mass elements in the surface or the regions next to the Pt film.

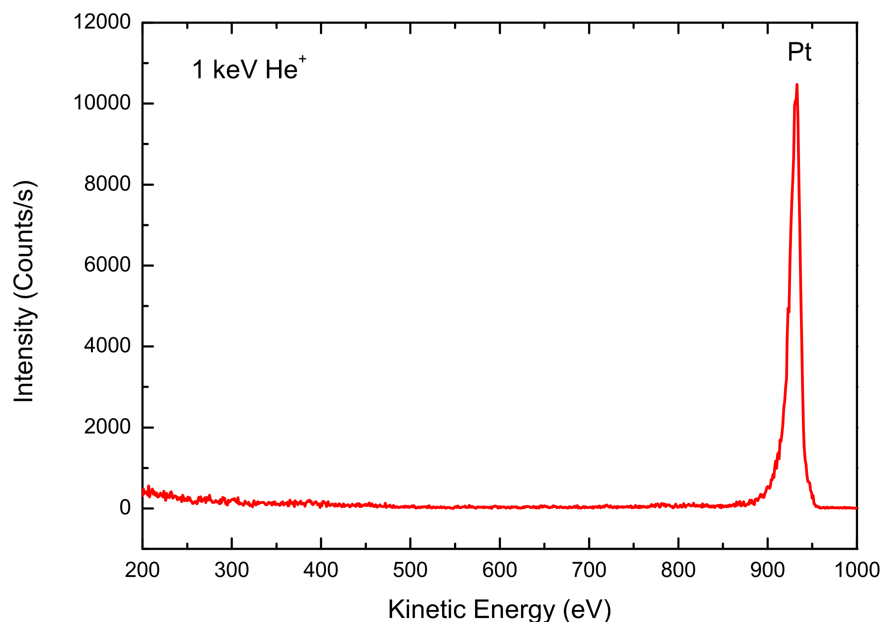

Figure 9.6: Ion Scattering Spectrum of the surface of Pt film after cleaning. The peak at 935 eV is from Pt in the surface layer. Due to the high probability of neutralization of the incoming He^+ ions in ISS the spectrum only show the first surface layer of the sample. No other elements are observed in the surface.

[3]For a description of the experimental technique of ISS see reference [82]

9.4 Thermal CO Desorption

In order to measure the amount of CO adsorbed on the cleaned Pt surface and to estimate the detection sensitivity of the mass spectrometer setup CO was made desorb from the Pt surface by thermal activation. As in the cleaning procedure, the Pt film was heated using a direct current of 0.3 A through the Pt metal film heating the device rapidly from room temperature to approximately 300°C in order to desorb CO and other adsorbed species.

Labeled CO was adsorbed from the gas phase after cleaning by cooling the device in a background pressure of labeled CO (mass 29 AMU) of 1×10^{-7} mbar supplied from a leak valve. The leak valve was closed when the temperature of the device reached 39°C measured with the thermocouple. The desorption measurement was initiated when the device had cooled to 34.5°C .

A few examples of CO desorption experiments are shown in Fig. 9.7. CO is desorbed in a broad peak with maximum between 120 and 150°C with a low shoulder extending to 300°C . These desorption measurements compare relatively well with results reported in the literature[78, 85]. The main broad peak in the measurement is due to CO desorption from terraces with close-packed surfaces while the shoulder extending up in temperature to 300°C is probably due to desorption from corners and steps in the Pt film known to bind CO more strongly[86].

The desorption peaks from four measurements shown in Fig. 9.7 express a relatively good reproducibility of consecutive desorption experiments on the same device. The standard deviation in the area of the peaks is 10^{-10} C or about 7% of the mean value, however it should be possible to improve on this result.

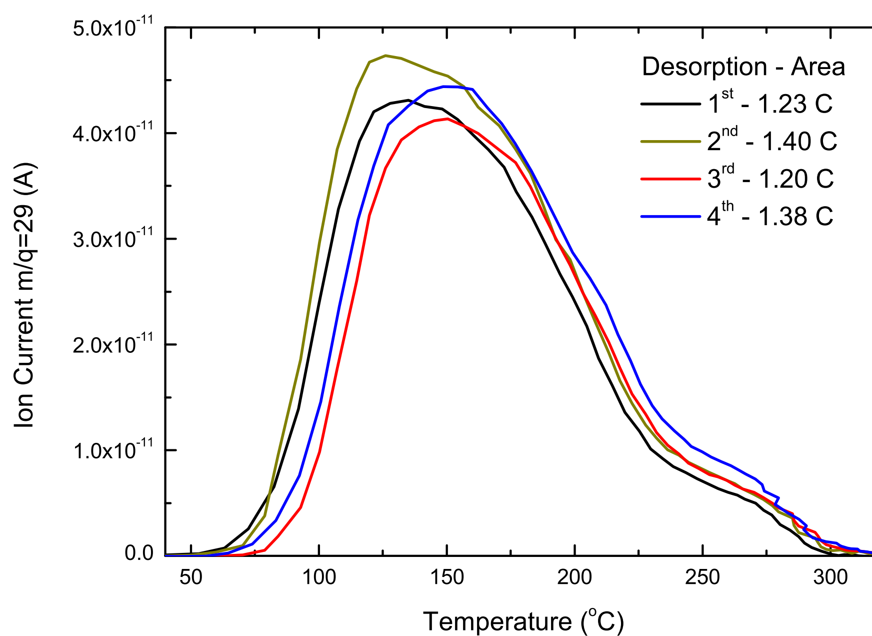

Figure 9.7: Four consecutive thermal CO desorption experiments. A measure of the total amount of desorbed CO is obtained by integrating the ion current as a function time. This area is shown for each of the experiments in the legend.

9.5 Detection Limit

From the CO thermal desorption measurements presented in the last section we can now estimate the detection limit of the mass spectrometer setup combined with our MIS hot electron device and the geometry of our setup in general.

Furthermore we can give a rough estimate of the desorption rate of CO from our devices using various data from the work presented throughout this thesis.

The detection limit of our detection system is obtained using the peak area obtained from the CO desorption experiments presented in the last section.

There are basically two possible experimental detection modes, which could be used to detect hot electron activated processes, these are online and batch mode. With an online detection mode the products are detected while the experiment is running and the production rate must be large enough to be told apart from the background. In the batch detection mode the experiment is left running for an extended period of time before the products or, in the case of CO desorption, the remaining reactants are detected.

The detection limit of the mass spectrometer setup is determined as:

$$\Gamma_{Lim} = \frac{\theta_{CO} \cdot \rho_{Pt} \cdot A_{MIS}}{A_{TPD}} \cdot I_{Min} \tag{9.7}$$

where A_{TPD} is the area of the TPD peak of CO obtained experimentally, θ_{CO} is the expected coverage of CO on polycrystaline Pt at the conditions prior to the TPD, I_{Min} is the smallest change in current which can be distinguished from the noise in the ion current, A_{MIS} is the active emission area of the device, and ρ_{Pt} is the density of Pt atoms in the surface of the MIS electron emitter.

The expected coverage of CO on polycrystaline Pt at room temperature under UHV (θ_{CO}) is 0.5 ML [78]. The active area of the devices A_{MIS} is 1 cm^2. The density of Pt atoms in the surface ρ_{Pt} is 1.5×10^{15} cm^{-2}[85], and the step in ion current which can be detected is estimated to be 10^{-14} A [4].

This gives a detection limit of the online experiment of:

[4]Based on an experiment where the signal of 29 m/q was followed for 1 h. The signal was measured for 10 s in one channel and 10 s in another channel repeatedly, simulating an online experiment with the MIS hot electron emitter turned on for 10 s then off for 10 s. The standard deviation of the difference between the channels was 5×10^{-15} A. Two times the standard deviation, set as the detection limit, yield 10^{-14} A.

$$\Gamma_{Online} = \frac{0.5 \cdot 1.5 \times 10^{15}\ \text{cm}^{-2} \cdot 1\ \text{cm}^2}{1.3 \times 10^{-9}\ \text{C}} \cdot 10^{-14}\ \text{A} = 6 \times 10^9\ \text{s}^{-1} \tag{9.8}$$

In the case of a batch experiment where the experiment was running for ten hours a positive result can be defined as an experiment that yield a value that falls two standard deviations off the mean value of the experiments presented in Fig. 9.7, assuming no desorption from the surface by thermal processes. The standard deviation for the areas from measurements is 10^{-10} C. In this case the detection limit becomes:

$$\Gamma_{Batch} = \frac{0.5 \cdot 1.5 \times 10^{15}\ \text{cm}^{-2} \cdot 1\ \text{cm}^2 \cdot 2 \cdot 10^{-10}\ \text{C}}{1.3 \times 10^{-9}\ \text{C} \cdot 10\ \text{h}} = 3 \times 10^9\ \text{s}^{-1} \tag{9.9}$$

9.6 Hot Electron Induced Desorption Rates

With estimates of the detection limits, it is interesting to estimate the desorption rate from the MIS hot electron emitter. The desorption rate of CO induced by hot electrons can be described using the simple product of several parameters:

$$k_{des} = \frac{I_{Hot}}{q} \cdot P_{\text{des}} \cdot \theta_{\text{CO}} \cdot \eta \tag{9.10}$$

where I_{Hot} is the current of hot electrons tunneling through the oxide into the metal layer, P_{des} is the probability for a CO molecule hit by a hot electron with the right energy to desorb, and η is the efficiency, with which an electron injected into the metal layer will emanate at the surface of the metal layer as a ballistic electron, see Sec. 7.3.

In order to get some desorption rates to compare to our detection limit three sets of numbers are used representing three different situations.

The desorption probability per electron scattering event is obtained from Sec. 2.2, presenting theoretical work on the desorption probability, to be 10^{-5} for CO on Pt(111).

1. **The Current Situation** In this case the desorption rate is estimated using numbers that have been achieved experimentally in the work presented in this thesis. The resonance is being activated by ballistic electrons with an energy of 4.5 eV. The typical current of the MIS electron emitter at 4.5 V is 1 mA. The efficiency for an electron to transverse the metal layer (consisting of 20 nm Pt) without loosing significant energy is known from Fig. 7.6 to be $\sim 10^{-6}$. This yield a desorption rate of: 2×10^4 s^{-1}.

2. **Optimistic Estimate** Decreasing the Pt metal layer thickness to 5 nm might increase the efficiency by a factor of ten to 10^{-5}. The oxide layer thickness is decreased so the current at 4.5 V is 100 mA. These numbers result in a desorption rate of 2×10^{7} s^{-1}.

3. **Indirect Activation** Indirectly activating the CO resonance at 4.5 eV, by driving the MIS electron emitter at eg. 6 V relying on inelastically scattered electrons to drive the desorption process could in theory circumvent the efficiency factor by creating a close to equal amount of secondary electrons in the resonance region as ballistic electrons were injected into the metal layer. This would then yield a desorption rate of 2×10^{10} s^{-1} for a current of 1 mA.

The three examples for the desorption rate are shown along with the detection limit in Fig.9.8. For a binary experiment the desorption rate must be above the detection limit, but for more quantitative experiments the desorption rate should be at least an order of magnitude above the detection rate.

The numbers calculated for these three situations are of course subject to a large uncertainty and could easily vary several orders of magnitude. The important message from these calculations are however quite clear. Even with a desorption probability of one per electron the desorption rate would be below the detection limit for the current system. This underlines the necessity of improving the sensitivity of the current mass spectrometer detection system, which should be possible. This could be done by moving the mass spectrometer closer to the device surface and by removing the sniffer. Of course also completely different techniques for detection could be considered.

Another interesting point is that it seems like the detection limit of the batch and online experiments are comparable for the CO experiment. Our initial expectations were that the detection limit in for the batch experiment would be significantly better than that for the online experiment, but in the relatively poor reproducibility of the batch experiments, the CO desorption measurements, eat up the advantage of the integration over time. This is especially the case when also thermal desorption at room temperature is taken into account.

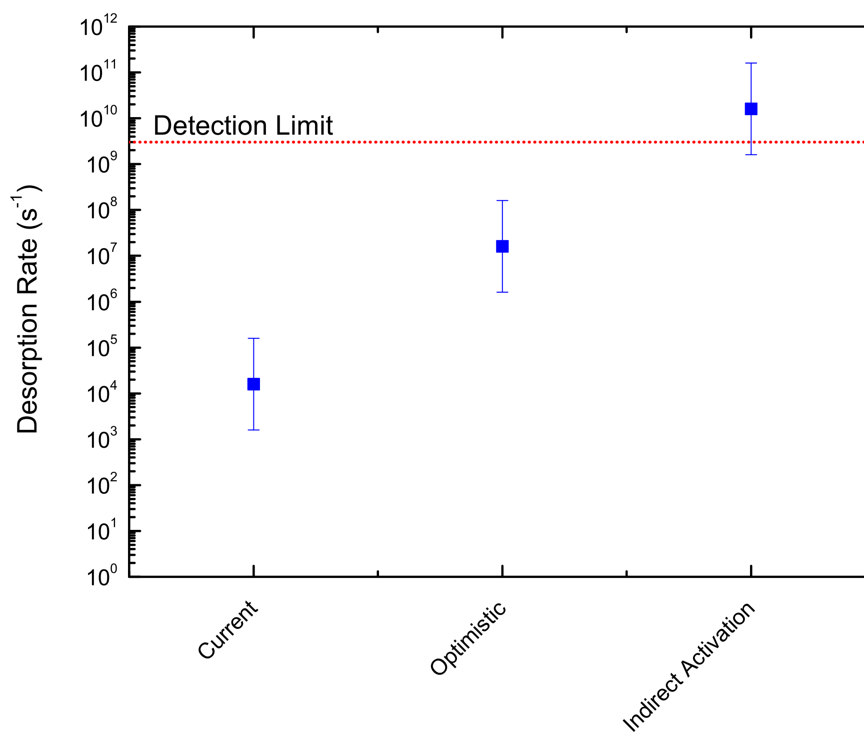

Figure 9.8: The desorption rates shown for the three situations described in the text along with the detection limit of the current mass spectrometer setup. It is seen that there is a large gap between the detection limit and the estimated desorption rates. However, these numbers have a high degree of uncertainty.

Chapter 10

Conclusion

In this thesis MIS based hot electron emitter devices have been modeled, designed, fabricated and characterized with the motivation of using such devices for enhancing the reactivity of metal surfaces using hot electrons. During the investigation of the MIS hot electron emitters the following conclusions and achievements were reached:

- An implementation of a MIS structure was chosen as the source for hot electrons for hot electron chemistry based on the proposal by J. W. Gadzuk of a MIM based device for hot electron chemistry on surfaces [1, 2, 3].

- A theoretical framework for the MIS structure from the point of view of hot electron generation was presented. Self-consistent modeling of Poisson's equation was carried out.

- A device was designed implementing a MIS structure hot electron emitter along with a wafer layout and process sequence to fabricate the devices. The MIS hot electron emitters were produced in cleanroom conditions with variations in metal layer type and thickness.

- Simulations describing the consequences of the thickness and variations of the tunnel barrier of the fabricated MIS hot electron emitters were presented. The results underlined the critical importance of achieving as low a roughness as possible of the tunnel barrier in order to distribute emission evenly across the active area of the MIS hot electron emitters.

- CV characteristics showed insulator thickness close to the expected value of 50 Å, but with thicknesses varying 5 Å across a wafer, and up to 15 Å from wafer to wafer in the same batch.

- IV characteristics indicated tunneling as the main mechanism for electron conduction through the SiO_2 insulator layer, especially when presented in Fowler plots. The apparent thicknesses extracted from the slope of the Fowler plots showed systematic and linear variation with the thicknesses extracted from CV measurements. As predicted from the simulations the extracted thicknesses from the IV measurements seemed lower than those from CV measurements indicating some degree of SiO_2 roughness.

- A UHV setup was developed to facilitate experiments with electron emission, heating and temperature monitoring, and surface chemistry.

- Electron emission has been realized from the MIS hot electron emitters with Ti/Au gate metal layers. The total emission from the devices under vacuum has been characterized using a biased Cu plate as collector. The emission at low bias voltages ($<$4.8 V) was seen to be varying over time and probably related to defects in the insulator. The emission for higher voltages ($>$5 V) was however quite stable and related to tunneling electrons.

- The workfunction of the MIS hot electron emitters was lowered using Cs to below 2 eV and electron emission was observed for bias voltages as low as 2 eV. Cs changed the IV characteristics of the devices, increasing the tunnel current by orders of magnitude. Furthermore Cs had a deteriorating effect on the reliability of the SiO_2 tunnel barrier, causing the devices to fail more rapidly. The reason for the devices to fail more rapidly is believed to relate to Cs diffusing from the metal surface to the insulator surface thereby lowering the tunnel barrier and increasing the tunnel current. The highest observed emission efficiency was 8% for a cesiated surface at a bias voltage of 3 V.

- The mean free path of electrons with a kinetic energy of 5 eV has been extracted by measuring the emission efficiency as a function of the thickness of the Au metal layer. The mean free path obtained was 52 Å. This value is in excellent agreement with both theoretical predictions [77] and experimental data [76] in the literature.

- The influence of the Ti wetting layer on the emission efficiency was investigated and it was found that a 1 nm Ti layer reduces the efficiency of emission by approximately one order of magnitude. This effect was explained as the workfunction difference between Au and Ti leading to a strong scattering potential at the interface of Ti and Au.

- Sputtering the MIS hot electron emitters with 500 eV O^+ ions increased the emission efficiency by two orders of magnitude due to roughening of the metal layer, creating areas with lower thickness of Au.
- Electron emission under ambient pressure conditions was realized across a 0.1 mm gap from emitter to collector, proving the ability of the MIS electron emitter to operate under high gas pressures. This ability was further put to test in a minireactor, where the electron emission was characterized as a function of Ar pressure. It was seen that the emission dropped an order of magnitude from vacuum conditions to 2 bar of Ar. The emission current decreased exponentially with pressure.
- The energy dispersion of the emitted electrons was investigated using a modified HSA setup with a very low pass energy (1 eV) to suppress signal and achieve high resolution. The energy distribution was seen to evolve from being cut-off by the workfuntion of the surface of the emitter to a single peak moving up in kinetic energy as a function of bias voltage. The high energy flank and peak position moves proportional in energy to the increase in applied bias voltage which indicates that the observed electrons are ballistic electrons from around the Fermi level of Si.
- It was demonstrated that a 20 nm Pt film can be used as a template for hot electron chemistry on the MIS hot electron emitter. Such a Pt film can be heated by a driving direct current of 0.3 A between the two front contacts of the MIS hot electron emitter. Furthermore a good measure of the temperature is obtained using the temperature dependence of the resistivity of the Pt film as a thermometer. The resistance of the Pt film was calibrated using a thermocouple and the calibration was seen to be consistent with the thickness of the Pt film.
- The Pt film was cleaned in-situ by heating the film to approximately 400°C in an O_2 background pressure of 3×10^{-7} mbar. After cleaning, the Pt film was able to catalyze CO oxidation.
- CO thermal desorption experiments were carried out and the desorption profile was in good agreement to expectations and results from literature on Pt(111) and Pt(poly). CO was desorbing in a broad peak from 60°C to 225°C with a shoulder extending to 300°C . The main peak was attributed to terrace sites while the high temperature shoulder desorption was assigned to under coordinated sites such as kinks and steps. The reproducibility obtained was close to 7% in area, which is not too impressive and should be improved upon.

- From the CO desorption experiments the detection limit of the mass spectrometer setup was estimated using basic assumptions for coverage and adsorption site surface density to be 6×10^9 s^{-1} for online experiments and 3×10^9 s^{-1} for batch experiments.

- The desorption rate induced by hot electrons on the MIS hot electron emitters was estimated for three cases: Current ($\Gamma = 2 \times 10^4$ s^{-1}), optimistic (2×10^7 s^{-1}), and indirect activation (2×10^{10} s^{-1}). Only the estimate of the desorption rate of indirect activation is above the estimated detection limit.

Altogether a large base of knowledge have been gathered on the various aspects of the MIS hot electron emitter and the application of this for the overall goal of experimental investigation of surface chemistry enabled by hot electrons. This information is not only applicable for hot electron chemistry, but for many interesting technological applications where a low voltage cold cathode electron emitter is desirable.

Appendix A

Symbols

A Area

α Thermal Coefficient of Resistance

C Capacitance

ε Electric field

ε_S Surface electric field

E_A Acceptor activation energy

E_C Energy level of Conduction Band Edge

E_D Donor activation energy

E_F Fermi level

E_F, i The intrinsic Fermi level

E_g Energy band gap

E_V Energy level of Valence Band Edge

E_{Vac} Energy of the Vacuum level

E_x Transverse Energy

E_p Longitudinal Energy

η Electron Emission Efficiency

ϵ_0 Permittivity of vacuum

ϵ_r Relative permittivity

$\mathcal{F}$ Fermi Integral

f_A Acceptor distribution function

f_D Donor distribution function

f_{fd} Fermi-Dirac distribution function

G Gain

Γ Detection limit

g_C Density of states in the conduction band

g_V Density of states in the valence band

h Planck's Constant

$\hbar$ Modified Planck's Constant $h/2\pi$

I Current

J Current Density

k_B Boltzmann's constant

k_{des} Desorption rate

L Length

ℓ Metal layer thickness

λ Mean free electron path

m^* Effective Electron mass

m_C^* Effective electron mass in the conduction band

m_V^* Effective hole mass in the valence band

N_A Concentration of acceptors

N_A^- Concentration of ionized acceptors

N_C Effective Density of States in the conduction band

N_D Concentration of donors

N_D^+ Concentration of ionized donors

N_C Effective Density of States in the valence band

$N(E_x)$ Supply function

n Concentration of electrons

n_0 Equilibrium concentration of electrons

ρ Charge density

P_{des} Desorption probability

p Concentration of holes

p_0 Equilibrium concentration of holes

Φ Work function

Φ_B Tunnel barrier height

Q Charge

q The elementary charge

R Resistance

R_C Contact resistance

R_0 Resistance at 0°C

Ψ Wavefunction

ψ_S Surface Potential of the semiconductor

$sigma$ Standard Deviation

T Temperature

Θ Coverage

$T(E_x)$ Transmission Coefficient

χ Electron Affinity

v_k k$^{\text{th}}$ eigenvector

$V_{\mathbf{Bias}}$ Bias Voltage

V_{FB} Flat band voltage

V_I Voltage across insulator

$V(x)$ Potential

V_{im} Image charge potential

W Width

X_I Insulator thickness

x_C Classical Turning Point

Appendix B

Abbreviations

AFM Atomic Force Microscopy

ASF Atomic Sensitivity Factor

CV Capacitance Voltage. As in capacitance-voltage characteristics.

DFT Density Functional Theory

DIET Desorption Induced by Electronic Transitions

DIMET Desorption Induced by Multiple Electronic Transitions

ΔSCF-DFT Delta Self-Consistent Field DFT

ESD Electron Stimulated Desorption

FWHM Full Width at Half Maximum

HEEL Hot Electron Emission Lithography

HSA HemiSpherical Analyzer

ISS Ion Scattering Spectroscopy

IV Current Voltage. As in current-voltage characteristics.

MCP Multi Channel Plate

MEMS Micro-Electro-Mechanical-Systems

MIM Metal Insulator Metal

MIS Metal Insulator Semiconductor

ML Mono layer

MOS Metal Oxide Semiconductor

PES Potential Energy Surface

PVD Physical Vapor Deposition

QCM Quartz Crystal Microbalance

STM Scanning Tunneling Microscopy

TCR Thermal Coefficient of Resistance

UHV Ultra High Vacuum

XPS X-ray Photoelectron Spectroscopy

Appendix C

Numerical Implementation

The numerical self-consistent solution to Poisson's equation was implemented in Mathworks MATLAB.

First of all the equilibrium Fermi level was obtained using the solution described in Sec. 3.1.4 for the donor concentration selected.

The solution of Eq. 3.39 and 3.40 was implemented on the same equidistant 1-D grid with an element spacing of 1 Å. 5 nm oxide and 30 nm of Si was used as the geometry for solving the system. In the solution of the Schrödinger equation the oxide was modeled as an infinitely high barrier to avoid bound eigenstates in the tilted conduction band of the oxide at high voltages.

The charge density as a function the spatial coordinate was obtained using a guess potential distribution to generate the charge densities of free electrons, free holes, ionized donors and acceptors. The density of electrons and holes in bound states was obtained by solving the discretized Schrödinger equation (Eq. 3.40) using the MATLAB `eigs` eigenvalue solver.

The iteration procedure and self-consistency loop was provided by the MATLAB `fsolve` nonlinear solver. A `TolFun` value or maximum value of Eq. 3.39 of 10^{-12} was used as the self-consistency criteria in all calculations presented in this thesis.

Appendix D

Process as implemented in the Danchip Cleanroom

In this appendix information related to the specifics of the implementation of the Hot Electron Emitter process in the Danchip Cleanroom at DTU is given. The purpose is to convey the tricks-of-the-trade with specific machinery available in the Danchip cleanroom facility.

The item numbers of this appendix refer to the process steps as laid out in section 4.2.

1 Wafer Selection Wafers from the batches ON132, ON188, and ON200 have been successfully used as substrates for the Hot Electron Emitters.

2 Formation of Thick Oxide The wet oxidation has been performed in the phosphor drive-in furnace using the WET1000 recipe with 180 min oxidation time and 20 min N_2 anneal time. The FilmTek is used for measuring the oxide thickness.

3 Etch Mask Definition Mask: HotElectronVer2_Field. Both the EV or KS-aligner can be used. Take care to align the mask to the wafer flats, to avoid problems with the shadow mask alignment when depositing the metal gate layer.

4 Back Etching of Active Emitter Areas Either use the bHF bath in the photolithography room or the bHF bath with wetting agent and elevator in the new part of the cleanroom.

5 Tunnel Oxide Formation Use Gate-Oxide Furnace with DRY800 recipe 40 min oxidation time and 20 min anneal in N_2 . Place two new wafers in front of and behind the device wafers in the boat. Include the four

test wafers in the RCA clean to make sure they are clean and without any oxide. Measure the film thickness using the Ellipsometer.

6 Wafer Backside Metallization Either use the Leybold, Wordentec or Alcatel PVD system. Use a drop of HF acid to remove any oxide formed on the backside of the wafers just prior to the PVD process.

7 Gate Metal Deposition Use Alcatel PVD system. For thin layers the evaporation rate can be adjusted to eg. 1 Å s^{-1}.

8 Optionally: Wafer Dicing Use diamond cutter tool in the service room between the lock and the photolithography room.

Appendix E

Calibration of Metal Layer Thickness

In Fig. E.1 a calibration between the selected or nominal thickness of an Au layer and the value measured by AFM.

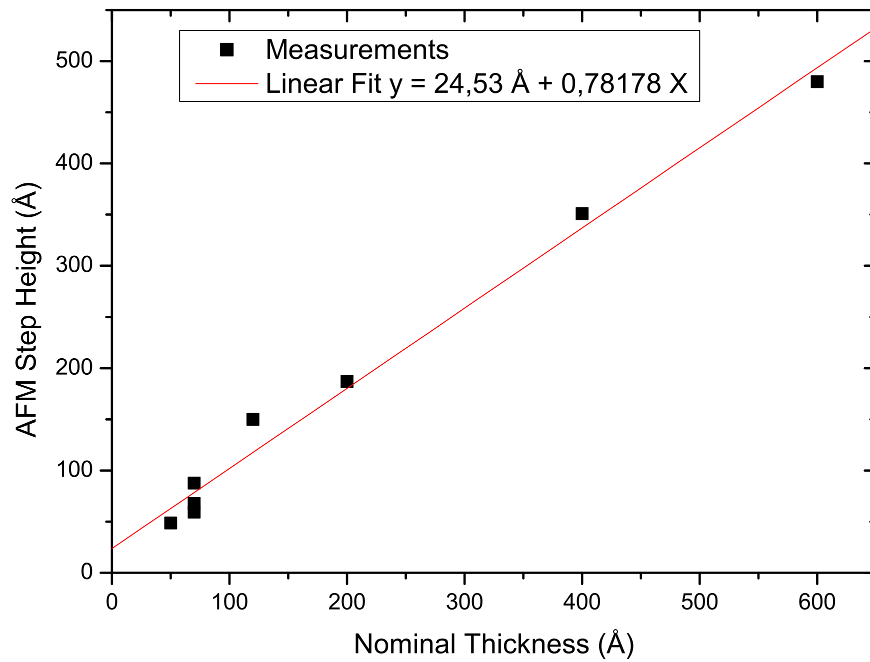

Figure E.1: AFM step height versus nominal Au layer thickness. The offset can partly be explained by the 1 nm Ti wetting layer, while the slope not being 1 is explained by an error in the calibration of the Quartz-Crystal-Micro Balance (QCM) which was used to monitor the thickness during deposition.

Bibliography

[1] J. W. Gadzuk. Inelastic resonance scattering, tunneling and desorption. *Physical Review B*, 44(24):13466–13477, 1991.

[2] J W Gadzuk and C W Clark. Resonance enhanced electron stimulated desorption. *Journal of Chemical Physics*, 91(5):3174–3181, 1989.

[3] J. W. Gadzuk. Role of secondary electrons in hot-electron femtochemistry at surfaces using tunnel junctions. volume 15, pages 1520–1525. AVS, 1997.

[4] P. Sabatier. La catalyse en chimie organique. *Bérange, Paris*, 1920.

[5] M. P. Ray, R. E. Lake, L. B. Thomsen, G. Nielsen, O. Hansen, I. Chorkendorff, and C. E. Sosolik. Surface-assisted kinetically induced hot carrier production in mos devices via slow ion bombardment. *In preparation*, 2009.

[6] S. Meyer, D. Diesing, and A. Wucher. Kinetic electron excitation in atomic collision cascades. *Phys. Rev. Lett.*, 93(13):137601, Sep 2004.

[7] Beate Mildner, Eckart Hasselbrink, and Detlef Diesing. Electronic excitations induced by surface reactions of h and d on gold. *Chemical Physics Letters*, 432(1-3):133 – 138, 2006.

[8] X. Liu, B. Roldan Cuenya, and E. W. McFarland. A mis device structure for detection of chemically induced charge carriers. *Sensors and Actuators B: Chemical*, 99(2-3):556 – 561, 2004.

[9] M. Born and R. Oppenheimer. Quantum theory of the molecules. *Annalen der Physik*, 84:457–84, 1927.

[10] B. Gergen, H. Nienhaus, W. Weinberg, and E. McFarland. Chemically induced electronic excitations at metal surfaces. *Science*, 294(5551):2521–2523, 2001.

[11] H. Nienhaus, B. Gergen, W. Weinberg, and E. McFarland. Detection of chemically induced hot charge carriers with ultrathin metal film schottky contacts. *Surface Science*, 514:172–181, 2002.

[12] H. Brenten, H. Müller, W. Maus-Friedrichs, S. Dieckhoff, and V. Kemptera. Exo-electron emission during the oxidation of alkalated w(110) surfaces. *Surface Science*, 262:151–158, 1992.

[13] S. Glass and H. Nienhaus. Continuous monitoring of mg oxidation by internal exoemission. *Physical Review Letters*, 93(16):168302, 2004.

[14] A. L. Linsebigler, G. Lu, and J. T. Yates Jr. Photocatalysis on tio_2 surfaces: Principles, mechanisms, and selected results. *Chemical Reviews*, 95:735–756, 1995.

[15] R. D. Ramsier and J. T. Yates. Electron-stimulated desorption: Principles and applications. *Surface Science Reports*, 12(6-8):246 – 378, 1991.

[16] J. A. Prybyla, T. F. Heinz, J. A. Misewich, M. M. T. Loy, and J. H. Glownia. Desorption induced by femtosecond laser pulses. *Phys. Rev. Lett.*, 64(13):1537–1540, 1990.

[17] F.-J. Kao, D. G. Busch, D. Cohen, D. Gomes da Costa, and W. Ho. Femtosecond laser desorption of molecularly adsorbed oxygen from pt(111). *Phys. Rev. Lett.*, 71(13):2094–2097, Sep 1993.

[18] J.W. Gadzuk, L.J. Richter, S.A. Buntin, D.S. King, and R.R. Cavanagh. Laser-excited hot-electron induced desorption: A theoretical model applied to no/pt(111). *Surface Science*, 235(2-3):317 – 333, 1990.

[19] S. Alavi and T. Seideman. Reaction induced by a scanning tunneling microscope: Theory and application. *The Journal of Chemical Physics*, 115(4):1882–1890, 2001.

[20] N Lorente, R Rurali, and H Tang. Single-molecule manipulation and chemistry with the stm. *Journal of Physics: Condensed Matter*, 17(13):S1049–S1074, 2005.

[21] J. Gavnholt, T. Olsen, M. Engelund, and J. Schiøtz. Delta self-consistent field method to obtain potential energy surfaces of excited molecules on surfaces. *Physical Review B*, 78(7):075441, 2008.

[22] J. W. Gadzuk. Resonance-assisted, hot-electron-induced desorption. *Surface Science*, 1995.

[23] D. Diesing, A. W. Hassel, and M. M. Lohrengel. Aluminium oxide tunnel junctions: influence of preparation technique, sample geometry and oxide thickness. *Thin Solid Films*, 342(1-2):282 – 290, 1999.

[24] D. Diesing, G. Kritzler, M. Stermann, D. Nolting, and A. Otto. Metal/insulator/metal junctions for electrochemical surface science. *Journal of Solid State Electrochemistry*, 7:389–415, 2003.

[25] T Wadayama, A Kojim, and A Hatta. Bias-voltage-induced decomposition of 2-methyl-1,4-naphthoquinone on Ag/AlOx/Al tunnel junction. *Applied Physics A-Materials Science & Processing*, 79(8):1891–1894, DEC 2004.

[26] T. Wadayama and M. Yokawa. Hot-electron assisted reaction of p-nitrobenzoic acid adsorbed on metal-insulator-metal tunnel junction's electrode surface. *Chemical Physics Letters*, 428(4-6):348–351, SEP 20 2006.

[27] T. E. Madey. History of desorption induced by electronic transitions. *Surface Science*, 299-300:824 – 836, 1994.

[28] J. A. Misewich, T. F. Heinz, and D. M. Newns. Desorption induced by multiple electronic transitions. *Phys. Rev. Lett.*, 68(25):3737–3740, Jun 1992.

[29] W. Ho. Reactions at metal surfaces induced by femtosecond lasers, tunneling electrons, and heating. *The Journal of Physical Chemistry*, 100(31):13050–13060, 1996.

[30] P. Hohenberg and W. Kohn. Inhomogeneous electron gas. *Phys. Rev.*, 136(3B):B864–B871, Nov 1964.

[31] T. Olsen, J. Gavnholt, and J. Schiøtz. Hot-electron-mediated desorption rates calculated from excited-state potential energy surfaces. *Physical Review B (Condensed Matter and Materials Physics)*, 79(3):035403, 2009.

[32] F. Abild-Pedersen and M.P. Andersson. Co adsorption energies on metals with correction for high coordination adsorption sites - a density functional study. *Surface Science*, 601(7):1747 – 1753, 2007.

[33] B. v. Zeghbroeck. *Principles of Semiconductor Devices.* Electrical and Computer Engineering Department, University of Colorado, 2004.

[34] D. K. Schroder. *Semiconductor Material and Device Characterization.* IEEE Press, 2006.

[35] R. H. Fowler and L. W. Nordheim. Electron emission in intense electric fields. *Proc. Royal Soc. London A*, 119:173–181, 1928.

[36] C. B. Duke. *Tunneling in Solids.* Academic Press, 1969.

[37] G. Wentzel. A generalisation of the quantum constraints for the purposes of the wave mechanics. *Zeitschrift für Physik*, 38:518–529, 1926.

[38] H. A. Kramers. Wave mechanics and half-integral quantisation. *Zeitschrift für Physik*, 39:828–840, 1926.

[39] L. Brillouin. The ondulatory mechanics of schrodinger; a general method of resolution by successive approximations. *Comtes Rendus Hebdomadaitres des Seances De L Academite Des Sciences*, 183:24–27, 1926.

[40] E. Schroedinger. The current situation in quantum mechanics. *Naturwissenschaften*, 23:844–849, 1935.

[41] E. Schroedinger. The present situation in quantum mechanics. *Naturwissenschaften*, 23:823–828, 1935.

[42] E. Schroedinger. The current situation in quantum mechanics. *Naturwissenschaften*, 23:807–812, 1935.

[43] A. Schenk and G. Heiser. Modeling and simulation of tunneling through ultra-thin gate dielectrics. *Journal of Applied Physics*, 81(12):7900–7908, 1997.

[44] N. Yang, W. K. Henson, J. R. Hauser, and J. J. Wortman. Modeling study of ultrathin gate oxides using direct tunneling current and capacitance voltage measurements in mos devices. *IEEE Transactions on Electron Devices*, 46(7):1464–1471, 1999.

[45] Z. A. Weinberg. On tunneling in metal-oxide-silicon structures. *Journal of Applied Physics*, 53(7):5052–5056, 1982.

[46] S. Subramanian. A self-consistent solution of one-dimensional schrodinger-poisson equations by newton-raphson iteration technique. *Proc. 3rd Int. Workshop on Computational Electronics*, 1994.

[47] M. A. Green. Intrinsic concentration, effective densities of states, and effective mass in silicon. *Journal of applied physics*, 67(6):2944–54, 1989.

[48] L. F. Register, E. Rosenbaum, and K. Yang. Analytic model for direct tunneling current in polycrystalline silicon-gate metal–oxide–semiconductor devices. *Applied Physics Letters*, 74(3):457–459, 1999.

[49] W. Kern. *Handbook of Semiconductor Wafer Cleaning Technology - Science, Technology, and Applications*. William Andrew Publishing/Noyes, 1993.

[50] C. P. Ho and J. D. Plummer. Si/sio_2 interface oxidation kinetics: A physical model for the influence of high substrate doping levels. 1. theory. *Journal of the Electrochemical Society*, 126:1516–1522, 1979.

[51] C. P. Ho and J. D. Plummer. Si/sio_2 interface oxidation kinetics: A physical model for the influence of high substrate doping levels. 2. comparison with experiment and discussion. *Journal of the Electrochemical Society*, 126:1523–1530, 1979.

[52] S. Lombardo, J. H. Stathis, B. P. Linder, K. Leong Pey, F. Palumbo, and C. H. Tung. Dielectric breakdown mechanisms in gate oxides. *Journal of Applied Physics*, 98(12):121301, 2005.

[53] B. P. Linder and J. H. Stathis. Statistics of progressive breakdown in ultra-thin oxides. *Microelectronic Engineering*, 72(1-4):24 – 28, 2004. Proceedings of the 13th Biennial Conference on Insulating Films on Semiconductors.

[54] M. Lenzlinger and E. H. Snow. Fowler-nordheim tunneling into thermally grown sio_2. *Journal of Applied Physics*, 40:278–283, 1969.

[55] Z. Weinberg. On tunneling in metal-oxide-structures. *Journal of Applied Physics*, 53:5052–5056, 1982.

[56] C. Hendriksen and O. Hansen. Comparison of thickness measured by afm and ellipsommetry. Private communications.

[57] E. Y. Wu and J. Suñé. Power-law voltage acceleration: A key element for ultra-thin gate oxide reliability. *Microelectronics and Reliability*, 45(12):1809 – 1834, 2005.

[58] S. D. Brorson, D. J. DiMaria, M. V. Fischetti, F. L. Pesavento, P. M. Solomon, and D. W. Wong. Direct measurement of the energy distribution of hot electrons in silicon dioxide. *Journal of Applied Physics*, 58(3):1302–1313, 1985.

[59] D. J. DiMaria, M. V. Fischetti, J. Batey, L. Dori, E. Tierney, and J. Stasiak. Direct observation of ballistic electrons in silicon dioxide. *Physical Review Letters*, 57(25):3213–3217, 1986.

[60] J. Cohen. Tunnel emission into vacuum. *Journal of Applied Physics*, 33(6):1999–2000, 1962.

[61] J. Cohen. Tunnel emission into vacuum ii. *Applied Physics Letters*, 1(3):61–62, 1962.

[62] C. A. Mead. Operation of tunnel-emitter devices. *Journal of Applied Physics*, 32(4):646–652, 1961.

[63] K. Yokoo, H. Tanaka, S. Sato, J. Murota, and S. Ono. Emission characteristics of metal-oxide-semiconductor electron tunneling cathode. *Journal of Vacuum Science and Technology B*, 11(2):429–432, 1993.

[64] K.H.-J. Fitting, T. Hingst, and E. Schreiber. Breakdown and high-energy electron vacuum emission of mis-structures. *Journal of Physics D: Applied Physics*, 32:1963–1970, 1999.

[65] H. Mimura, Y. Neo, H. Shimawaki, T. Matsumoto, and K. Yokoo. Emission characteristics and application of semiconductor field emitters. *Applied Surface Science*, 144:498–503, 2005.

[66] N. S. Xu and S. E. Huq. Novel cold cathode materials and applications. *Materials Science and Engineering R*, 48:47–189, 2005.

[67] W. B. Nottingham. Thermionic emission from tungsten and thoriated tungsten filaments. *Physical Review*, 49:78–97, 1936.

[68] L. B. Thomsen, G. Nielsen, S. B. Vendelbo, M. Johansson, O. Hansen, and I. Chorkendorff. Electron emission from ultra-large area mos electron emitters. *Accepted, Journal of Vacuum Science and Technology B*, 2009.

[69] M. Poppeller, E. Cartier, and R. M. Tromp. *Microelectronic Engineering*, 46:183–186, 1999.

[70] G. Nielsen, L. B. Thomsen, M. Johansson, O. Hansen, and I. Chorkendorff. Electron emission from mos electron emitters with clean and cesium covered gold surface. *Submitted to Applied Surface Science*, 2009.

[71] H. L. Skriver and N. M. Rosengaard. Surface energy and work function of elemental metals. *Physical Review B*, 46(11):7157–7168, 1992.

[72] H. Mimura, Y. Neo, H. Shimawaki, Y. Abe, K. Tahara, and K. Yokoo. Improvement of the emission current from a cesiated metal-oxide-semiconductor cathode. *Applied Physics Letters*, 88, 2006.

[73] J. Drucker and P. K. Hansma. Emission of energetic electrons from tunnel junctions. *Applied Physics Letters*, 30(8), 1984.

[74] H. Mimura, K. Miyajima, and K. Yokoo. Electron emission from porous planar emitters. *Journal of Vacuum Science and Technology B*, 21(4), 2003.

[75] J. A. Rodriguez, J. Hrbek, Y.-W. Yang, M. Kuhn, and T. K. Sham. Photoemission and thermal desorption studies of cs-au and li-au films on ru(oo1). *Surface Science*, 293:260–274, 1993.

[76] W. F. Krolikowski and W. E. Spicer. Photoemission studies of the noble metals. ii. gold. *Physical Review B*, 1(2):478–487, 1970.

[77] H. Kanter. Slow-electron mean free paths in aluminum, silver, and gold. *Physical Review B*, 1(2):522–536, 1970.

[78] G Ertl, M Neumann, and Km Streit. Chemisorption Of Co On Pt(111) Surface. *Surface Science*, 64(2):393–410, 1977.

[79] JK Bohlke, JR de Laeter, P De Bievre, H Hidaka, HS Peiser, KJR Rosman, and PDP Taylor. Isotopic compositions of the elements, 2001. *Journal Of Physical And Chemical Reference Data*, 34(1):57–67, 2005.

[80] L. Michalski, K. Eckersdorf, J. Kucharski, and J. McGhee. *Temperature Measurement*. John Wiley and Sons, Ltd, 2002.

[81] P. R. N. Childs, J. R. Greenwood, and C. A. Long. Review of temperature measurement. *Review of Scientific Instruments*, 71(8):2959–2978, 2000.

[82] I. Chorkendorff. Experimental surface physics. *Lecture notes - Part A*, 2004.

[83] G. Ertl, P. R. Norton, and J. Rüstig. Kinetic oscillations in the platinum-catalyzed oxidation of co. *Phys. Rev. Lett.*, 49(2):177–180, 1982.

[84] A. K. Santra and D. W. Goodman. Catalytic oxidation of co by platinum group metals: from ultrahigh vacuum to elevated pressures. *Electrochimica Acta*, 47(22-23):3595 – 3609, 2002.

[85] R.W McCabe and L.D Schmidt. Binding states of co on single crystal planes of pt. *Surface Science*, 66(1):101 – 124, 1977.

[86] P. J. Feibelman, B. Hammer, J. K. Norskov, F. Wagner, M. Scheffler, R. Stumpf, R. Watwe, and J. Dumesic. The co/pt(111) puzzle. *The Journal of Physical Chemistry B*, 105(18):4018–4025, 2001.

Appendix F

List of Publications

Paper 1: Ultralarge area MOS tunnel devices for electron emission
Lasse B. Thomsen, Gunver Nielsen, Søren B. Vendelbo, Martin Johansson, Ole Hansen, and Ib Chorkendorff,
Physical Review B, 2007

Paper 2: Electron emission from ultralarge area metal-oxide-semiconductor electron emitters
Lasse B. Thomsen, Gunver Nielsen, Søren B. Vendelbo, Martin Johansson, Ole Hansen, and Ib Chorkendorff,
accepted by Journal of Vacuum Science and Technology B, 2009

Paper 3: Electron emission from MOS electron emitters with clean and cesium covered gold surface
Gunver Nielsen, Lasse B. Thomsen, Martin Johansson, Ole Hansen, and Ib Chorkendorff,
submitted to Applied Surface Science, 2009

Ultralarge area MOS tunnel devices for electron emission

Lasse B. Thomsen,[1] Gunver Nielsen,[1] Søren B. Vendelbo,[1] Martin Johansson,[1] Ole Hansen,[1,2] and Ib Chorkendorff[1,*]
[1]*CINF—Center for Individual Nanoparticle Functionality, Department of Physics, Nano•DTU, Technical University of Denmark, DK-2800 Kongens Lyngby, Denmark*
[2]*MIC—Department of Micro and Nanotechnology, Oersteds Plads Building 345E, Nano•DTU, Technical University of Denmark, DK-2800 Kongens Lyngby, Denmark*

(Received 16 May 2007; revised manuscript received 23 August 2007; published 23 October 2007)

A comparative analysis of metal-oxide-semiconductor (MOS) capacitors by capacitance-voltage (*C-V*) and current-voltage (*I-V*) characteristics has been employed to characterize the thickness variations of the oxide on different length scales. Ultralarge area (1 cm^2) ultrathin (~5 nm oxide) MOS capacitors have been fabricated to investigate their functionality and the variations in oxide thickness, with the use as future electron emission devices as the goal. *I-V* characteristics show very low leakage current and excellent agreement to the Fowler-Nordheim expression for the current density. Oxide thicknesses have been extracted by fitting a model based on Fermi-Dirac statistics to the *C-V* characteristics. By plotting *I-V* characteristics in a Fowler plot, a measure of the thickness of the oxide can be extracted from the tunnel current. These apparent thicknesses show a high degree of correlation to thicknesses extracted from *C-V* characteristics on the same MOS capacitors, but are systematically lower in value. This offset between the thicknesses obtained by *C-V* characteristics and *I-V* characteristics is explained by an inherent variation of the oxide thickness. Comparison of MOS capacitors with different oxide areas ranging from 1 cm^2 to 10 μm^2, using the slope from Fowler-Nordheim plots of the *I-V* characteristics as a measure of the oxide thickness, points toward two length scales of oxide thickness variations being ~1 cm and ~10 μm, respectively.

DOI: 10.1103/PhysRevB.76.155315 PACS number(s): 73.40.Qv, 73.43.Jn, 77.22.Jp, 85.45.Db

I. INTRODUCTION

Solid-state low energy electron emitters have a variety of potential application in science and technology. Several of such potential applications require inexpensive electron emitters.[1] Free electrons can be obtained by heating a filament and extracting electrons with a high voltage extractor. In many applications, the use of such a filament is a problem due to its size, the heat evolved, outgassing,[2] or the light emitted. It has been a goal for decades to be able to substitute these traditional electron sources with inexpensive compact silicon-based cold-cathode emitters.

Most on-chip electron emitters available today are based on the field effect type emitter structure. The field effect emitter has to be operated in vacuum, since it cannot withstand operation at high pressure due to the high fields involved. Another approach to achieve a semiconductor electron emitter is by using a metal-oxide-semiconductor (MOS) structure with an ultrathin oxide acting as a tunnel barrier.[3–5] Oxide film thicknesses on the nanometer scale allow electrons to tunnel from the semiconductor substrate into the top metal film. Applying a voltage larger than the work function of the metal film across such a structure will lead to electrons being emitted into vacuum[3,6,7] if the gate metal film is sufficiently thin. These devices work at low voltages (<10 V), low temperatures, and have a nearly pressure-independent emission.[8] The drawback compared to the field emitter is the low emission current density.

In order to increase the emission current, the area of the thin oxide forming the tunnel barrier must be enlarged. The great challenge of implementing MOS structures as electron emitters lies in the fabrication process, since it is extremely difficult to produce an ultrathin oxide film which is still electrically insulating and nearly defect-free over an ultralarge area, e.g., 1 cm^2. When scaling up the oxide area, the number of statistical defects leading to electric breakdown of the oxide increases dramatically,[9] which leads to a high probability of having a significant fraction of nonfunctional devices. This underlines the necessity of having a means to characterize large area oxides if these devices are to be successfully implemented in electronic devices.

The variation of oxide thickness is of great importance to large area electron emitters for several reasons. One reason is the breakdown of the oxide being of the weakest-link nature.[9] The number of weak points due to spots of thin oxide will scale with the area and, therefore, be more important the larger the oxide area is since breakdown in one of these weak spots is enough to render the whole oxide useless. Another reason is the exponential dependence of the tunneling current on the thickness. The average thickness of the device is, in this way, very important for the absolute brightness of the emission from the device. Furthermore, a variation in thickness will lead to "hot" and "cold" spots in the electron emission being a nuisance in applications where an even distribution of electrons is needed on a certain length scale.

Two possible, unique applications for MOS electron emitters are in electronic catalysis and hot electron emission lithography (HEEL).[10] It has previously been proposed by Gadzuk[11–14] that hot electrons injected from the substrate into the gate in metal-insulator-metal tunnel devices, and thus similar MOS based devices, can be used to enhance surface reactivity on the surface of the ultrathin gate metal. This phenomenon has been investigated experimentally by several groups.[15–19] In HEEL, a MOS electron emitter is used as a combined electron source and mask to illuminate an electron sensitive polymer resist.[10] The patterning is

 ©2007 The American Physical Society

achieved by forming the tunnel oxide or gate metal as a 1:1 mapping of the pattern to be transferred to the substrate. In this way, electron beam lithography can be combined with the massive parallelism known from standard UV lithography.

The MOS capacitor, being one of the most important components in very large scale integration technology as the heart in the field effect transistor (FET), has received a considerable amount of attention in the literature.[20] With regard to FET technology, the thickness variations of the oxide in the MOS structure are important in relation to fluctuations in threshold voltages and electrical breakdown of the oxide, leading to excessive power consumption[21] and possible malfunction. The oxide thickness variations have been characterized on a microscopic length scale by transmission electron microscope,[22] atomic force microscope,[22–24] and scanning tunneling microscope[22,25] measurements. These types of measurements yield valuable information on the micrometer length scale, which is relevant, for example, in FETs, but they do not give the full picture for large area MOS devices, where also longer length scales of variations in the oxide thickness might be important.

Our work is devoted to electronically promoted chemical phenomena, and the devices presented here have been developed to be a platform for delivering hot electrons to a metal surface from within. In this work, we report on the results of the characterization of ultralarge area ($1\ cm^2$) MOS devices with ultrathin tunnel oxides by *I-V* and *C-V* characteristics. Insights into the oxide thickness variations across these large devices are extracted from a comparative analysis of obtained *C-V* and *I-V* characteristics, and are reported here.

Breakdown statistics[23,26–28] are, besides oxide thickness variations, one of the most important characteristics for ultralarge area MOS electron emitters employed in technological applications, but perhaps not as crucial in our future work of studying electronically promoted chemical phenomena. For this reason, we have not devoted serious attention to this aspect, even though we recognize its extreme importance in other applications.

II. EXPERIMENT

A. Fabrication of ultralarge area ultrathin metal-oxide-semiconductor capacitors

The MOS capacitors presented in this paper are fabricated in the cleanroom facilities at Danchip at the Technical University of Denmark. The wafers used are silicon wafers, fabricated by Okmetic, heavily doped with antimony ($\sim 3 \times 10^{18}\ cm^{-3}$), resulting in a resistivity of $<0.025\ \Omega$ cm. A thick oxide of 750 nm is grown by wet thermal oxidation at 1000 °C to serve as an underlayer for a contact pad for electrical measurement purposes. A wet-etch mask is formed by standard photolithography, and the thick oxide is etched back to the substrate in a standard buffered hydrofluoric acid solution to form the areas for the ultrathin tunnel oxide (SiO_2). The wafers are etched for 9 min continuously, and then inspected for a hydrophobic surface. If this has not been achieved, the wafers are etched in steps of 30 s until a hydrophobic Si surface is observed. It is critical to avoid overetching due to the risk of increasing the surface roughness.[29]

The resist is stripped and a standard RCA cleaning procedure[30] is performed. An ultrathin SiO_2 tunnel barrier is grown thermally in a dedicated ultraclean three-zone drive-in furnace at 800 °C in 1 atm of O_2 for 40 min, with a flow of 6 SLM (SLM denotes standard liters per minute). The oxide growth is followed by a 20 min anneal in 1 atm N_2 at 800 °C, with a flow of 6 SLM. Ti/Au (10/100 nm) gate electrodes are deposited using electron-beam physical vapor deposition (PVD), where Ti serves as a wetting layer. Finally, the native oxide is stripped from the backside of the wafer using a 5% HF solution, and a Ti/Au (10/100 nm) backside electrode is deposited using electron-beam PVD.

B. Measurements of the capacitance and current

Due to the large capacitance ($\sim 0.6\ \mu F$) in combination with a high tunneling current of the fabricated MOS capacitors, a special technique for measuring the capacitance-voltage (*C-V*) characteristics is adopted. The technique is designed to measure large capacitances and correct for current from parallel conductance due to tunneling. The capacitance is measured by the use of a switched analog integrator (Fig. 1).

The capacitance of a MOS capacitor can be obtained by applying a signal of the form shown in Fig. 2. For each voltage step in the *C-V* characteristics, a square voltage signal is applied to the MOS capacitor. The reason for using a square signal instead of a simple step is to be able to correct for the current signal due to tunneling electrons.

The voltage versus time signal on the integrator increases or decreases in steps when the MOS capacitor is charged or discharged as a consequence of the applied square voltage signal. In between each charging or discharging step, the integrator signal changes at a constant rate due to the current passing through the MOS capacitor (tunneling or leakage current). The voltages V_0, V_1, V_2, and V_4 are measured since there is no decaying charging or discharging current at these points which would otherwise influence the measurement. The signal from a constant current and charging or discharging of the MOS capacitor can be separated using the following procedure: V_0 is used as the reference zero, and V_1 is subtracted from V_4 to obtain V_3. The signal due to the capacitance of the MOS capacitor, V_C, is $V_2 - V_3$. From this voltage difference, the MOS capacitance is calculated as

$$C_{MOS} = \frac{(V_2 - V_3) C_{ref}}{\Delta V}, \qquad (1)$$

where C_{ref} is the capacitance of the reference capacitor in the integrator and ΔV is the height of the square voltage signal. The current through the oxide of the MOS capacitor and any other leakage currents in the system during Δt are proportional to $V_T = V_3 - V_1$:

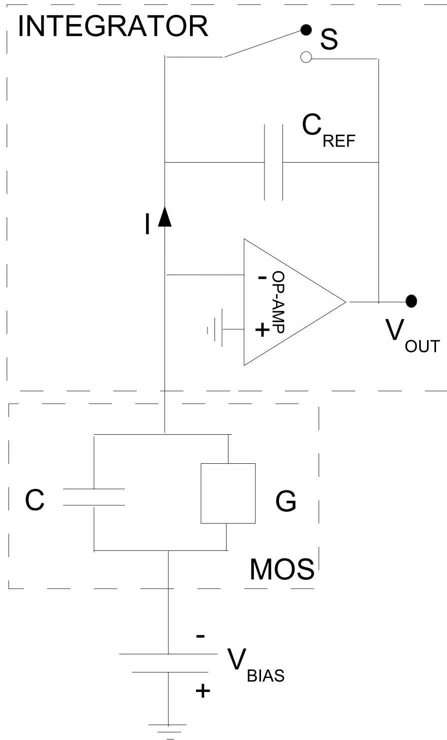

FIG. 1. Diagram of the analog integrator used to measure the *C-V* characteristics presented in this paper. The MOS capacitor under test is modeled as a capacitance C in parallel with a conductance G. The operational amplifier stores the charge flowing to and from the MOS capacitor on the reference capacitor C_{ref}. The switch S is used to reset the integrator before each measurement point. V_{bias} is the bias voltage applied to the MOS capacitor and V_{out} is the readout voltage of the integrator used to calculate the capacitance and current.

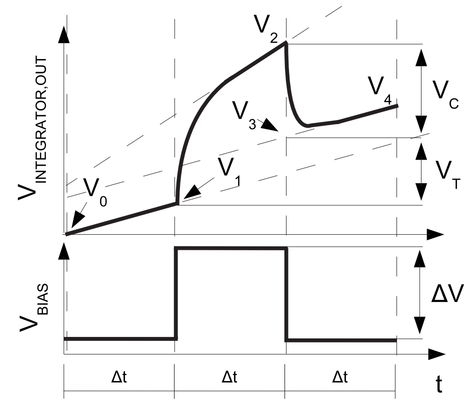

FIG. 2. A sketch of the applied square voltage signal which makes the MOS capacitor charge and discharge, and above, the resulting signal on the integrator. The MOS capacitor is equivalent to a capacitor in parallel with a conductor. The signal on the integrator can be divided into two parts: fast decaying charging and/or discharging signals from the capacitance, and constant increasing signals due to the current flowing through the MOS capacitor. By measuring the voltages V_0, V_1, V_2, and V_4, the current and capacitance of the MOS capacitor can be obtained as explained in the text.

$$I_{\mathrm{MOS}} = \frac{(V_3 - V_1)C_{\mathrm{ref}}}{\Delta t}, \tag{2}$$

where Δt is the duration of the applied voltage pulse. In practice, the current is determined by integration of the current for a period of between 100 μs and 1 s at a constant voltage for better accuracy. Here, the current can be made up of any physical or electronic phenomena in the system such as oxide tunnel current, oxide leakage current, noise induced current, and amplifier bias current.

C. Instrumentation

The bias voltage was generated using a National Instruments PCIe-6259 DAQ card, where the current output was enhanced with a TI BUF634T high speed buffer enabling a maximum current of 250 mA continuously. The MOS capacitors were contacted using Accuprobe *Z*-adjustable probes with gold plated Be and/or Cu tips. The voltage output was measured at the output pin of the TI BUF634T to account for offset and nonunity gain.

The instrument has seven reference capacitors, each covering one decade (4.7 pF–47 μF), switched using standard reed relays. This combined with the variation of the integration time results in a theoretical dynamic range of 14 decades. In practice, this is limited to 11 decades due to the current limitation of the output amplifier (250 mA) and the noise level of the instrument (picoamperes).

I-V characteristics were also measured using a Keithley 485 ampere meter with a dynamical range from 0.1 pA to 2 mA.

D. Extraction of the oxide thickness

From the *C-V* characteristics, the oxide capacitance is extracted from the total capacitance of the MOS capacitor by fitting it to the exact solution to Poisson's equation for the system using Fermi-Dirac statistics for the electrons in the semiconductor. It is important to use Fermi-Dirac statistics for this system due to the high dopant concentration in the silicon wafers used and due to the very high surface field. Using Boltzmann instead of Fermi-Dirac statistics typically returned 1 Å higher values for the thickness of the oxides. Since the *C-V* characteristics are obtained at high frequency, interface traps are neglected in the extraction of the oxide thickness. The model assumes spatially constant dopant impurity concentration, and interface traps and minority carrier capacitances are neglected. This model, known as the McNutt-Sah-Walstra algorithm, has earlier been used as the benchmark for five other *C-V* oxide thickness extraction algorithms by Walstra and Sah.[31] In addition to fitting the thickness, we also allow for a variation in the dopant concentration to circumvent any misleading changes in the oxide thickness from variations in dopant concentration, which could give rise to changes in the semiconductor capacitance in series with the oxide capacitance.

The oxide thickness is calculated from the oxide capacitance as[32]

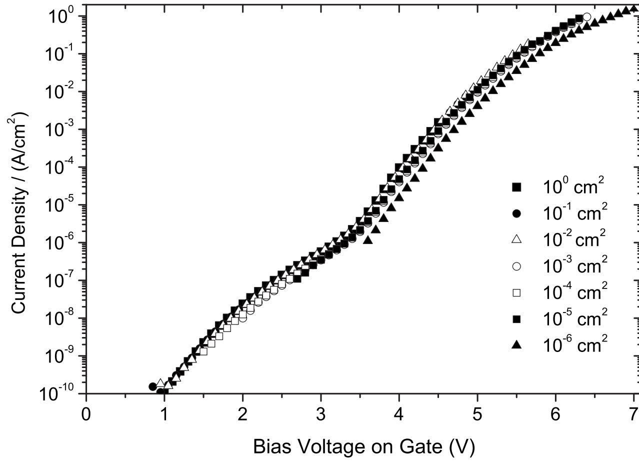

FIG. 3. The current density as a function of gate voltage for seven MOS devices, with oxide areas ranging from 10^{-6} to 1 cm^2. The reason for the different voltage range of measurements on different area devices is the dynamical range of the ammeter.

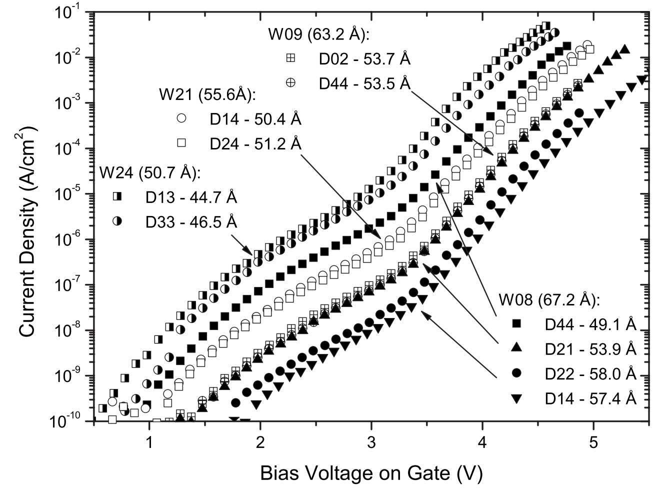

FIG. 4. Measured *I-V* characteristics of ten devices from four wafers, all with an oxide area of 1 cm^2. The oxide thickness measured by ellipsommetry measured on each wafer is shown in parentheses. There is a spread in the oxide thickness between devices, but the thickness extracted from *C-V* measurements agrees qualitatively well with the relative positions of the *I-V* characteristics and the thickness implied therefrom.

$$X_{ox} = \frac{\epsilon_0 \epsilon_{ox} A}{C_{ox}}, \tag{3}$$

where ϵ_0 is the permittivity of vacuum, ϵ_{ox} is the relative dielectric constant of the oxide (SiO_2:3.9), A is the MOS capacitor area, and X_{ox} is the oxide thickness.

III. RESULTS

The results presented here are measured on MOS capacitors on wafers from a single batch. This means that when parallel processing was possible, all wafers were processed in the same run. The MOS capacitors are enumerated according to host wafer and position on same, e.g., W24D02, where W24 is the wafer and D02 is the MOS capacitor.

In Fig. 3, *I-V* characteristics from MOS capacitors with oxide areas ranging from 100 μm^2 to 1 cm^2 with an increment in area of a decade are shown. The current is scaled with area to show the current density. It is seen that the six larger devices have similar current densities, while the smallest device lies a factor of 2–3 lower.

In Fig. 4, the *I-V* characteristics of a range of different 1 cm^2 area MOS capacitors are shown. The MOS capacitors measured are from four different wafers, but with several MOS capacitors from each wafer shown. The oxide thickness measured by ellipsommetry on each wafer is shown in parentheses after each wafer number. The oxide thickness extracted from *C-V* characteristics is shown after the number designating each MOS capacitor. From Fig. 4, it is seen that the thicknesses extracted from *C-V* characteristics and the relative position of the *I-V* characteristics show systematically and qualitatively good agreement. There is a variation in the oxide thickness between different wafers, but also between different MOS capacitors on the same wafer. Figure 4 shows a variation of typically 5 Å in oxide thickness on single wafers, and up to 15 Å from wafer to wafer. Variation in substrate dopant concentration is known to affect oxidation rates,[33,34] which can explain variations in oxide thickness.

IV. DISCUSSION

A. Functionality of ultralarge area oxides

With the general motivation for creating ultralarge area, high current electron emitters in mind, it is important to determine the transport mechanism of the electrons through the oxide. In order to have electron emission, the electrons must have an energy equal to or higher than the work function of the gate metal. This kind of extreme electron heating can only occur if the electrons are tunneling through the oxide. To verify the tunnel nature of the electron transport through the oxide, the higher bias part ($\gtrsim$3.4 V) of the *I-V* characteristics is compared to the Fowler-Nordheim[35–37] (FN) model for the current density:

$$J_{FN} = A F_{ox}^2 \exp\left(-\frac{B}{F_{ox}}\right), \tag{4}$$

where F_{ox} is the electric field in the oxide given by $F_{ox} = \frac{V_{ox}}{X_{ox}}$; A and B are constants given by

$$A = \frac{e^3}{16\pi^2 \hbar} \frac{m_{Si}}{\phi_B m_{ox}} \text{ and } B = \frac{4}{3} \frac{\sqrt{2 m_{ox}}}{e\hbar} \phi_B^{3/2}, \tag{5}$$

where e is the electron charge, $\hbar$ is the reduced Planck's constant, m_{Si} is the effective electron mass in silicon, m_{ox} is the effective electron mass in the oxide, and ϕ_B is the barrier height for electron tunneling, given by the difference between the Fermi level in the semiconductor and the conduction band edge of the insulator.

The model can be rewritten so as to yield a mean to linearize the *I-V* characteristics:

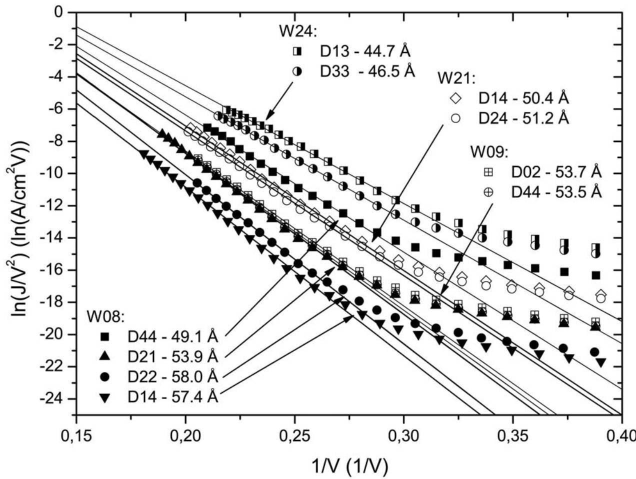

FIG. 5. The *I-V* characteristics from Fig. 4 shown in a Fowler plot. The data yield straight lines in the Fowler-Nordheim regime above 3.4 V, corresponding to ~0.29 on the inverse voltage axis. The slope of the Fowler-Nordheim fit should be proportional to the thickness, as seen from Eq. (6).

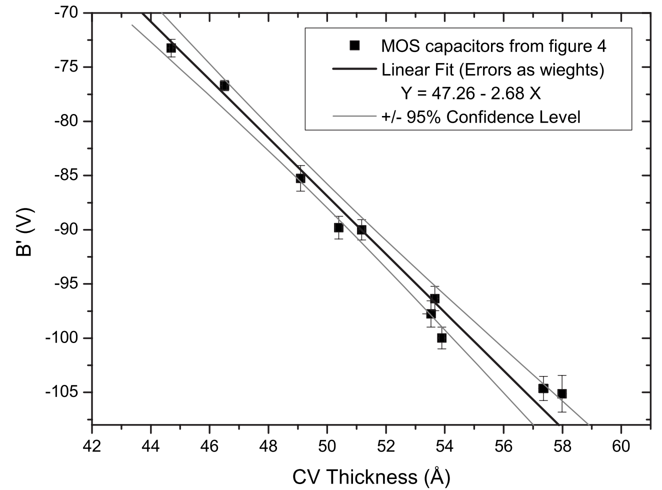

FIG. 6. The extracted slope from fits to the Fowler-Nordheim model (B') plotted against the oxide thickness extracted from *C-V* characteristics on the same devices.

$$\ln\left(\frac{J}{V_{\mathrm{ox}}^2}\right) = \ln(A') - \frac{B'}{V_{\mathrm{ox}}}, \tag{6}$$

where $A' = \frac{A}{X_{\mathrm{ox}}^2}$ and $B' = BX_{\mathrm{ox}}$.

The *I-V* characteristics from Fig. 4 are shown as Fowler plots, using Eq. (6), in Fig. 5. The *I-V* characteristics fit the Fowler-Nordheim model very well above a bias voltage of ~3.4 V, which matches well the sum of typical values for the flatband (FB) voltage $eV_{\mathrm{FB}} = \Phi_{\mathrm{Ti}} - \Phi_{\mathrm{Si}} \approx 4.3\ \mathrm{eV} - 4.1\ \mathrm{eV} = 0.2\ \mathrm{eV}$ and the tunnel barrier height $\phi_B \sim 3.2$ eV.[38]

B. Variations in the oxide thickness

A significant variation of the oxide thickness between devices and certainly from wafer to wafer is observed using *C-V* characteristics, but also more qualitatively from the *I-V* characteristics (Fig. 4) and again quantitatively from the slopes of the Fowler plots in Fig. 5.

From Fig. 4, it can be seen that there is a systematic relation between the thickness measured by *C-V* measurements and the apparent thickness in the *I-V* measurement. In order to quantify this further, the slopes extracted from the Fowler plot in Fig. 5 are plotted against the thicknesses derived from the *C-V* measurements of the same 1 cm^2 MOS capacitors in Fig. 6. From Eq. (6), it is seen that the slope (B') is directly proportional to the thickness of the oxide X_{ox} and would, therefore, be expected to yield a straight line intercepting the origin (0,0) when plotted against the thicknesses extracted from *C-V* measurements. As seen from Fig. 6, plotting B' against the thicknesses extracted from *C-V* measurements yields a straight line, but it does not intercept the origin when extrapolated. The oxide will not be completely flat, but will have a certain roughness and thickness variation from fabrication. A roughness or oxide thickness variation is weighted as $\frac{1}{X_{\mathrm{ox}}}$ in the *C-V* measurement, as seen from Eq. (3), but weighted as $\exp(-X_{\mathrm{ox}})$ in the *I-V* measurement, from which B' is extracted. As a direct consequence of those two different nonlinear weighings, the FN slopes (B') and the thickness probed by the *I-V* measurements will appear thinner than in the corresponding *C-V* measurements. From the fact that the *I-V* measurements give thinner areas exponentially more weight than areas with relatively thicker oxide, the offset in Fig. 6 can be explained by a thickness variation in the oxide. The characteristic length scale of the thickness variation must be on the order of 1 cm or larger, since the oxide thickness variations are clearly not averaged out in measurements on the square (1 cm^2) MOS capacitors.

In Fig. 7, the relative offset of the slope extracted from a Fowler plot is plotted against the nominal area of the devices for four series of devices. A series contains seven devices from 1 to 10^{-6} cm^2 in oxide area, situated close to each other on the same wafer. Since the slope of the Fowler plot is proportional to the thickness [see Eq. (5)] the relative offsets can be interpreted as relative differences in thickness. From Fig. 7, it is seen that there is a typical variation in thickness of ~3%, which for a 50–60 Å thick oxide corresponds to ~2 Å. The thicknesses of the smallest MOS capacitors (10^{-6} cm^2) are significantly larger than those of the larger area MOS capacitors.

The larger apparent thickness of the smallest oxide area MOS capacitors can be understood as a consequence of the variation in oxide thickness. In the simplest model, the thickness variation with a certain length scale is considered in two extreme regimes of MOS capacitor oxide areas. In the first regime, an area of oxide that is far larger than the length scale of the oxide thickness variation is considered. In this situation, an *I-V* measurement samples the entire distribution of oxide thicknesses, and each is weighted exponentially with regard to the thickness, and the total current is the surface integral of the current from each part of the thickness distribution:

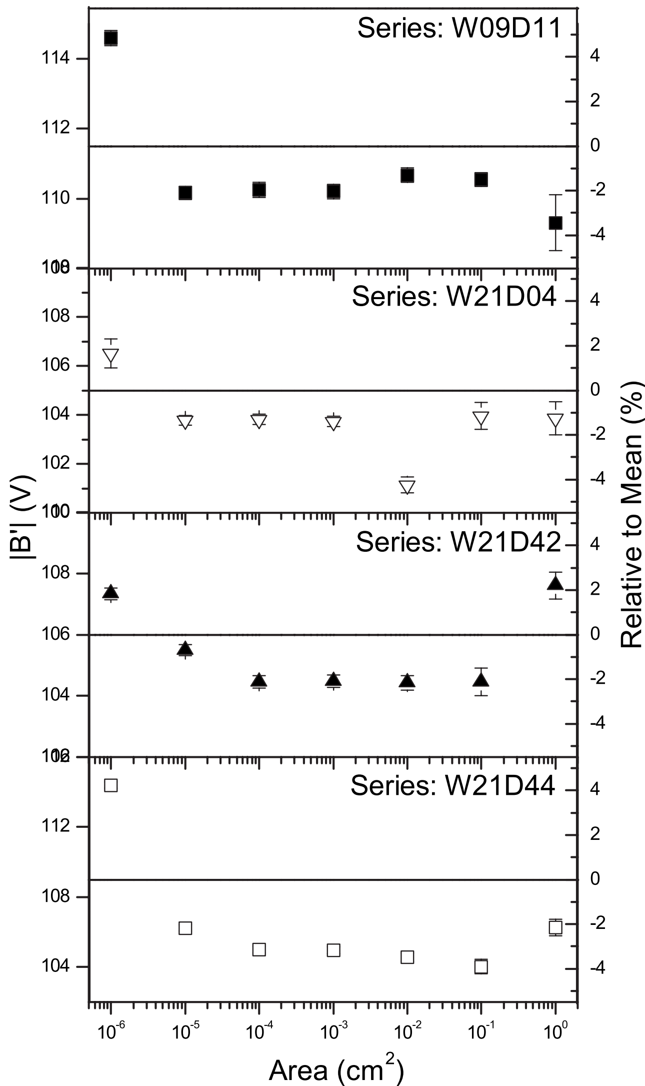

FIG. 7. Slopes (B') extracted from Fowler plots for four series of MOS capacitor, each series includes seven MOS capacitors of increasing area. The left axis shows the absolute value of the slopes, which are proportional to the oxide thickness. The right axis shows the relative deviation of each slope compared to the mean of each series. The error bars express the standard deviation of each slope value from the linear fit to the data plotted in a Fowler plot, not the statistical variation in oxide thickness for a particular MOS capacitor area.

$$I_{tot} = \int J_{FN}(X_{ox}(x,y))dA, \tag{7}$$

where I_{tot} is the total current of the MOS capacitor and $J_{FN}(X_{ox}(x,y))$ is the Fowler-Nordheim current density of a part of the oxide, with the thickness X_{ox} situated at (x,y). The current is integrated over the entire oxide area.

In the opposite extreme, the area of the MOS capacitor is very small compared to the length scale of the roughness or thickness variation; in this case, an *I-V* measurement samples one thickness of oxide and the *I-V* measurements for a series of MOS capacitors yield a distribution of current densities reflecting the variation in oxide thickness. Due to the exponential weighting by the tunnel current, the thicknesses extracted from the *I-V* measurements will be lower than the arithmetic mean of the distribution of oxide thicknesses present in the area sampled. Therefore, depending on the exact nature of the oxide thickness variation distribution, there will always be a larger probability of finding a larger than a smaller thickness of the smaller MOS capacitors compared to the larger MOS capacitors.

Taking an oxide thickness variation and an accompanying characteristic length scale into account make Fig. 7 relatively straightforward to interpret as expressing variations in oxide thicknesses with a characteristic length scale being $\sim 10\ \mu m$. Another explanation for the larger apparent thickness of the smallest area ($100\ \mu m^2$) MOS capacitors could be an edge effect arising from the fabrication technique, where back etching of a thick wet oxide to the Si substrate defines the area of the MOS capacitor as described in Sec. II A. In this case, one has to remember that the FN slope (B') is not directly dependent on the area of the MOS capacitor, but only indirectly through the integration of the current distribution [Eq. (7)].

The fact that the FN slope (B') is independent of area and no assumptions of the tunneling parameters, such as barrier height (ϕ_B) and effective electron mass in the oxide (m_{ox}), have been made makes this method of characterization very robust.

V. CONCLUSION

MOS devices with ultralarge area ($1\ cm^2$) and ultrathin oxides (~ 5 nm) have been fabricated and characterized electrically by *C-V* and *I-V* measurements. The oxide thickness has been extracted from *C-V* characteristics by fitting to a model incorporating band bending and Fermi-Dirac statistics. The thicknesses obtained are realistic from an absolute perspective, by comparing with ellipsommetry, and they show qualitatively and systematically good agreement with the *I-V* characteristics. The thicknesses extracted from *C-V* characteristics as well as the *I-V* characteristics show a significant variation in the oxide thickness between MOS capacitors on the same wafer as well as between wafers. The spread in thicknesses measured on a single wafer is ~ 5 Å, while between wafers it is ~ 15 Å. The *I-V* characteristics of the MOS capacitors fit the Fowler-Nordheim model well in the region where the model is applicable, which is a strong evidence for the tunnel transport mechanism being dominant, and indicates that the MOS capacitors will work as electron emitters with a thinner gate metal layer. The *I-V* characteristics for the $1\ cm^2$ MOS capacitors are comparable to those with smaller oxide areas ($10^{-1}-10^{-6}\ cm^2$). The smallest area MOS capacitors are significantly different from the others, which is well explained by the variation of the oxide thickness on a length scale comparable to the side length of these. The slopes extracted from Fowler plots give a different method of characterizing the oxide thickness and, when comparing several orders of magnitude of area, also a good quantitative measure of the oxide thickness variations and the characteristic length scales of these. For the MOS capacitors

fabricated in this work, two length scales of importance, namely ~10 μm and ~1 cm, were found. Of course, the data presented here are just a few samples of statistical phenomena and it is, therefore, not possible to conclude on the exact nature of the oxide thickness variations. It would be very interesting to see more elaborate studies of oxide thickness variations using slopes extracted from Fowler plots to gain information on the thickness variation of ultrathin oxides.

With regards to the motivation for the fabrication of ultralarge area electron emitters and the issues of oxide thickness variation discussed in the Introduction, there might be a problem with the large variation of thicknesses that is seen between different and across single large area MOS capacitors, since this can easily lead to a large difference in current density both between devices and from one side of a device to the other. These thickness variations might be improved upon by implementing alternative oxide growth methods and annealing, or, perhaps, by using alternative insulating materials for tunnel barriers.

ACKNOWLEDGMENT

The work presented has been funded by the Danish National Research Foundation as part of their grant to the Center for Individual Nanoparticle Functionality.

*ibchork@fysik.dtu.dk

[1] N. S. Xu and S. E. Huq, Mater. Sci. Eng., R. **48**, 47 (2005).
[2] B. R. F. Kendall, J. Vac. Sci. Technol. A **17**, 2041 (1999).
[3] J. Cohen, J. Appl. Phys. **33**, 1999 (1962).
[4] J. Cohen, Appl. Phys. Lett. **1**, 61 (1962).
[5] T. Sumiya, H. Fujinuma, T. Miura, and S. Tanaka, Appl. Surf. Sci. **130–132**, 36 (1998).
[6] D. J. DiMaria, M. V. Fischetti, J. Batey, L. Dori, E. Tierney, and J. Stasiak, Phys. Rev. Lett. **57**, 3213 (1986).
[7] S. D. Brorson, D. J. DiMaria, M. V. Fischetti, F. L. Pesavento, P. M. Solomon, and D. W. Wong, J. Appl. Phys. **58**, 1302 (1985).
[8] H. Mimura, Y. Neo, H. Shimawaki, T. Matsumoto, and K. Yokoo, Appl. Surf. Sci. **144**, 498 (2005).
[9] E. Y. Wu and J. Sune, Microelectron. Reliab. **45**, 1809 (2005).
[10] M. Poppeller, E. Cartier, and R. M. Tromp, Microelectron. Eng. **46**, 183 (1999).
[11] J. W. Gadzuk, Phys. Rev. Lett. **76**, 4234 (1996).
[12] J. W. Gadzuk, J. Vac. Sci. Technol. A **15** 1520 (1997).
[13] J. W. Gadzuk, Phys. Rev. B **44**, 13466 (1991).
[14] J. W. Gadzuk and C. W. Clark, J. Chem. Phys. **91**, 3174 (1989).
[15] D. Diesing, G. Kritzler, M. Stermann, D. Nolting, and A. Otto, J. Solid State Electrochem. **7**, 389 (2003).
[16] T. Wadayama, A. Kojim, and A. Hatta, Appl. Phys. A: Mater. Sci. Process. **79**, 1891 (2004).
[17] D. Diesing, H. Janssen, and A. Otto, Surf. Sci. **331–333**, 289 (1995).
[18] R. G. Sharpe, S. J. Dixon-Warren, P. J. Durston, and R. Palmer, Chem. Phys. Lett. **234**, 354 (1995).
[19] T. Wadayama and M. Yokawa, Chem. Phys. Lett. **428**, 348 (2006).
[20] E. H. Nicollian and J. R. Brews, *MOS (Metal Oxide Semiconductor) Physics and Technology* (Wiley, New York, 1982).
[21] M. Hirose, M. Koh, W. Mizubayashi, H. Murakami, K. Shibahara, and S. Miyazaki, Semicond. Sci. Technol. **15**, 485 (2000).
[22] P. Mur *et al.*, Appl. Surf. Sci. **175–176**, 726 (2001).
[23] M. Houssa, T. Nigam, P. W. Mertens, and M. M. Heyns, Solid-State Electron. **43**, 159 (1999).
[24] O. Maida, H. Yamamoto, N. Okada, T. Kanashima, and M. Okuyama, Appl. Surf. Sci. **130–132**, 214 (1998).
[25] A. Crossley, C. J. Sofield, J. P. Goff, A. C. I. Lake, M. T. Hutchings, and A. Menelle, J. Non-Cryst. Solids **187**, 221 (1995a).
[26] S. Lombardo, J. H. Stathis, B. P. Linder, T. Watson, K. L. Pey, F. Palumbo, and C. H. Tung, J. Appl. Phys. **98**, 121301 (2005).
[27] B. P. Linder and J. H. Stathis, Microelectron. Eng. **72**, 24 (2004).
[28] J. Verweij and J. Klootwijk, Microelectron. J. **27**, 611 (1996).
[29] A. Crossley, C. J. Sofield, J. P. Goff, A. C. I. Lake, M. T. Hutchings, and A. Menelle, J. Non-Cryst. Solids **187**, 221 (1995b).
[30] W. Kern, *Handbook of Semiconductor Wafer Cleaning Technology—Science, Technology, and Applications* (Noyes, New York, 1993).
[31] S. V. Walstra and C.-T. Sah, IEEE Trans. Electron Devices **44**, 1136 (1997).
[32] E. Vincent, G. Ghibaudo, G. Morin, and C. Papadas, Proceedings of the IEEE International Conference on Microelectronic Test Structures, Monterey, CA, 1997 (unpublished), pp. 105–110.
[33] C. P. Ho and J. D. Plummer, J. Electrochem. Soc. **126**, 1516 (1979).
[34] C. P. Ho and J. D. Plummer, J. Electrochem. Soc. **126**, 1523 (1979).
[35] R. H. Fowler and L. W. Nordheim, Proc. R. Soc. London, Ser. A **119**, 173 (1928).
[36] M. Lenzlinger and E. H. Snow, J. Appl. Phys. **40**, 278 (1969).
[37] Z. Weinberg, J. Appl. Phys. **53**, 5052 (1982).
[38] H. C. Card, Solid State Commun. **14**, 1011 (1974).

Electron Emission from Ultra-Large Area MOS Electron Emitters

Lasse B. Thomsen,[1] Gunver Nielsen,[1] Søren B. Vendelbo,[1] Martin Johansson,[1] Ole Hansen,[1, 2] and Ib Chorkendorff[1, *]

[1] *CINF - Center for Individual Nanoparticle Functionality, Department of Physics, Technical University of Denmark, DK-2800 Kgs. Lyngby, Denmark*

[2] *Department of Micro- and Nanotechnology, Technical University of Denmark, DTU Nanotech, Building 345 East, DK-2800 Kongens Lyngby, Denmark*

(Dated: March 1, 2009)

Ultra Large MOS devices with an active oxide area of 1 cm^2 have been fabricated for use as electron emitters. The MOS structures consist of an Si substrate, an SiO_2 tunnel barrier (∼5 nm), a Ti wetting layer (3-10 Å), and an Au top layer (5-60 nm). Electron emission from the Au metal layer to vacuum is realized from these devices by applying bias voltages larger than the work function of the Au layer. The emission is characterized for Au layers with thicknesses ranging from 5 to 60 nm nominally. The emission efficiency changes from close to 10^{-6} to 10^{-10}. The Ti wetting layer is varied from 3 to 10 Å which changes the emission efficiency by more than one order of magnitude. The apparent mean free path of ∼5 eV electrons in Au is found to be 52 Å. Deposition of Cs on the Au film increased the electron emission efficiency to 4.3 % at 4 V by lowering the work function. Electron emission under high pressures (up to 2 bar) of Ar was observed.

Introduction

In many scientific and technological applications electron emitters are necessary[1]. Traditionally free electrons have been generated from hot filaments[2], where a tungsten wire is heated by a direct current until some of the electrons gain enough energy to escape the work function of the filament. Such filaments have several drawbacks such as their size, extensive heating of surroundings, outgassing[3], high intensity light emission and poor control of the direction of the emitted electrons. For many years it has been a goal to develop low cost[1], preferably silicon-based, cold-cathode electron emitters, which could be integrated on-chip.

Today most on-chip cold cathode electron emitters in application are of the field effect type[1,4]. In such devices the high fields generated at geometrically sharp tips are used to draw out electrons from solid-state to vacuum. These emitters can only be operated under vacuum conditions since the devices cannot stand the high fields at the tips under high pressure due to formation of discharges between the anode and the tip.

The work presented in this article investigates the electron emission characteristics of a Metal-Oxide-Semiconductor (MOS) electron emitter[5–9]. This type of emitter works by biasing an ultra-thin tunnel barrier which is sandwiched between two electrodes, a semiconductor and a metal layer. When the bias voltage across the tunnel barrier is larger than the work function of the metal layer, electrons are emitted to vacuum[6,10,11]. The electrons are scattered in the metal layer[12,13], so to achieve a high efficiency of electrons emitted to vacuum relative to the electrons transported through the tunnel barrier the metal layer should be kept as thin as possible while still uniform. In practice electron emission can be realized from metal layers a few tens of nanometers thick and below.

The MOS type of cold-cathode electron emitter is free from many of the drawbacks which traditional and field-effect emitters suffer from. MOS electron emitters will theoretically have no outgassing, generate no significant amount of heat, they can be made extremely small, and be operated under a wide range of conditions[14]. As demonstrated in this work the emitters can operate in the range from vacuum up to at least atmospheric pressure. Furthermore these emitters can easily be fabricated in any shape and size to give emission in a given pattern, which is utilized in Hot Electron Emission Lithography (HEEL)[15]. Furthermore the turn-on and -off rate of the MOS electron emitters is only limited by the resistance capacitance (RC) product of the devices. The weak points of the MOS electron emitter are the low emission current density, here we report up to 36 nA cm^{-2}, and possible breakdown of the insulator tunnel barrier during operation[16–19]. Insulator breakdown will rapidly decrease the emission efficiency and in the end render the device useless.

To increase the emission current of the MOS emitter the devices presented in this work are ultra-large with an active area of 1 cm^2. It is a significant challenge to produce MOS emitters with an active area of 1 cm^2 since the SiO_2 tunnel barrier must be close to defect free in order to get a reasonable emission efficiency. When scaling up the area of the thin tunnel oxide the number of statistical defects leading to oxide breakdown increases rapidly[17]. Nonetheless, for our application of investigating surface chemistry enhanced by hot electrons[20–22], an ultra-large area is necessary to be able to detect gas-phase or surface adsorbed reaction products on the MOS electron emitters. The MOS electron emitter is implemented with an n-type Si wafer as substrate, a thermally grown SiO_2 layer (5 nm) as the tunneling barrier, a thin (3-10 Å) Ti wetting layer, and an Au (5-60 nm) layer as the top electrode [23].

In this work we report on the electron emission characteristics from our MOS electron emitters to vacuum, and how the emission is influenced by changing the Au and Ti layer thickness. Furthermore we have investigated

emission under high pressure (2 bar) and the efficiency of a MOS electron emitter with a cesiated Au film.

Experimental

Structure and Fabrication of MOS Electron Emitters

The experiments carried out in this work have all been done on the same type of basic device, Fig. 1; a Metal-Oxide-Semiconductor consisting of a highly Sb doped Si (001) substrate (< 25 mΩ cm) on which an ultra-thin dry thermal silicon dioxide (SiO_2) layer is grown (∼5 nm). The metal top layer consists of a Physical Vapor Deposition (PVD) film of a thin (3 to 10 Å) Ti wetting layer and an Au layer (5 to 60 nm). The MOS electron emitters presented in this paper are fabricated in the cleanroom facilities at Danchip at the Technical University of Denmark. The fabrication procedure has been described in detail elsewhere[23]. The active area of the electron emitter is 1 cm^2.

Measurements of Transmission and Emission Currents

Most of the measurements presented in this work were all carried out in an Ultra-High-Vacuum (UHV) chamber with a base pressure below 10^{-9} mbar. The MOS electron emitters were placed in special sample holders in which a bias voltage could be applied across the oxide. A relatively large (3 × 3 cm^2) Cu plate, which could be biased relative to the MOS electron emitter, was installed as an electron collector and a voltage of +25 V was applied relative to the MOS electron emitter surface, see Fig. 1. During measurements of the electron emission the distance between the collector plate and the Au surface of the MOS electron emitter was approximately 2 mm. Varying the distance (± 1 mm) did not affect the emission current measured. The UHV chamber was blackened out during all emission measurements, otherwise a photo current in the pA range was measured to the collector plate.

The current through the oxide layer of the MOS electron emitters, which was not emitted to vacuum (I_T), was measured using a Keithley 6485 pico ampere meter. A Keithley 6514 electrometer was connected in series between the voltage supply and the collector to measure the current of electrons to the collector (I_E). The MOS electron emitters were biased using a National Instruments M-series digital acquisition card capable of delivering 20 mA of current to the MOS electron emitter. The bias voltage was measured using the same digital acquisition card. From a measurement across a thick Au film (100 nm) using the probes used for contacting the MOS electron emitters the resistance was measured to below 1 Ω, which makes the parasitic voltage drops across the contacts negligible at the currents measured in this work (< 20 mA).

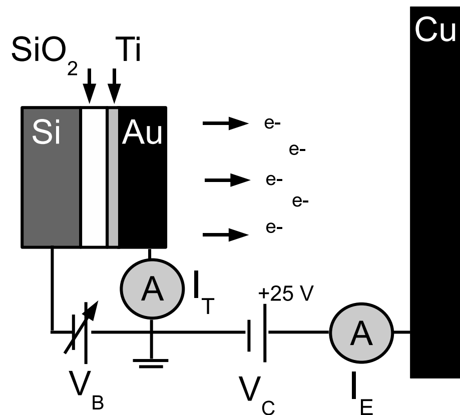

Figure 1: Schematic of the electron emission setup. On the left hand side the MOS electron emitter is depicted with the Si substrate, thermally grown oxide tunnel barrier, Ti wetting layer, and the Au film on top. Under large forward bias (V_B > 4.6 V) electrons are emitted from the Au surface and are attracted to the Cu collector which is biased positively (V_C = 25 V) with respect to the Au surface. The transmission, the current through the layers of the MOS electron emitter, which is not emitted to vacuum (I_T) is measured by an ampere meter, while the current to the Cu collector (I_E) is measured by an electro meter. The distance from the Au surface of the MOS electron emitter to the Cu collector plate is approximately 2 mm.

Measurements of Metal Film Thickness and Integrity

The top metal layers of various thicknesses of Ti and Au were defined using a shadow mask. After deposition the total thickness was measured using a Veeco NanoMan Atomic Force Microscope (AFM). A scan with a side length of 10 to 60 μm was made across the edge of the metal layer and the NanoScope software was used to process the images. The images were first leveled using a first order plane fit and thereafter the step height was measured using a built-in function of the NanoScope software, that compares the average height of two areas, one on each side of the step. For each film thickness one 4” wafer was produced and devices from this were labeled with the metal thickness obtained by AFM. For each wafer the thickness of the metal was measured at several locations across the wafer and an average value of the step height was obtained for the thickness. The integrity of the metal layers was investigated using both AFM roughness measurements and Scanning Electron Microscopy (SEM). The Root Mean Square (RMS) and Absolute Mean (AM) roughness of the metal films were all approximately 1-3 Å. The SEM micrographs showed no signs of discontinuities and only very few voids with a diameter of approximately 50-100 nm. These voids were only found in Au films with thicknesses below 10 nm. Their presence did not correlate with the thickness of the Ti wetting layer.

The measurements done on cesiated devices were after deposition of Cs using a Cs-getter (SAES) mounted in a

water cooled housing with a flag. Cs deposition was done by driving a constant current of 7.2 A through the getter. Before each dose the getter was outgassed for 2 min and the timing of the doses was controlled by turning the flag in front of the getter away and dosing for 20 min. This Cs dose is expected to correspond to a coverage of 1 to 2 monolayers, since we observe the lowest work function after this dosing time.

Measurements of Electron Emission under High Pressures

The measurements of electron emission in high pressures were performed in a mini chemical reactor of stainless steel. The mini reactor area was 14 x 17 mm^2 and the gap between the surface of the MOS electron emitter and the lid of the reactor was 1 mm. The gas pressure was measured using a Brooks 5866 pressure controller. The reactor could be evacuated to high vacuum using a turbo molecular pump. The electron emission was measured using a Keithley 6514 electrometer connected to the lid of the mini reactor. The lid was electrically isolated from the rest of the reactor by a Viton gasket also used as the seal for the reactor. The lid of the mini reactor was biased with +25 V with respect to the MOS electron emitter Au film during measurements in order to attract emitted electrons.

Results and Discussion

Emission from Ti-Au Films

The work presented here is based on simultaneous measurements of the IV-characteristics of MOS electron emitters and the current emitted to vacuum. The current through the SiO_2 tunnel barrier, which is not emitted to vacuum, is labeled as the transmission (I_T), while the current emitted to vacuum is labeled emission (I_E). Three typical consecutive measurements on the same MOS electron emitter are shown in Fig. 2. The first transmission curve shows a typical Fowler-Nordheim (FN) relation between voltage and current. Earlier work on similar devices[23] showed that the transmission transport mechanism obeys the Fowler-Nordheim relation for tunneling. The FN relationship indicates that electrons with high ballistic energy are injected into the metal layer under forward bias (positive voltage on the metal gate compared to the silicon substrate). Electrons are emitted to vacuum if they reach the metal-vacuum interface with enough energy to overcome the work function of the metal layer. On the emission curve for the first run a sharp turn-on is seen at 4.6 V which is the voltage where electrons begin to escape the Au surface and are detected by the positively biased copper collector plate. From the point where the emission takes off, it is growing at a much faster pace than the transmission current, ie., the emission to transmission ratio or efficiency is increasing for

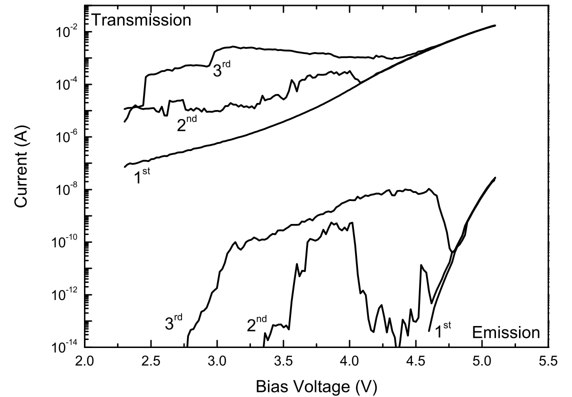

Figure 2: The transmission through the oxide layer of a MOS electron emitter and the resulting emission to vacuum as measured to a positively (+25 V) biased copper collector plate. In this case the metal film consists of 1 nm Ti and 12 nm Au. It is seen how the emission takes off from 4.6 V in the first run, while in the second run emission is seen from as low as 3.3 V. In the third run emission is appearing from 2.75 V. In the first run the transmission shows tunneling behavior as the dominating current transport mechanism while significant leakage current is appearing in the second and third run. Although there are fluctuations in the emission and transmission currents in the second and third run at low voltages, the emission is stable above 4.8 V. The fluctuations in the transmission and emission currents are related to defects in the oxide layer.

increasing voltage.

In the second and third run the oxide is clearly damaged and substantial leakage current is observed from low pre-tunneling bias voltages (<3 V), which is a result of the high bias voltage applied in the first run and can be circumvented by limiting the applied bias voltages to lower values. The transmission is still dominated by the FN-tunneling at high voltages (>4 V) and the MOS electron emitter still emits electrons. A change in the emission current curve pattern is realized at the voltages just below the turn-on of the original emission curve, where electrons are now being emitted at as low as 3 V introducing a shoulder to the original emission curve in the second and third run. At present we have no clear understanding of the origin of these fluctuations, however, they are related to defect creation and progressive breakdown in the oxide layer. Local field enhancement might be responsible for the enhanced emission at low voltages from SiO_2 or Ti, due to opening and closing of nano scale voids in the metal film.

In order to investigate the influence of varying metal layer thicknesses several wafers with MOS electron emitters were fabricated with Au film thicknesses varying from 5 nm to 60 nm nominally. These Au films were deposited on top of a 1 nm Ti wetting layer to avoid roughness and voids, which is critical since the emission current is expected to be exponentially decreasing with

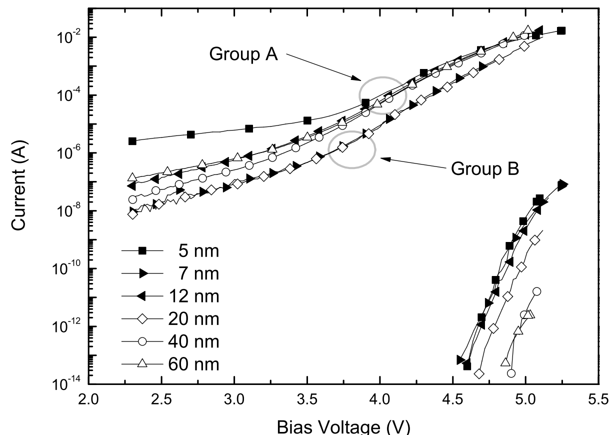

Figure 3: Transmission and emission curves for several MOS electron emitters with varying Au layer thicknesses. The transmission curves fall in two groups, labeled A and B, which is due to variations in oxide thickness[23]. The emission current is in general highest for the thinnest metal gate layers, where the emission takes off at close to 4.6 V. From the thicker metal gate layers the emission seems to take off at higher voltages, but this is due to the noise floor of the experimental setup.

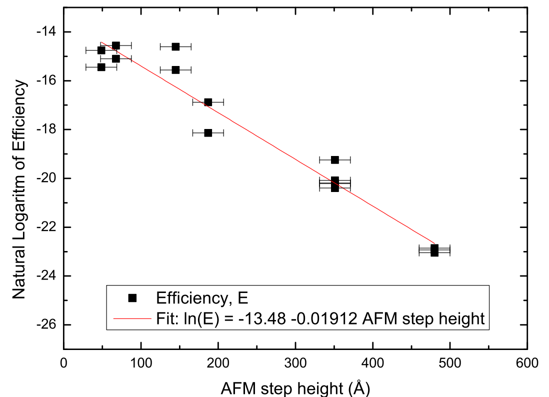

Figure 4: The natural logarithm of the efficiency of electron emission as a function of the metal thickness measured by AFM. The thickness of the Ti wetting layer is 1 nm for the film used in these measurements. The efficiency is calculated from the emission and transmission current at 5V from the first run of each device. It is seen that the efficiency is decreasing exponentially with increasing metal thickness.

thickness. These wafers were all fabricated in one batch using parallel processing up to the final metal layer deposition step. Fig. 3 shows several transmission and emission curves for varying metal layer thicknesses. It is seen how the transmission curves fall in two groups, marked A and B, of curve patterns; one containing the 7 and 20 nm Au film MOS electron emitters and another containing the rest. The reason for the two groups of MOS electron emitters and their different transmission IV characteristics is variations in the oxide thickness[23] leading to changes in the transmission probability for electrons to tunnel through the oxide layer. For the emission curves the general trend is that the thinner the metal layer the higher the emission current, which is due to less scattering of the electrons in the thinner metal layers. There is a higher apparent threshold voltage for the emission current for the thicker metal layer, which is due to the noise of the experimental setup.

Electron Emission as a Function of Film Thickness

In order to investigate how the electron emission of the MOS electron emitters is affected by varying the metal layer thickness, an emission efficiency is defined as the ratio between electrons emitted to vacuum and electrons transported through the oxide, see Eq. 1.

$$\eta = \frac{I_\mathrm{E}}{I_\mathrm{E} + I_\mathrm{T}} \tag{1}$$

From the type of measurement presented in Fig. 2 the efficiency is extracted by reading off the transmission and emission current at a chosen reference voltage and calculating the efficiency by inserting in Eq. 1.

Fig. 4 shows efficiencies calculated from several measurements on Ti/Au films with varying Au thicknesses from 5 to 50 nm, but all with 1 nm Ti as wetting layer. The transmission and emission currents at 5 V were used to calculate the efficiencies. It is clearly seen how the emission efficiency decreases in an exponential manner with increasing metal thickness, which is in good agreement with earlier work on electron transmission through thin metal layers[13,24]. From Fig. 4 the mean free path of the emitted electrons in the Au layer can be extracted from Eq. 2:

$$\eta(\ell) \propto \exp\Big(-\frac{\ell}{\lambda}\Big) \tag{2}$$

where ℓ is the thickness of the Au layer, and λ is the mean free electron path. $\eta(\ell)$ is the efficiency as defined by Eq. 1 as a function of the Au film thickness. From Fig. 4 the mean free path can be found as the inverse of the slope of the fit to the data, which yields a mean free path of 52 Å for the electrons emitted to vacuum at this energy. This value is a bit higher than the 45 Å given by H. Kanter[25] at 5.5 eV electron energy. The lower kinetic energy of these measurements results in a longer mean free path of the electrons and the obtained value agrees extremely well with Krolikowski et al.'s calculations[26].

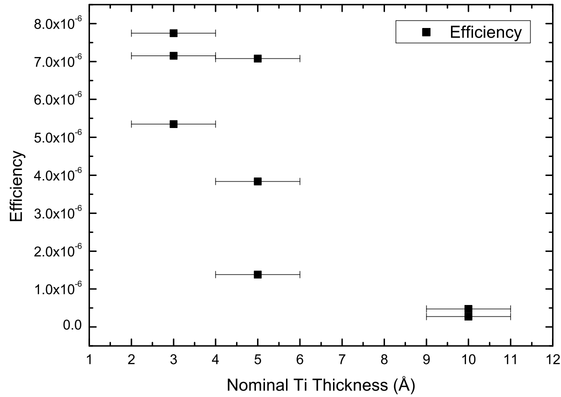

Figure 5: The logarithm of the efficiency of electron emission as a function of the Ti wetting layer nominal thickness. The thickness of the Au layer is 7 nm. The efficiency is, as for the data in Fig. 4, calculated from emission and transmission current at 5 V from the first run of each device.

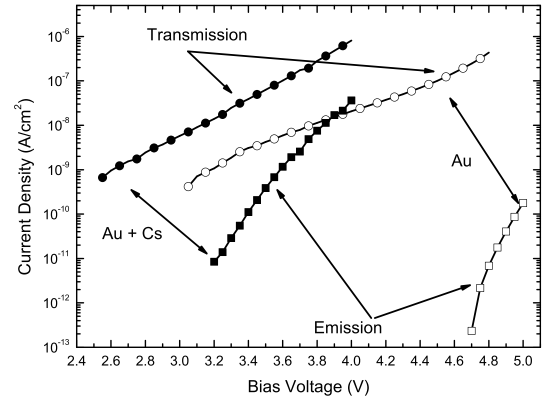

Figure 6: Electron emission to vacuum from a MOS electron emitter. The open symbols show the IV characteristics of the transmission and emission of the as prepared emitter with a 7 nm Au layer while the closed symbols show the same for the emitter after deposition of approximately 1 ML of Cs. The emission threshold is moved considerably from the as prepared Au film to the Cs covered Au film, which indicates a shift of the work function by 1.6 V. The transmission curve of the Cs covered emitter (open circles) is shifted significantly compared to the as prepared Au emitter (closed circles). The emission efficiency of the Cs covered electron emitter is increasing with voltage and is 4.3 % at 4 V.

Electron Emission as a Function of Ti Wetting Layer Thickness

In order to investigate the effect of the thickness of the Ti wetting layer, MOS electron emitters with a nominal wetting layer of 3, 5 and 10 Å Ti underneath a 7 nm Au film were fabricated. In Fig. 5 the results of varying the Ti layer thickness can be seen. It is seen that the efficiency is, as for the Au films, decreasing with the Ti wetting layer thickness, but here the rate of decrease is 22 times faster if one would fit the data to an exponential decay and extract a mean free path. This would, however, be misleading, since existing models predict the mean free path of electrons in Au and Ti to be on the same order of magnitude[26]. We believe that the effect of the Ti wetting layer on the ballistic electrons is to introduce an electric potential scattering region. This scattering potential will arise from the difference in work function of Au (5.40 eV)[27] and Ti (4.63 eV)[27]. The Ti wetting layer has a significant role in the scattering of the ballistic tunnel electrons and must either be kept as thin as possible or perhaps completely circumvented using another metal than Au as the top layer.

Emission Current from a Cesiated Au Film

In order to increase the emission efficiency and bring the operation bias voltage down, Cs was deposited on the Au film surface of a MOS electron emitter. This method have proven to work successfully for similar devices elsewhere[28–30]. The deposition of Cs changed the IV curve as well as the work function of the electron emitter significantly, as can be seen in Fig. 6. The threshold bias voltage for electron emission is changed from 4.7 V to 3.1 V due to the very low work function (2.1 eV[27]) for Cs. The Cs deposition also changes the shape of the IV characteristics for the transmission of the electron emitter. This is probably due to alloying effects between Au and Cs in the Au layer[31] and subsequent migration of Cs to the oxide interface. This migration of Cs from the surface of the Au layer to the SiO_2-Ti-Au interface results in changes in the work function at the oxide interface, which in turn changes the tunnel barrier shape and therefore the transmission coefficient of the SiO_2 tunnel barrier. During the experiments Cs proved to reduce the reliability of the oxide, hence Cs is not a feasible work function lowering agent for technological applications. The efficiency of the electron emitter is, despite the higher transmission, increased by two and a half orders of magnitude. The emission efficiency for the Cs covered electron emitter is 4.3 % at 4 V, where the emission current reaches 36 nA cm^{-2}. The emission from this specific sample is not particularly high due to a relatively thick oxide layer, as seen in the transmission curve. The emission current can be increased by using thinner SiO_2 tunnel barriers. In this way the emission current could theoretically be increased by several orders of magnitude.

Emission Current under High Gas Pressure

A significant advantage of the MOS electron emitter is the ability to operate at high pressures[14]. In Fig. 7 the

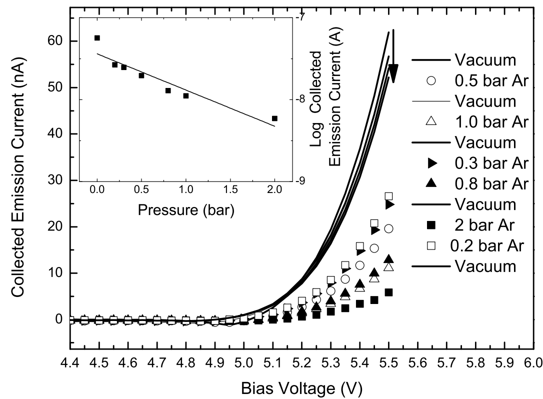

Figure 7: Electron emission from a MOS electron emitter in Ar pressures from 0.1 bar to 2 bar. The collected electron emission current is measured under vacuum conditions (<1 mbar) and then under varying pressures of Ar. After each measurement at high pressure, the emission current measurement was repeated under vacuum (solid lines) and the high pressure measurements were performed in the order expressed by the legend. The inset show the collector current at 5.5 V as a function of Ar pressure.

electron emission from a MOS electron emitter is shown at different pressures of Ar between the collector plate and the surface of the emitter. It is clearly seen that electrons are emitted and collected even at pressures above 1 bar. The ratio of collected electron current under 1 bar of Ar to electron current under vacuum is close to 0.2 which is in very good agreement with the result of Mimura et al.[4]. They report an increase in collected electron current of approximately a factor of 5 from decreasing the pressure from 760 torr of air to vacuum. The inset in Fig. 7 shows the pressure dependence of the emission current to the detector plate as a function of pressure, which is very well described as an exponential decay with increasing pressure of Ar, which points towards the mean free path of electrons in the gas to be important. It is our belief that the decrease in collected electron current as a function of pressure is related to backscattering of emitted electrons into the surface of the emitter. The reason for the increase in backscattering probability, as a function of pressure, is the decreasing ratio between the mean free path of electrons in the gas and the electric field between the emitter and collector attracting electrons towards the collector.

Conclusion

In this work the electron emission from ultra large area (1 cm^2) MOS electron emitters has been investigated under various conditions and we have arrived at the following conclusions:

- The electron emission efficiency is exponentially reduced when the thickness of the Au layer is increased with an apparent mean free path of 52 Å for 5 eV electrons. This result stresses the necessity of having the thinnest possible metal film in order to preserve as many ballistic electrons as possible yielding a high efficiency.

- Variation of the Ti wetting layer thickness showed that increasing the Ti layer by a few Å in thickness results in a decrease in the emission efficiency by an order of magnitude.

- It was shown that it is possible to increase the emission efficiency of the MOS electron emitters by several orders of magnitude using a low work function alkali metal such as Cs. Electron emission efficiencies as high as 4.3 % was observed when the Au film was covered with Cs. Still the absolute emission current of 36 nA cm^{-2} is not very competitive and will have to be improved by going to thinner tunnel barriers. Furthermore Cs was seen to alter the tunnel characteristics of the MOS electron emitters and to some extent degrade the reliability of the oxide. It is our opinion that further research on the combinations of other alkali metals with either Au or another top metal could be very fruitful. Perhaps the way to go is to avoid Au altogether and search for a combination of a gate metal layer that does not need a wetting layer to stick to the oxide and is a better diffusion barrier for Cs and other work function lowering agents.

- The results from electron emission under high Ar pressures prove the pressure versatility of the MOS electron emitter, which could be an advantage in many scientific and technological applications.

Acknowledgement

The work presented has been founded by the Danish National Research Foundation as part of their grant for the Center for Individual Nanoparticle Functionality.

---

* Electronic address: ib.chork@fysik.dtu.dk

[1] N. S. Xu and S. E. Huq. Novel cold cathode materials and applications. *Materials Science and Engineering R*, 48:47–189, 2005.

[2] W. B. Nottingham. Thermionic emission from tungsten and thoriated tungsten filaments. *Physical Review*, 49:78–97, 1936.

[3] B. R. F. Kendall. Ionization gauge errors at low pressures. *Journal of Vacuum Science and Technology A - Vacuum Surfaces and Films*, 17:2041–2049, 1999.

[4] H. Mimura, Y. Neo, H. Shimawaki, T. Matsumoto, and K. Yokoo. Emission characteristics and application of semiconductor field emitters. *Applied Surface Science*, 144:498–503, 2005.

[5] C. A. Mead. Operation of tunnel-emitter devices. *Journal of Applied Physics*, 32(4):646–652, 1961.

[6] J. Cohen. Tunnel emission into vacuum. *Journal of Applied Physics*, 33(6):1999–2000, 1962.

[7] J. Cohen. Tunnel emission into vacuum ii. *Applied Physics Letters*, 1(3):61–62, 1962.

[8] T. Sumiya, H. Fujinuma, T. Miura, and S. Tanaka. Ballistic electron emission microscopy studies of aurcaf rn-si111/ interfaces. *Applied Surface Science*, 130-132:36–40, 1998.

[9] K.H.-J. Fitting, T. Hingst, and E. Schreiber. Breakdown and high-energy electron vacuum emission of misstructures. *Journal of Physics D: Applied Physics*, 32:1963–1970, 1999.

[10] D. J. DiMaria, M. V. Fischetti, J. Batey, L. Dori, E. Tierney, and J. Stasiak. Direct observation of ballistic electrons in silicon dioxide. *Physical Review Letters*, 57(25):3213–3217, 1986.

[11] S. D. Brorson, D. J. DiMaria, M. V. Fischetti, F. L. Pesavento, P. M. Solomon, and D. W. Wong. Direct measurement of the energy distribution of hot electrons in silicon dioxide. *Journal of Applied Physics*, 58(3):1302–1313, 1985.

[12] J. J. Quinn. Range of excited electrons in metals. *Physical Review*, 1(4):1453+, 1962.

[13] C. I Crowell, W . G. Spitzer, L . E. Howarthan, and D E. E. LaBate. Attenuation length measurements of hot electrons in metal films. *Physical Review*, 127(6):2006–2015, 1962.

[14] K. Yokoo, H. Tanaka, S. Sato, J. Murota, and S. Ono. Emission characteristics of metal-oxide-semiconductor electron tunneling cathode. *Journal of Vacuum Science and Technology B*, 11(2):429–432, 1993.

[15] M. Poppeller, E. Cartier, and R. M. Tromp. *Microelectronic Engineering*, 46:183–186, 1999.

[16] S. Lombardo, J. H. Stathis, B. P. Linder, T.J. Watson, K. L. Pey, F. Palumbo, and C. H. Tung. Dielectric breakdown mechanisms in gate oxides. *Journal of Applied Physics*, 98(121301), 2005.

[17] E. Y. Wu and J. Sune. Power-law voltage acceleration: A key element for ultra-thin gate oxide reliability. *Microelectronics Reliability*, 45:1809–1834, 2005.

[18] B. P. Linder and J. H. Stathis. Statistics of progressive breakdown in ultra-thin oxides. *Microelectronic Engineering*, 72:24–28, 2004.

[19] J.F. Verweij and J.H. Klootwijk. Dielectric breakdown i: A review of oxide breakdown. *Microelectronics Journal*, 27:611–622, 1996.

[20] J. W. Gadzuk. Resonance-assisted, hot-electron-induced desorption. *Surface Science*, 1995.

[21] J. W. Gadzuk. Inelastic resonance scattering, tunneling and desorption. *Physical Review B*, 44(24):13466–13477, 1991.

[22] J W Gadzuk and C W Clark. Resonance enhanced electron stimulated desorption. *Journal of Chemical Physics*, 91(5):3174–3181, 1989.

[23] L. B. Thomsen, G. Nielsen, S. B. Vendelbo, M. Johansson, O. Hansen, and I. Chorkendorff. Ultra-large area mos tunnel devices for electron emission. *Physical Review B*, 76(155315):1–7, 2007.

[24] H.-J. Drouhin, G. Lampel, Y. Lassailly, A. J. van der Sluijs, and C. Marlihe. Electron transmission through ultra-thin metal layers and its spin dependence for magnetic structures. *Journal of Magnetism and Magnetic Materials*, 151(3):417–426, 1995.

[25] H. Kanter. Slow-electron mean free paths in aluminum, silver, and gold. *Physical Review B*, 1(2):522–536, 1970.

[26] W. F. Krolikowski and W. E. Spicer. Photoemission studies of the noble metals. ii. gold. *Physical Review B*, 1(2):478–487, 1970.

[27] H. L. Skriver and N. M. Rosengaard. Surface energy and work function of elemental metals. *Physical Review B*, 46(11):7157–7168, 1992.

[28] H. Mimura, Y. Neo, H. Shimawaki, Y. Abe, K. Tahara, and K. Yokoo. Improvement of the emission current from a cesiated metal-oxide-semiconductor cathode. *Applied Physics Letters*, 88, 2006.

[29] J. Drucker and P. K. Hansma. Emission of energetic electrons from tunnel junctions. *Applied Physics Letters*, 30(8), 1984.

[30] H. Mimura, K. Miyajima, and K. Yokoo. Electron emission from porous planar emitters. *Journal of Vacuum Science and Technology B*, 21(4), 2003.

[31] J. A. Rodriguez, J. Hrbek, Y.-W. Yang, M. Kuhn, and T. K. Sham. Photoemission and thermal desorption studies of cs-au and li-au films on ru(oo1). *Surface Science*, 293:260–274, 1993.

* Manuscript
Click here to view linked References

Electron emission from MOS electron emitters with clean and cesium covered gold surface

Gunver Nielsen[a,*], Lasse Bjørchmar Thomsen[a], Martin Johansson[a], Ole Hansen[a,b], Ib Chorkendorff[a,*]

[a] *Center for Individual Nanoparticle Functionality (CINF), Department of Physics, Technical University of Denmark, DK-2800 Kgs. Lyngby, Denmark*
[b] *Department of Micro- and Nanotechnology, Technical University of Denmark, DTU Nanotech Building 345E, DK-2800 Kgs. Lyngby, Denmark*

Abstract

MOS (Metal-Oxide-Semiconductor) electron emitters consisting of a Si substrate, a SiO_2 tunnel barrier and a Ti (1 nm)/Au(7 nm) top electrode, with an active area of 1 cm^2 have been produced and studied with surface science techniques under UHV (Ultra High Vacuum) conditions and their emission characteristics have been investigated. It is known, that deposition of an alkali metal on the emitting surface lowers the work function and increases the emission efficiency. For increasing Cs coverages the surface has been characterized by X-ray Photoelectron Spectroscopy (XPS), Ion Scattering Spectroscopy (ISS) and work function measurements. Energy spectra of electron emission from the devices under an applied bias voltage have been recorded for the clean Au surface and for two Cs coverages and simultaneous work function curves have been obtained. The electron emission onset is seen to appear at the surface work function. A method for cleaning the ex-situ deposited Au top electrodes to a degree satisfactory to surface science studies has been developed, and a threshold for oxide damage by low energy ion exposure between 0.5 and 1 keV has been determined.

Key words: Electron emission, Work function, MOS, UHV

*Corresponding author. Tel.: +45 45 25 31 70; Fax: +45 45 93 23 99
Email addresses: ibchork@fysik.dtu.dk (Ib Chorkendorff)

1. Introduction

Free electron emitters find application in many technological and scientific branches. Tunnel emitters have been investigated and developed for several decades for applications where hot cathodes and field effect emitters [1] can not be applied. Hot cathodes suffer from outgassing, extensive heat generation and light emission and they can only be operated in vacuum. The use of field effect emitters eliminates most of these drawbacks, but they too are not robust in the presence of gas, due to ionization of the gas molecules by the emitted electrons which can lead to either discharges or sputtering of the cathode [1].

Tunnel emitters consist of two electrodes (metal or semiconductor) separated by an insulating layer. When a bias voltage is applied between the two electrodes, electrons will be able to tunnel through the insulator, and if the bias voltage is high enough they may gain sufficient energy to escape the work function of the top electrode, which should be as thin as possible to reduce energy loss by scattering.

In the early sixties electron emission from MIM (Metal-Insulator-Metal) devices was demonstrated [2, 3, 4]. Extensive studies of both MIM and MIS (Metal-Insulator-Semiconductor) tunnel emitters produced in various ways have contributed to the understanding of the transport mechanisms and emission characteristics of tunnel emitters and explored ways to improve the efficiency [5, 6, 7, 8, 9, 10, 11, 12, 13, 14, 15, 16]. A well known and commonly used way of improving the emissivity of the devices is lowering the work function of the top electrode by cesiation [15, 16]. The shortcomings of this type of electron emitters are the emission efficiency and the lifetime, whereas the insensitivity to gas pressure has been demonstrated [16, 17]. The versatility of this type of cold cathode is demonstrated in the various uses, like for instance maskless e-beam lithography [18], electron sources in electron microscopes [19] and for flat panel displays [11].

MIM and MIS tunnel devices as well as Schottky diodes have recently attracted much attention as detectors for currents of chemically induced hot carriers. Detection of such chemicurrents has been reported from molecular adsorption events on MIS devices [20, 21], associative desorption events on MIM devices [22] and oxidation reactions on Schottky diodes [23]. Also the response of tunnel devices to carrier excitation by ion impact is a field of interest [24, 25].

We have developed Si-SiO_2-Au MOS (Metal-Oxide-Semiconductor) de-

vices to be used for Hot Electron Femtochemistry at Surfaces (HEFatS) [26]. These devices have an ultra-large oxide area of 1 cm^2 in order to generate a detectable amount of products from hot electron induced reactions at the surface. The MOS-devices show excellent electrical properties [27], and their capability as electron emitters has also been investigated [17]. This article presents an investigation of Cs deposited on thin Au films using surface science techniques, along with more detailed studies of the emission characteristics of devices with well defined, clean and Cs covered Au surfaces.

2. Experimental

2.1. Fabrication of Tunnel Emitters

The tunnel emitters investigated in this work were fabricated in the Danchip cleanroom facilities at the Technical University of Denmark using standard silicon processing technologies. The substrates are heavily doped n-type (0.025 Ωcm, Sb-doped) Si wafers. A 0.75 μm thick oxide was grown by wet thermal oxidation at 1000°C to serve as a stable underlayer for making electrical contact to the devices. The thick oxide was etched back in buffered hydrofluoric acid (bHF) in order to open 1×1 cm^2 large active areas. Masking was done by standard photolithography. The tunnel oxide was grown in dry oxygen at 800°C, and annealed at the same temperature for 20 min. in nitrogen. This yields a high quality oxide with a thickness of ∼5-6 nm. The top electrode is a Ti wetting layer only 1 nm thick and a thin gold film, 7 nm thick, deposited by Physical Vapor Deposition (PVD) in an e-beam evaporator at a base pressure of 1×10^{-6} mbar. The area was defined by a shadow mask. The process is described in more detail in [27]. A schematic drawing of the cross section of a single device is shown in the inset of Fig. 1. After scribing and dicing of the wafers the devices were cleaned for 4 min. in RCA I [29] solution at room temperature and rinsed in water, before insertion into UHV. This cleaning procedure removes a major part of the carbon containing film covering the gold surface, and makes it possible to clean the top metal surface in-situ to a degree satisfactory for surface science studies.

2.2. UHV Chamber

All experiments were carried out in a standard Ultra High Vacuum (UHV) chamber with a base pressure of 8×10^{-11} mbar, see Fig. 1. The chamber

is equipped with a loadlock system and a wobblestick, facilitating quick exchange of samples without breaking vacuum. Through the sample stage on the manipulator there are isolated connections to the front contacts on both sides of the device and to the back electrode, a thermocouple in contact with the backside and a shielded tungsten filament underneath the sample capable of heating the sample to 550 K. The UHV chamber further includes a Hemispherical Analyzer (HSA) (VSW HA100), an X-ray gun with Mg and Al anodes (VSW Twin Anode X-ray Source), a Quadrupole Mass Spectrometer (Baltzer 125), a Cs-getter (SAES) mounted in a water cooled housing with a flag, and two identical differentially pumped ion guns (Perkin Elmer Phi 04-300). One ion gun is operated when doing Ion Scattering Spectroscopy (ISS), the other one has a smaller incidence angle on the sample and is used for cleaning the sample with low energy oxygen ions. Operation in O_2 slowly burns the filament, so the ion current cannot be kept constant and the filaments are replaced frequently.

X-ray Photoelectron Spectroscopy (XPS) spectra were obtained using the Mg anode for excitation and at a constant pass energy through the HSA of 50 eV. The work function of the analyzer has been determined from the position of the Au $4f_{7/2}$ line, and this value determines the position of the binding energy scale. Work function measurements on the sample were performed by energy analysis of the low energy cutoff of the secondary electrons produced by irradiation with X-rays from the Mg anode. The sample was biased negatively to $\sim$ -25 V relative to the grounded HSA entrance. A small negative bias voltage is needed for the emitted electrons to overcome the work function of the analyzer when this is larger than the work function of the emitting surface. A higher bias voltage should minimize the effects of space charge and magnetic fields on the paths of the electrons to the analyzer, but is in practice not necessary, since equivalent spectra could be obtained along with the emission spectra at a much lower relative bias voltage.

ISS was performed with 1 keV He ions at a constant pass energy of the HSA of 125 eV. Ion currents of around 80 nA to the sample were achieved, and once the temperature of the ion gun had been allowed to stabilize with the filament on, this current was constant. It could be controlled to within a few percent by regulating the He pressure according to the ion gauge readings. The extractor voltage was only turned on when recording spectra, in this way care was taken to limit the ion exposure time of the sample in order to minimize sputtering effects. The scattering angle was 135° with detection along the surface normal. Cs deposition was done by driving a constant

current of 7.2 A through the getter. Before each dose the getter was outgassed for 2 min. and the timing of the doses was controlled by turning a flag in front of the getter, dosing from 30 s and up to 20 min.

The emitted electrons were detected using the HSA, set up for a pass energy of 1 eV which was only possible using a home build, LabVIEW controlled voltage supply. The selection energy of the HSA was kept constant during measurements and the bias on the top electrode relative to the HSA was scanned to complete an energy spectrum of the emitted electrons. This is equivalent to normal operation, where the sample is grounded, and the retarding potential of the HSA is scanned, but technically much easier to set up in this special case. The entry plate of the HSA which controls the retardation of the electrons was kept at -4 V with respect to ground, so that an electron accelerated to 5 eV with respect to the Fermi level of the Si substrate would be retarded to 1 eV kinetic energy and detected. An energy diagram of the sample and the analyzer is shown in Fig. 2a, and for clarity Fig. 2b shows an emission spectrum and the corresponding work function measurement. During these measurements all filaments and light sources in the chamber were turned off and all viewports were blocked, in order to minimize the background of electrons at these low kinetic energies and to eliminate the signal from photoexcited electrons, which we could otherwise detect from the device.

2.3. Cleaning the Au Surface

One of the challenges when producing samples under cleanroom conditions and transferring them to UHV for surface science studies is the cleanliness of the sample surfaces. XPS-spectra confirmed that the primary contaminant was C-species. The thin SiO_2-films are very delicate, so the normal cleaning procedures applied to metal surfaces in UHV like Ar sputtering followed by heating in O_2 and/or H_2 was not successful. We found that the energy of the Ar ions should be very low not to damage the oxide, exposure to 500 eV Ar ions left the IV-characteristics of the device unaltered, whereas only 1 min. exposure to 1 keV ions increased the diode current by one order of magnitude and further exposure led to a soft breakdown. The method of ion implantation in the Si technology for obtaining various doping profiles also suffers from these unwanted effects, and the common solution to this is annealing to high temperatures [28]. The sputter efficiency was very low at these energies, so this method was abandoned. The sample holder only allowed heating to around 650 K, and at this temperature neither O_2 nor H_2 had

any impact on the C overlayer, probably because Au is too noble. However, the nobleness of Au makes it possible to clean the samples in an oxidizing agent immediately before insertion into UHV. Testing the RCA I (H_2O:H_2O_2 30%:NH_4OH 29% in the relation 5:1:1), RCA II (H_2O:H_2O_2 30%:HCl 37% in the relation 5:1:1) and pirañha (H_2SO_4 98%:H_2O_2 30% in the relation 3:1) solutions [29] at room temperature showed good results with RCA I, followed by rinsing in water. The next step was to employ activated O_2 molecules to clean the surface in-situ, and this was achieved by sputtering at 500 V in O_2. At this low energy the ions did not affect the electrical characteristics of the devices, but they are very efficient in removing the surface C. By ISS we could verify that this treatment leaves only a small fraction of a monolayer of carbon on the surface and negligible amounts of oxygen, see Fig. 3, black line. Though ISS proved that the Au-surface was clean, we were not able to eliminate the C 1s peak in the XPS spectrum, most likely due to C incorporated in the film, so we could not quantify the C-coverage by XPS.

3. Results and Discussion

3.1. ISS on Cs/Au-film

The surfaces of the Au top electrodes were investigated with XPS and ISS, both prior to and in between Cs-depositions. Since ISS probes only the topmost atom-layer of a surface it is a more powerful tool when checking the cleanliness of the sample and also in determining coverages of adsorbed species. Fig. 3 compares the full ISS-spectrum of the freshly cleaned sample (black line), with the spectrum after a finished Cs-deposition series (grey line). In the range from 300 eV to 850 eV the spectra have been magnified in the inset. Some signal from the sample holder and the mounting clips (Cu and Mo) is obtained since the ion beam was defocused to cover the whole sample, in order to avoid uneven sputtering of Cs.

The probability for He ions to survive the collision with surface atoms depends strongly on various factors, like geometry, the element of the target atom and shadowing effects from adsorbates [30]. Also the work function of the surface is rather important, since it determines the possible neutralization mechanisms the ions are subject to. Lowering of the work function to a certain level makes resonant neutralization possible, in addition to Auger and collision-induced neutralization [30, 31]. Exactly how the survival probability of the scattering ions depends on the work function seems to vary strongly with scattering geometry and primary ion energy [32, 33], but in general the

survival probability decreases with work function, so that alkali metals give only very small signals in ISS [30, 31, 32, 33, 34]. We were not able to detect any signal from the deposited Cs-atoms, so our approach to determining the absolute Cs-coverage was from attenuation of the Au signal.

Also the exposure to 1 keV He ions during ISS proved to be detrimental to the oxide. The device current has increased after 1 keV He ion exposure and a soft breakdown occurs after exposure times comparable to those for 1 keV Ar ion exposure, so this method could not be applied on samples which were to be used for electron emission. Therefore the correlation between the relative XPS line intensity of the Cs 3d-line and the ISS attenuation was determined. Fig. 4 shows this relation as the integral of the ISS Au-peak versus the integral of the Cs $3d_{5/2}$ line normalized with the integral of the Au 4f lines, assuming the attenuation of the XPS Au-signal due to Cs deposition to be negligible. The integrals are calculated from the raw data after background subtraction (Cs-line: linear background, Au-lines and ISS Au-peak: Shirley background, as implemented in the CasaXPS software). There is a linear relationship at sub-monolayer coverages which flattens out at higher coverages. It should be noted, that the relationship between the relative XPS Cs-line intensity and the deposition time is linear, so the quantification by XPS is a direct measure of the coverage. The grey line in Fig. 4 represents a linear fit to the points 2 to 7. The first point from the clean Au surface is omitted, as it shows an unexplainable low intensity, and we judge the next six points to represent the linear decrease in ISS intensity. The linear fit intersects the abscissa at 0.22 which is the relative Cs $3d_{5/2}$-line intensity corresponding to one monolayer. The exposure to the He ion beam leads to some sputtering, so the XPS spectra as well as the work function were recorded both before and after each ISS spectrum and the average was used. The difference is considerable, ~ 20 %, at low coverages but drops to a few percent at high coverages.

For each data point in Fig. 4 the XPS O 1s line was recorded, and we could not detect any oxidation in this manner. The behavior with an apparent small increase in ISS signal for the smallest Cs dose could not always be reproduced, and we do not have information enough to speculate about its origin.

3.2. Work Function of Cesiated Au-film

The position of the energy cut-off of the secondary electrons escaping the Au-surface represents the work function, an example of a work function curve

can be seen in Fig. 2b, grey line. The work function is determined by making a linear fit to the steep part of the curve and calculating the intersection with the energy axis. This method has proven very robust, it is not very sensitive to the number of data points included in the fit, and it yields the same results as determining the inflection point of the curve from the first order derivative, since we are only interested in work function changes. Here it is practical to use the work function of the cleaned Au-surface as the reference.

In Fig. 5 the change in work function is plotted versus the Cs-coverage as quantified by XPS. The behavior of the curve resembles that of the ISS intensity as can also be seen in the inset showing the ISS intensity versus the work function change. Studies of work function change with alkali metal coverage on single crystals show a minimum at a distinct coverage, dependent on the alkali metal studied [35, 36], the explanation being a maximal polarization of the adsorbates by donation of negative charge to the substrate. This occurs for a certain overlayer structure and is an indication of long range order in the alkali metal layer. We do not see this minimum occur in any of our measurement series, which have also been extended to higher coverages than the one shown here, but this is expected, since the Au-films are poly-crystalline, and the apparent work function will probably be an average of different facets.

Our measurements show an apparent linear dependence of the attenuation of the ISS Au signal with work function. It has been shown in the literature, that the dominating neutralization mechanisms at high work functions (Auger and collision induced) are independent on work function, whereas the resonant neutralization probability depends on the macroscopic or average work function [31, 34]. Cortenraad et al. [31], however, see a continuous decrease in ISS signal from the substrate, and only a work function dependent signal from the Ba add-atoms for the same scattering geometry as in the present study. So the fact, that we determine the Cs coverage from the attenuation of the Au signal data points at low coverage adds credibility to the result, that 1 ML of Cs corresponds to a relative Cs XPS line intensity of 0.22.

3.3. Electron Emission

Having established the characteristics of the Au and cesiated Au-surfaces in terms of cleanliness, work function and Cs-coverage, more detailed studies of the electron emission could be performed. In order to investigate the correlation between the state of the electrode surface and the emission characteristics of the devices, energy spectra of the emitted electrons along with

measurements of the work function for four different surfaces are obtained.

As discussed in Sec. 2.2, Fig. 2a explains the principle of the electron emission measurements. Fig. 2b shows the work function of the clean Au-surface (grey) along with the emission spectrum at a device bias of 4.7 V (black). In these measurements the work function curves are obtained with the same sample/analyzer setup as for the emission measurements, only with the front and back electrodes shorted, and photoelectron excitation by X-rays. Zero on the energy axis is the measured work function of the clean Au-surface, determined from the work function curve as explained above. The work function curve is seen to be rather broad, which we explain by the presence of different Au sites on the surface of the poly-crystalline Au-film. The work function of different facets can from theoretical calculations vary up to 0.75 eV and experimental values are around 5.40 eV [37]. The position of the 4.7 V emission peak relative to the work function curve indicates, that electrons are being emitted from the surface at low-work function sites.

Fig. 6 shows the emitted electron distributions and the work function curves from A: a clean Au surface (the same measurement as in Fig. 2b), B: the Au surface with a Cs coverage of $\sim$ 0.87 ML, C: the Au surface with a Cs coverage of $\sim$ 1.74 ML, and D: the cesiated Au surface after being left for 80 min. under UHV conditions. For each emission spectrum the device bias voltage that gives the onset of emission is chosen The decrease in work function with increasing coverage can be followed and the work function curves get markedly sharper, which could be because the Cs-overlayer makes the overall work function much more homogeneous or because certain low-work function sites dominates the emission. The electron emission spectra confirm that as the work function is lowered, hot electrons can be emitted at lower device bias voltage. The position of the peak corresponds very well to the applied bias, and for the cesiated surfaces the low-energy cut-off in electron intensity follows the work function very nicely. Consequently, much higher emission currents can be achieved by lowering the work function as reported in [17], where integrated emission current vs. device bias voltage curves from similar devices are presented. By cesiation of the surface an emission efficiency of 4.3 % at 4 V device bias voltage can be achieved. For the same device without Cs the emission efficiency at 5 V device voltage is $\sim 10^{-4}$.

Leaving the cesiated Au surface in vacuum for 80 min. increases the work function slightly. This was also seen by LaRue et al. [38] and they speculate, that this can either be due to reaction with the background pressure of for

instance O_2 or water, or desorption of Cs. As discussed in [17], Cs migrates through the Au and into the SiO_2-Ti-Au-interface and possibly further into the SiO_2, compromising the stability of the oxide under bias voltage. For technical applications, therefore, other work function lowering agents or top electrode metals should be investigated.

4. Conclusion

The MOS devices work as electron emitters when applying a bias across the oxide, which is high enough for the electrons to overcome the work function of the top-electrode. Deposition of Cs effectively lowers the work function of the Au top-electrode up to 1 ML of Cs, without the appearance of a minimum, most likely because the Au-film is poly crystalline. Kinetic energy spectra of the emitted electrons at the onset of emission for different Cs coverages confirm that the low energy cut-off of the electron emission is determined by the work function. This implies, that changing the device bias voltage by the same amount as the work function yields qualitatively identical emission spectra.

We have further developed a procedure for cleaning MOS electron emitters with Au top-electrodes produced on Si-wafers in a cleanroom, involving cleansing in an oxidizing agent before insertion in UHV, followed by in-situ cleaning with 500 eV O-ions produced in a normal ion gun, which makes the devices suitable for surface science studies. This low ion energy does not affect the functionality of the devices whereas exposure to 1 keV Ar ions which is often applied for sputter cleaning, as well as exposure to 1 keV He ions during ISS leads to a soft breakdown in the devices, meaning that the device current gradually increases with ion exposure, so that a certain ion dose results in a total breakdown. The threshold energy for ions being able to damage the oxide after passage of the 7 nm Au top-electrode lies between 0.5 and 1 keV.

Acknowledgments

The work presented has been founded by the Danish National Research Foundation as part of their grant for the Center for Individual Nanoparticle Functionality.

References

[1] N.S. Xu, S.E. Huq, Mat. Sci. Eng. R 48 (2005) 47.

[2] C.A. Mead, J. Appl. Phys. 32 (1961) 646.

[3] J. Cohen, J. Appl. Phys. 33 (1962) 1999.

[4] J. Cohen, Appl. Phys. Lett. 1 (1962) 61.

[5] J-S. Kim, T. Hoshi, K. Sawada, M. Ishida, J. Vac. Sci. Technol. B 22 (2005) 1358.

[6] M. Mańkoś, R.M. Tromp, M.C. Reuter, E. Cartier, Phys. Rev. Lett. 76 (1996) 3200.

[7] H. Mimura, Y. Neo, H. Shimawaki, T. Matsumoto, K. Yokoo, Appl. Surf. Sci. 244 (2005) 498.

[8] K. Yokoo, H. Tanaka, S. Sato, J. Murota, S. Ono, J. Vac. Sci. Technol. B 11 (1992) 429.

[9] J. Ikeda, A. Yamada, K. Okamoto, Y. Abe, K. Tahara, H. Mimura, K. Yokoo, J. Vac. Sci. Technol. B 16 (1998) 818.

[10] H. Adachi, J. Vac. Sci. Technol. B 14 (1996) 2093.

[11] K. Sakemura, N. Negishi, T. Yamada, H. Satoh, A. Watanabe, T. Yoshikawa, K. Ogasawara, N. Koshida, J. Vac. Sci. Technol. B 22 (2004) 1367.

[12] K. Yokoo, S. Sato, G. Koshita, I. Amano, J. Murota, S. Ono, J. Vac. Sci. Technol. B 12 (1993) 801.

[13] A. Govyadinov, T. Novet, D. Pidwerbecki, S. Ramamoorthi, J. Smith, J. Chen, C. Otis, D. Neiman, P. Benning, J. Vac. Sci. Tecnol. B 23 (2005) 853.

[14] D.J. DiMaria, M.V. Fischetti, J. Appl. Phys. 64 (1988) 4683.

[15] J. Drucker, P.K. Hansma, Phys. Rev. B 30 (1984) 4348.

[16] H. Mimura, Y. Neo, H. Shimawaki, Y. Abe, K. Tahara, K. Yokoo, Appl. Phys. Lett. 88 (2006) 123514.

[17] L.B. Thomsen, G. Nielsen, S.B. Vendelbo, M. Johansson, O. Hansen, I. Chorkendorff, J. Vac. Sci. Technol. B 27 (2009) (*in press*).

[18] M. Poppeller, E. Cartier, R.M. Tromp, Microelectron. Eng. 46 (1999) 183.

[19] B. van Someren, M.J. van Bruggen, Y. Zhang, C.W. Hagen, P. Kruit, J. Phys.: Conference Series 34 (2006) 1092.

[20] X. Liu, B. Roldan Cuenya, E.W. McFarland, Sensor. Actuat. B Chem. 99 (2004) 556.

[21] B. Roldan Cuenya, H. Nienhaus, E.W. McFarland, Phys. Rev. B 70 (2004) 115322.

[22] B. Mildner, E. Hasselbrink, D. Diesing, Chem. Phys. Lett. 432 (2006) 133.

[23] J.Y. Park, G. A. Somorjai, ChemPhysChem. 7 (2006) 1409.

[24] S. Meyer, D. Diesing, A. Wucher, Nucl. Instrum. Meth. B 230 (2005) 608.

[25] M.P. Ray, R.E. Lake, S.A. Moody, V. Magadala, C.E. Sosolik, Rev. Sci. Instrum. 79 (2008) 076106.

[26] J.W. Gadzuk, Phys. Rev. Lett. 76 (1996) 4234.

[27] L.B. Thomsen, G. Nielsen, S.B. Vendelbo, M. Johansson, O. Hansen, I. Chorkendorff, Phys. Rev. B 76 (2007) 155315.

[28] J.D. Plummer, M. D. Deal, P.B. Griffin, Silicon VLSI Technology - Fundamentals, Practice and Modeling, Prentice Hall, Upper Saddle River, 2000.

[29] W. Kern, Handbook of Semiconductor Wafer Cleaning Technology – Science, Technology and Applications, Noyes, New York, 1993.

[30] H.H. Brongersma, M. Draxler, M. de Ridder, P. Bauer, Surf. Sci. Rep. 62 (2007) 63.

[31] R. Cortenraad, A.W. Denier van der Gon, H.H. Brongersma, S.N. Ermolov, V.G. Glebovsky, Phys. Rev. B 65 (2002) 195414.

[32] M. Beckschulte, E. Taglauer, Nucl. Instrum. Meth. B 78 (1993) 29.

[33] P. Wenter, N. Memmel, Surf. Sci. 513 (2002) L419.

[34] M.J. Ashwin, D.P. Woodruff, Surf. Sci. 244 (1991) 247.

[35] R. Błaszczyszyn, M. Błaszczyszyn, R. Meclewski, Surf. Sci. 51 (1975) 396.

[36] R.W. Verhoef, M. Asscher, Surf. Sci. 391 (1997) 11.

[37] H.L. Skriver, N.M. Rosengaard, Phys. Rev. B 46 (1992) 7157.

[38] J.L. LaRue, J.D. White, N.H. Nahler, Z. Liu, Y. Sun, P.A. Pianetta, D.J. Auerbach, A.M. Wodtke, J. Chem. Phys. 129 (2008) 024709.

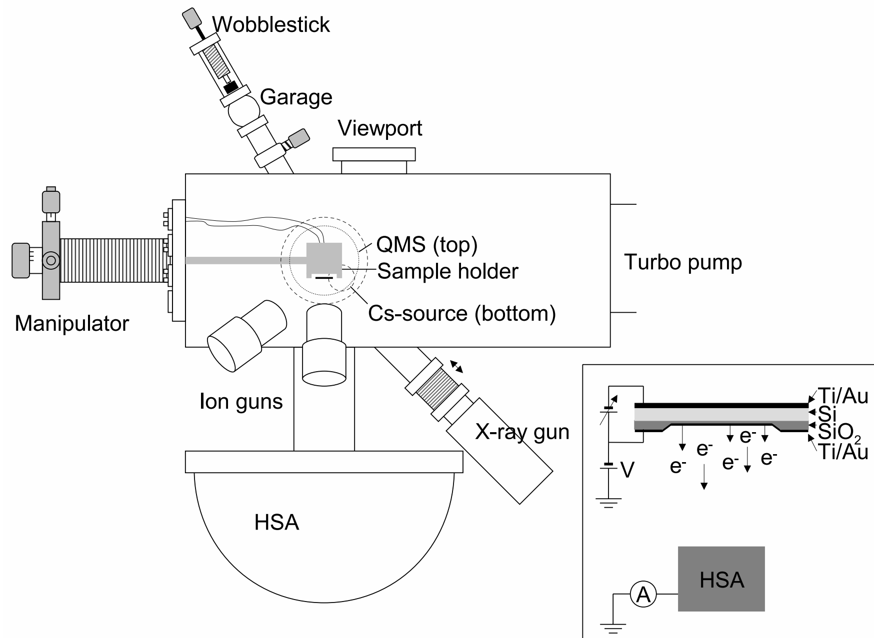

Figure 1: A schematic overview of the UHV chamber. Samples mounted in special sample holders facilitating electrical contact and electrical isolation from the chamber are transferred from the garage to the sample stage in the center of the chamber using the wobblestick. The sample stage can be moved in all three directions and rotated 360°. The chamber has a Hemispherical Analyzer (HSA), two identical, differentially pumped ion guns and an X-ray gun placed on one side. A Cs-getter is mounted in a water cooled Cu-housing at the bottom of the chamber. The chamber further has a Quadrupole Mass Spectrometer (QMS) at the top of the chamber. The inset (not drawn to scale) depicts the structure of a single device consisting of a Si-substrate, a very thin SiO_2 tunnel barrier and the thicker contact pads, and the top and bottom metallization. By applying a bias voltage to the device, electrons can be emitted into vacuum and detected by the HSA, only shown schematically. The detected electrons are amplified by the channeltron at the end of the HSA and the current is detected by an ammeter. The front of the device is biased negatively relative to ground/the HSA.

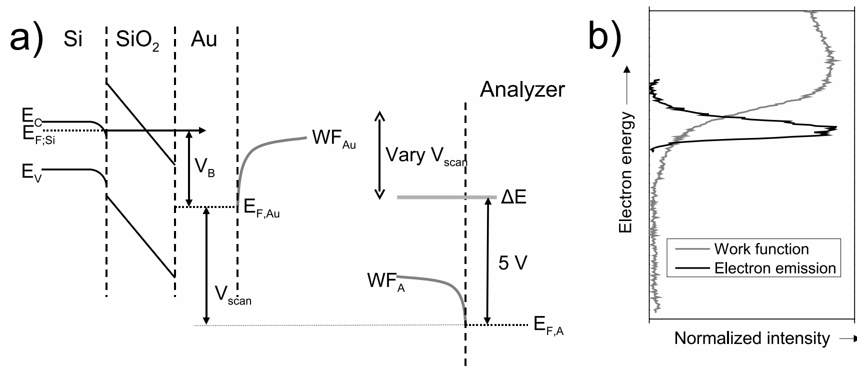

Figure 2: a) Energy diagram depicting the energy levels of the sample and the analyzer when obtaining electron emission spectra. E_F, E_C and E_V designates the Fermi level, the conduction band and the valence band, respectively. The sample is biased by V_B, and when this is high enough, electrons tunneling through the oxide have sufficient energy to escape the work function, WF, of the Au surface. The analyzer is set up to measure electrons of 5 eV kinetic energy at a pass energy of 1 eV, so it has a window open of width ΔE (approximately 1 % of 1 eV = 10 meV), 5 eV above the analyzer Fermi level. The sample floats at a voltage V_{scan} relative to the analyzer, and by scanning this voltage, an energy spectrum of the emitted electrons from the sample can be completed. b) A work function measurement of the clean Au film (grey) is shown along with the emission spectrum at 4.7 V device bias (black).

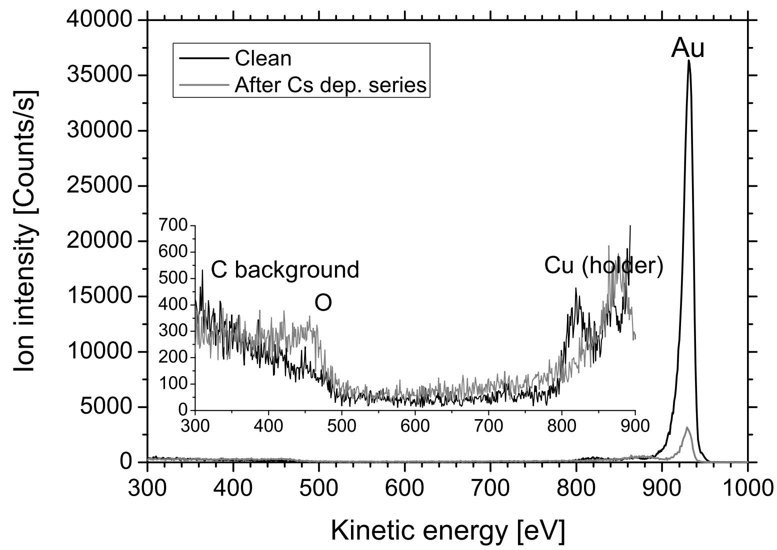

Figure 3: ISS spectra demonstrating the cleanliness of the sample, the inset shows a magnification of the region from 300 eV to 850 eV. Black: after oxygen ion treatment and prior to Cs deposition. The sample has a small C contamination and no oxygen. Grey: after a series of Cs depositions, total duration of the measurements around 6 hours. Oxidation of the Cs overlayer is seen to be almost negligible in XPS spectra of the O 1s line recorded after each Cs dose.

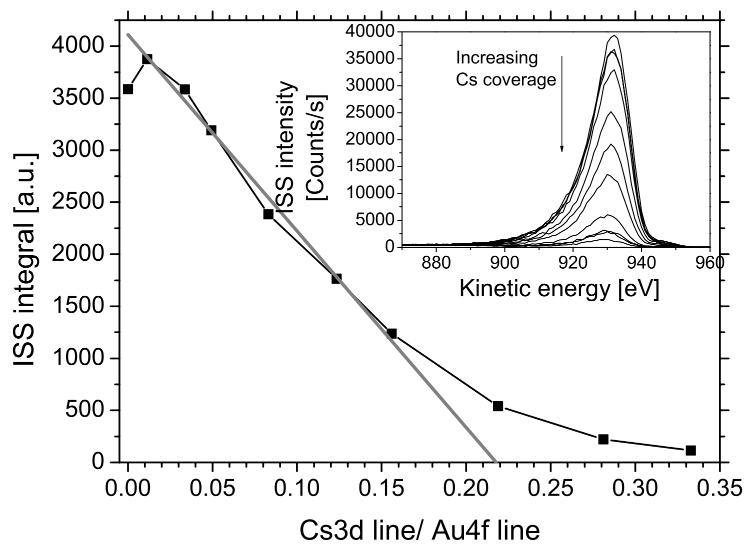

Figure 4: The decrease in the integral of the Au-peak in the ISS spectra with increasing Cs coverage. The Cs coverage is quantified by XPS as the integral of the Cs $3d_{5/2}$ line divided by the integral of the Au 4f lines, assuming negligible attenuation of the Au signal at these low Cs coverages. The plot shows a linear relationship at low coverage. The inset shows the ISS spectra of the Au line as it drops in intensity with increasing Cs coverage.

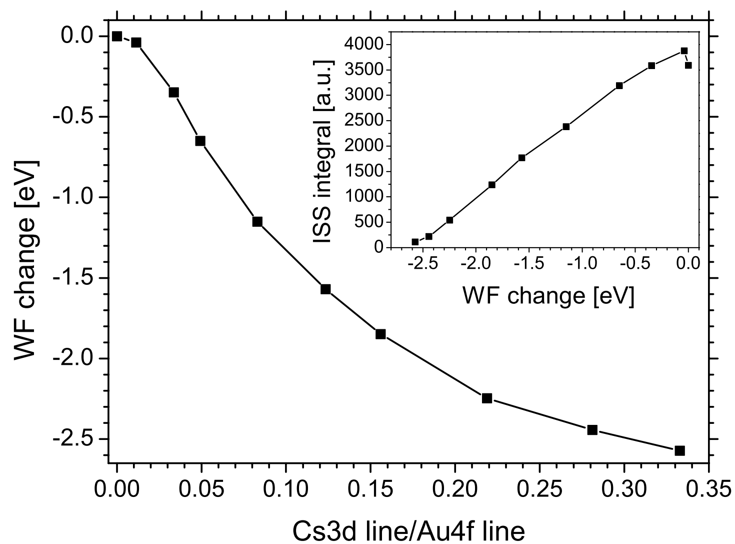

Figure 5: The decrease in work function with increasing Cs coverage quantified by XPS. The work function is seen to decrease linearly with Cs coverage in the regime at low coverages. The inset shows the integral of the Au peak in the ISS spectra vs. the change in work function. There is an apparent linear relationship, see discussion in the text. At the relative Cs XPS line intensity of 0.22 which we interpret as one monolayer, the work function is seen to level out.

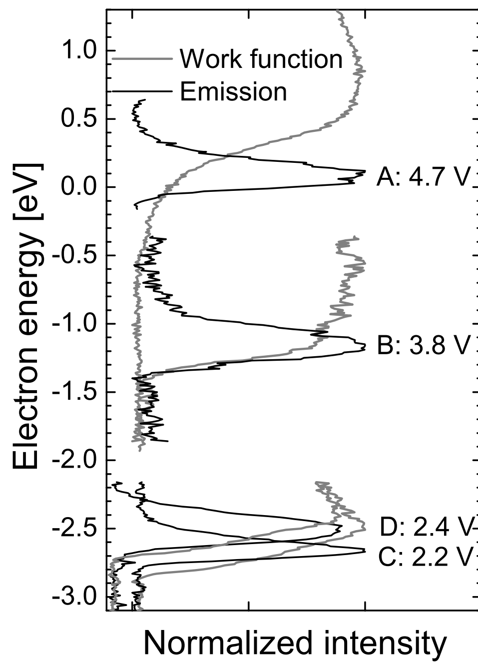

Figure 6: Electron emission energy spectra (black) and work function measurements (grey) recorded for four different states of the surface. A: Clean Au-surface (the same measurement as in Figure 2b)) at a device bias voltage of 4.7 V. B: ∼ 0.87 ML Cs/Au surface, device bias voltage 3.6 V. C: ∼ 1.74 ML Cs/Au surface, device bias voltage 2.2 V. D: Previous surface after 80 min. in UHV, device bias voltage 2.4 V. This curve is shifted to the left for clarity. It is observed how the bias voltage for which tunnel electrons begin to escape the surface is lowered along with the lowering of the work function.